

Origin of the atypical Puy-les-Vignes W breccia pipe (Massif Central, France)
constrained by trace element and boron isotopic composition of tourmaline

Matthieu Harlaux^{1,2*}, Julien Mercadier¹, Christian Marignac¹, Johan Villeneuve³, Bernard Mouthier⁴, Michel Cuney¹

¹ *Université de Lorraine, CNRS, CREGU, GeoRessources, 54506 Vandœuvre-lès-Nancy, France.*

² *Present Address: Department of Earth Sciences, University of Geneva, 1205 Geneva, Switzerland.*

³ *Université de Lorraine, CNRS, CRPG, 54501 Vandœuvre-lès-Nancy, France.*

⁴ *5 Quai André Lassagne, 69001 Lyon, France.*

** Corresponding author: matthieu.harlaux@unige.ch*

Abstract

The Puy-les-Vignes W deposit is an atypical wolframite-bearing hydrothermal breccia pipe hosted in migmatitic biotite-sillimanite gneisses in the northwestern French Massif Central. The deposit is characterized by volumetrically important tourmaline alteration allowing to investigate the fluid evolution of the ore-forming hydrothermal system. Four generations of hydrothermal tourmaline (Tur 1 to Tur 4) formed during pre-, syn-, and post-mineralization stages were identified based on detailed petrographic observations and were analyzed *in situ* for their chemical and boron isotopic compositions. At the grain scale, tourmaline commonly shows oscillatory zoning and dissolution textures resulting from a multi-stage crystallization in a fluid-dominated system. The different generations of hydrothermal tourmaline have dravite-schorl compositions and show similar major and trace element contents falling into

the field of metamorphic rocks. High concentrations of V, Cr, Sr and low concentrations of Li, Sn in tourmaline suggest a metamorphic-dominated origin of these elements. The boron isotopic compositions of tourmaline range between -13.3‰ and -7.8‰ and cannot unambiguously distinguish between a magmatic and a metamorphic fluid origin. Our data indicate that tourmaline formation is the result of high-temperature fluid-rock interactions between the metamorphic basement and boron-rich, reduced, and low-salinity hydrothermal fluids. This allows us to propose a fluid evolution scenario for the Puy-les-Vignes ore-forming hydrothermal system. Release of magmatic-hydrothermal fluids from an unexposed peraluminous leucogranite at ca. 324 Ma is proposed as the main mechanism responsible for early greisenization and formation of disseminated Tur 1. This episode was followed by massive tourmalinization and hydraulic brecciation of the host-rocks producing a tourmaline-rich (Tur 2) crackle breccia by interactions with boron-rich hydrothermal fluids, possibly equilibrated with the metamorphic country rocks. Fluid-assisted reopening and collapse of the former tourmalinite at ca. 318 Ma yielded a matrix-supported quartz-tourmaline breccia pipe and formation of wolframite-bearing quartz veins accompanied by deposition of Tur 3. Finally, post-ore hydraulic fracturing at ca. 300 Ma led to formation of tourmaline-rich microbreccias (Tur 4) possibly from metamorphic fluids.

Keywords

Tourmaline; Boron isotopes; Trace elements; Tungsten deposit; Breccia pipe; French Massif Central.

1. Introduction

The stability of tourmaline in a large number of geological environments, from sedimentary to hydrothermal, metamorphic, and magmatic settings, makes it an excellent monitor for determining the physico-chemical conditions and the processes involved during its crystallization (Dutrow and Henry, 2011; van Hinsberg et al., 2011). The chemical and isotopic compositions of tourmaline can, for instance, yield information about the temperature, composition and source of the fluids (van Hinsberg et al., 2011; Marschall and Jiang, 2011; Slack and Trumbull, 2011). Tourmaline is a common mineral in granite-related W-Sn deposits, which dominantly consist of wolframite-cassiterite-bearing hydrothermal veins spatially associated with granitic intrusions and represent economically important producers of W and Sn (Baker et al., 2005; Černý et al., 2005). In these magmatic-hydrothermal systems, tourmaline generally represents an accessory mineral phase, locally abundant, in evolved granites and related pegmatites, greisens, quartz veins, and breccia pipes (London and Manning, 1995; Williamson et al., 2000; Jiang et al., 2004; Mlynarczyk and Williams-Jones, 2006; Lerouge and Bouchot, 2009; Mahjoubi et al., 2016; Duchoslav et al., 2017; Codeço et al., 2017; Hong et al., 2017). The spatial association between tourmalinization and the occurrence of W-Sn deposits is thus well documented worldwide. Their genetic relationship is, however, debated since cases of intense tourmalinization without associated mineralization are known (e.g., Marignac and Zouhair, 1992; London and Manning, 1995; Demirel et al., 2009). Several questions remain open about (i) the source of boron, (ii) the origin of the hydrothermal fluids, and (iii) the role of these fluids in W-Sn ore-forming processes.

In granite-related W-Sn deposits, tourmaline may form during the magmatic stage as a late-crystallizing phase from the silicate melt, during the magmatic-hydrothermal transition as

veins, breccias, replacements, or cavity-filling mineral precipitating from exsolved magmatic fluids, or during later hydrothermal episodes involving external fluids (meteoric, metamorphic, etc). Many studies considered the hydrothermal fluids and metals (W, Sn) to be of magmatic origin derived from evolved peraluminous granites (e.g., Audétat et al., 2000; Williamson et al., 2010; Hulsbosch et al., 2016; Harlaux et al., 2017, 2018a). However, the origin of boron and tourmaline in granite-related W-Sn deposits remains controversial. A magmatic origin of the boron-rich fluids was proposed for the Panasqueira W-Sn deposit (Portugal) based on the chemical and isotopic compositions of tourmaline (Codeço et al., 2017; Launay et al., 2018). Mixing between magmatic and meteoric fluids was proposed for the Sn deposits of the Cornubian Batholith (England) using the same approach (Williamson et al., 2000; Drivenes et al., 2015; Duchoslav et al., 2017). Mass balance calculations and geochemical modelling suggested, however, that the boron budget in the Sn deposits of the Cornubian Batholith cannot be derived from the granitic melts alone, but that an additional source from the metamorphic country rocks is required (Williamson et al., 2010). A mixed magmatic-metamorphic origin or a metamorphic-dominated origin of the fluids were proposed for other W-Sn deposits based on mineral chemistry, fluid inclusion, and stable isotope data (e.g., Blamart et al., 1992; Vallance et al., 2001; Chicharro et al., 2016; Dewaele et al., 2016; Van Daele et al., 2018).

This study provides new constraints for the boron and fluid source(s) involved in the formation of granite-related W-Sn deposits, based on the Puy-les-Vignes wolframite-bearing breccia pipe in the French Massif Central (FMC). Like the majority of W-Sn deposits in the European Variscan belt, the tourmalinization at Puy-les-Vignes resulted from multi-stage hydrothermal alterations related to pre-ore fluid-rock interactions, formation of the W mineralization, and post-ore fracturing episodes. Tourmaline from Puy-les-Vignes therefore allows us to investigate the fluid evolution of the ore-forming hydrothermal system during

pre-, syn-, and post-mineralization stages. Here, we present a complete characterization of tourmaline combining detailed paragenetic and textural observations, with *in situ* analysis of chemical (major, minor, and trace elements) and boron isotope compositions. Our results indicate the preponderant role of high-temperature fluid-rock interactions between the metamorphic basement and boron-rich hydrothermal fluids for tourmaline formation at Puy-les-Vignes. We further discussed the magmatic vs. metamorphic origin of the fluids during the evolution of this atypical W-mineralized hydrothermal system.

2. Geological setting

2.1. The northwestern French Massif Central

The Puy-les-Vignes W deposit (Lat. 45°49'34"N, Long. 1°31'51"E) is located in the Limousin area in the northwestern FMC (Fig. 1), which belongs to the internal part of the European Variscan belt that formed during the continental collision between Gondwana and Laurussia through the Upper Paleozoic (Faure et al., 2009a and references therein). The regional structure of the FMC consists of a stack of metamorphic nappes that developed diachronously from Late Silurian to Early Carboniferous time. Three major tectonic units are recognized from top to bottom and from north to south (Faure et al., 2009a and references therein): (i) the Upper Gneiss Unit (UGU), which is composed of migmatitic ortho- and paragneisses derived from Cambrian to Ordovician protoliths (ca. 530 to 480 Ma; Alexandrov et al., 2001; Berger et al., 2010a; Chell-Michou et al., 2017), high-pressure and high-temperature metamorphic units (eclogite, granulite), and the so-called "leptyno-amphibolite complex" composed of an Ordovician metamorphosed bimodal magmatic association; (ii) the Lower Gneiss Unit (LGU) that consists of ortho- and paragneisses similar to those of the

UGU, that were inherited from Late Ediacarian protoliths (ca. 620 to 550 Ma; Alexandre, 2007; Melleton et al., 2010; Chell-Michou et al., 2017); and (iii) the Para-Autochthonous Unit (PAU), dominated by metasedimentary rocks (micaschists, metagreywackes, and quartzites) of greenschist- to lower amphibolite-facies, that were deposited between the Neoproterozoic and Early Cambrian (ca. 650 to 530 Ma; Melleton et al., 2010). To the south, these metamorphic units are overthrust above the sedimentary rocks of the Paleozoic fold-and-thrust belt and foreland basin in the external zone (Faure et al., 2009a). The FMC hosts numerous hydrothermal W-Sn deposits, which are spatially associated with Carboniferous peraluminous biotite-cordierite or two-mica granites (Marignac and Cuney, 1999; Cuney et al., 2002; Bouchot et al., 2005). Most of these W-Sn occurrences correspond to intra- or peri-granitic quartz-wolframite-cassiterite veins and stockworks, greisens, and scheelite skarns. U-Pb dating of wolframite from several peri-granitic vein-type deposits in the FMC indicates that W mineralization formed during at least three main episodes extending over a period of 40 million years, ranging from syn-orogenic compression in the Early Carboniferous at ca. 335 Ma to post-orogenic extension in the Permian at ca. 295 Ma (Harlaux et al., 2018b).

2.2. The Puy-les-Vignes W breccia pipe

The Puy-les-Vignes deposit represents the only known W-bearing hydrothermal breccia pipe in the FMC and is hosted in migmatitic biotite-sillimanite paragneisses of the St-Léonard-de-Noblat gneiss unit, which is structurally correlated with the LGU and is located on the southern flank of the Thaurion anticline (Faure et al., 2009a). The deposit was the second-ranked tungsten mine in France during the 20th century with a past production of ca. 4,000 t WO₃ at an average grade of 0.5% WO₃. Remaining W resources may be significant since only half of the breccia pipe was mined. The former economic mineralization was limited to

wolframite-bearing quartz veins, although the whole breccia body represents a potential low-grade ore containing disseminated wolframite (Weppe, 1958). The Puy-les-Vignes breccia pipe is located close to two peraluminous granitic intrusions (Fig. 1A): (i) the Auriat biotite-muscovite granite in the northeast dated at 324 ± 1 Ma (U-Pb on zircon; Gebauer et al., 1981), and (ii) the Aureil biotite-cordierite granite in the southwest dated at 346 ± 14 Ma (Rb-Sr on whole-rock; Duthou, 1978). Several other W showings are known in the surroundings of Puy-les-Vignes (Fig. 1A), including quartz-wolframite veins (Le Moulard, Les Clauds, Etivaud, Chassagnat, Beynat, Lifarnet), as well as a second possible wolframite-bearing breccia pipe at Les Caillaudoux (Weppe, 1951, 1958). The Puy-les-Vignes breccia pipe has an oval shape with dimensions 80 x 340 m at surface and is cut into two parts by a N30°E sinistral strike-slip fault (so-called “faille limite”) with a 120-m horizontal displacement (Fig. 1B). The pipe is located at the intersection of two NE-trending dykes of microgranite and one N-trending dyke of lamprophyre, typically 1 to 4 m thick, which crosscut the enclosing gneisses, but are fragmented within the breccia.

The Puy-les-Vignes deposit has been interpreted by Weppe (1951, 1958) as a gravitational collapse breccia that evolved in several steps. A first stage of hydraulic fracturing and mass collapse produced a matrix-supported breccia composed by polygenetic and heterometric clasts of the country rocks (mainly gneisses and granites) cemented by hydrothermal quartz representing about 10% of the total volume of the breccia. The clasts are angular to sub-angular, centimetric to pluri-metric in size, and are rimmed by an aureole of tourmalinite (tourmaline±quartz), the thickness of which varies from a few millimeters to ten centimeters (Fig. 2A), and up to complete tourmalinization of the fragments. A second stage of mass collapse resulted in the formation of quartz-filled decollements, some delineating the breccia-country rocks boundaries (“gaine” or “croiseurs”) and others forming planar-curved veins (“plateures”) within the former breccia. A third stage led to the formation of a NE-trending

network of sub-parallel quartz-wolframite-sulfide veins (“filons”) dipping at high-angle (>50°), which crosscut the entire breccia pipe and the enclosing gneisses. These veins are about 400 m long with variable thickness of 0.2 to 1 m, and they were the main host for the economic W mineralization, with grades ranging from 0.2 to 2% WO₃ (Weppe, 1951, 1958; Mouthier, 2005). ⁴⁰Ar-³⁹Ar dating of muscovite associated with wolframite yielded a plateau age of 323.4 ± 0.9 Ma (Cuney et al., 2002), whereas U-Pb dating of wolframite from a mineralized vein (“filon A”, level -270 m) yielded a slightly younger concordia age of 317.7 ± 0.7 Ma for the W mineralization (Harlaux et al., 2018b). Although the underground workings extended to 300 m below surface in the former mine, the vertical extent of the deposit has not been reached and no granitic body has been found at depth. Nevertheless, it is likely that the breccia pipe is located above the apex of an unexposed granite as described for other mineralized breccia pipes (e.g., Sillitoe, 1985; Ren et al., 1995; Somarin and Ashley, 2004; Yang and Bodnar, 2004; Solomovich et al., 2012).

The paragenetic sequence of the Puy-les-Vignes deposit is divided into six main stages (Harlaux et al., 2015a): (1) Early hydrothermal alteration of the host-rocks characterized by pervasive greisenization (exo-greisen), forming a quartz-muscovite±tourmaline assemblage, and massive tourmalinization, was followed by hydraulic brecciation and mass collapse producing a quartz-tourmaline matrix-supported breccia; (2) W mineralization associated with hydraulic fracturing and formation of quartz-wolframite-arsenopyrite-tourmaline veins that crosscut the breccia pipe and enclosing rocks; (3) Fe-Cu-Zn mineralization mainly composed by veins and overgrowths of pyrite, chalcopyrite, enargite, and minor sphalerite, which overprint the quartz-wolframite-arsenopyrite veins; (4) Tourmaline-adularia-chlorite microbreccias that locally affect the wolframite-bearing quartz veins and are associated with accessory minerals of hydrothermal zircon, xenotime, monazite, Nb-Fe-W-rich rutile, and Nb-Ti-Y-HREE-W-U oxides. This mineral assemblage has been interpreted as having formed by

magmatic-hydrothermal fluids derived from an hypothetical peralkaline granitic body concealed at depth that intruded later after the W mineralization (Harlaux et al., 2015b); (5) A minor and discrete stage of Bi-Au mineralization is associated with the deposition of native bismuth, bismuthinite, electrum, and Bi-Ag-Se-Te sulfosalts, in micro-cavity and micro-crack infillings within the mineralized quartz veins; (6) Late hydrothermal scorodite ($\text{FeAsO}_4 \cdot 2\text{H}_2\text{O}$) and illite alteration followed by supergene alteration forming secondary minerals of tungstite and Fe-oxides/hydroxides.

3. Analytical methods

3.1. Scanning electron microscope

Mineralogical observations of tourmaline were performed at the Service Commun de Microscopies Electroniques et de Microanalyses (SCMEM) of GeoRessources laboratory (Vandœuvre-lès-Nancy, France) using a Jeol J7600F scanning electron microscope (SEM) equipped with a SDD-type energy dispersive X-ray spectrometer (EDS) coupled to an Oxford Wave wavelength dispersive X-ray spectrometer (WDS). Backscattered electron (BSE) images were obtained on polished thin sections with an acceleration voltage of 15 kV, adjusting the electronic brightness to reveal the internal zoning in tourmaline. SEM was used to study the internal textures of tourmaline and to select crystals for the *in situ* chemical and isotopic analyses. Microanalyses were performed along profiles in selected grains of tourmaline to determine the major element variations along micrometre-scale zoning. The major elements measured were calibrated using the same standards as for the electron microprobe analyses (see below).

3.2. Electron microprobe

The major and minor element composition of tourmaline was determined using a Cameca SX100 electron microprobe analyzer (EMPA) at SCMEM, operated with an acceleration voltage of 15 kV, a beam current of 12 nA, and a beam diameter of 5 μm . The following standards were analyzed using WDS spectrometers: albite (Si, Na), corundum (Al), olivine (Mg), hematite (Fe), ilmenite (Mn, Ti), orthose (K), andradite (Ca), and Cr_2O_3 (Cr). Counting times were 10 s on element peaks and 5 s on background. Limits of detection are: 500 ppm for Si, Al; 600 ppm for Na, Ca; 400 ppm for Mg, K, Ti; 1700 ppm for Fe; 1600 ppm for Mn; and 900 ppm for Cr. Analytical error was <1% for most elements. Structural formulae of tourmaline were calculated using the Excel spreadsheet from The Open University, UK (Tindle et al., 2002) normalizing to 31 anions and assuming stoichiometric 3 atoms for B and 4 atoms for OH+F, based on the general formula $\text{XY}_3\text{Z}_6(\text{T}_6\text{O}_{18})(\text{BO}_3)_3\text{V}_3\text{W}$, where $\text{X}=\text{Na}^+$, Ca^{2+} , K^+ , and vacancy (X_{\square}); $\text{Y}=\text{Fe}^{2+}$, Mg^{2+} , Mn^{2+} , Al^{3+} , Li^+ , Fe^{3+} , and Cr^{3+} ; $\text{Z}=\text{Al}^{3+}$, Fe^{3+} , Mg^{2+} , Ti^{4+} , and Cr^{3+} ; $\text{T}=\text{Si}^{4+}$, Al^{3+} , and B^{3+} ; $\text{B}=\text{B}^{3+}$; $\text{V}=\text{OH}^-$, and O^{2-} ; and $\text{W}=\text{OH}^-$, F^- , and O^{2-} (Henry et al., 2011). Fe_2O_3 was calculated assuming all extra charges to be Fe^{3+} , whereas all deficiency in charge was assigned to presence of O^{2-} in the W-site. The chemical compositions of tourmaline are reported in weight per cent oxides (wt.%) and the structural formulae are expressed in atoms per formula unit (apfu). The results presented here correspond to approximately 400 spot microanalyses on the different generations of tourmaline. X-ray element maps were acquired with an acceleration voltage of 15 kV, a beam current of 100 nA, and a beam diameter of 1 μm . The elements Fe, Mg, Ti, Ca, and F were measured with dwell times of 0.2 s each and an acquisition step of 1 μm , for a total map size of 148 x 129 μm .

3.3. Laser ablation - inductively coupled plasma - mass spectrometry

The concentrations of minor and trace elements in tourmaline were measured by laser ablation - inductively coupled plasma - mass spectrometry (LA-ICP-MS) at GeoRessources laboratory using a Agilent 7500c quadrupole ICP-MS coupled with a 193 nm GeoLas ArF Excimer laser (MicroLas, Göttingen, Germany). Laser ablation was performed on polished thin sections with a constant 5 Hz pulse frequency and a constant fluence of 6 J/cm². LA-ICP-MS spot analyses were performed using variable laser beam diameters between 24 and 90 µm, depending on the size of zoning in tourmaline. Helium was used as carrier gas to transport the laser-generated particles from the ablation cell to the ICP-MS and argon was added as an auxiliary gas via a flow adapter before the ICP torch. Typical flow rates of 0.5 L/min for He and 0.9 L/min for Ar were used. The certified reference material NIST SRM 610 (concentrations from Jochum et al., 2011) was used as an external standard for calibration of all analyses, and was analyzed twice at the beginning and at the end of each set of samples, following a bracketing standardization procedure. The reference material NIST SRM 612 (concentrations from Jochum et al., 2011) was used as a control standard to verify the quality of the analyses and of the standardization. LA-ICP-MS calibration was optimized for highest sensitivity on the whole m/Q range, while maintaining Th/U ~ 1 and ThO/Th <0.5%, as determined on NIST SRM 610. The following 40 isotopes were measured with a dwell time of 10 ms for each: ⁷Li, ⁹Be, ²⁹Si, ⁴⁵Sc, ⁴⁷Ti, ⁵¹V, ⁵³Cr, ⁵⁹Co, ⁶⁰Ni, ⁶³Cu, ⁶⁶Zn, ⁸⁵Rb, ⁸⁸Sr, ⁸⁹Y, ⁹⁰Zr, ⁹³Nb, ⁹⁵Mo, ¹¹⁸Sn, ¹³³Cs, ¹³⁷Ba, ¹³⁹La, ¹⁴⁰Ce, ¹⁴¹Pr, ¹⁴⁶Nd, ¹⁴⁷Sm, ¹⁵³Eu, ¹⁵⁷Gd, ¹⁵⁹Tb, ¹⁶³Dy, ¹⁶⁵Ho, ¹⁶⁶Er, ¹⁶⁹Tm, ¹⁷²Yb, ¹⁷⁵Lu, ¹⁸¹Ta, ¹⁸²W, ²⁰⁸Pb, ²⁰⁹Bi, ²³²Th, and ²³⁸U. In these conditions, the cycle time was about 496 ms. Analytical background was recorded for 30 s at the beginning of each analysis followed by acquisition of the LA-ICP-MS signal of tourmaline for 40-60 s. Data reduction and absolute quantification of signals were performed

using the software StalQuant developed at the ETH Zürich, Switzerland. For each LA-ICP-MS analysis, the Si content previously determined by EMPA was used as internal standard. Limits of detection (LOD) were calculated using the 3σ criterion from Longerich et al. (1996).

3.4. Secondary ion mass spectrometry

Boron isotope compositions of tourmaline were measured by secondary ion mass spectrometry (SIMS) using a Cameca IMS 1280-HR instrument at the CRPG-CNRS (Vandœuvre-lès-Nancy, France). Analyses were performed on the same polished thin sections analyzed by LA-ICP-MS with a 20 nA beam of primary ions O^+ accelerated at 13 kV. The secondary ions $^{10}B^+$ and $^{11}B^+$ were accelerated at 10 kV and were measured in mono-collection with a mass resolution $M/\Delta M=2000$. Each calculated isotopic ratio $^{11}B/^{10}B$ corresponds to 30 cycles of measurement with counting times of 8 s per cycle on mass 10 and of 4 s per cycle on mass 11. The ablation spot size was fixed to 20 μm . Instrumental mass fractionation (IMF) was determined and corrected using two tourmaline reference materials corresponding to dravite (Harvard #108796) and schorl (Harvard #112566) described by Dyar et al. (2001) and Leeman and Tonarini (2001). Each standard was measured several times during the analytical SIMS session following a standard-sample-standard bracketing procedure. The summary of the SIMS B isotope analyses on the tourmaline reference materials is given in the Electronic Supplementary Material. After correction of IMF, the measured $^{11}B/^{10}B$ ratios were reported in $\delta^{11}B$ notation (in ‰) relative to the NIST SRM 951, whose $^{11}B/^{10}B$ ratio is 4.04362 (Catanzaro et al., 1970). The external reproducibility (2σ) is about 0.6‰ on dravite and schorl standards. The external error used is that of the relevant reference material, and the total uncertainty is the quadratic sum of the internal and external

errors. The total errors on individual analysis are typically $\pm 0.4\%$ (2σ).

4. Results

4.1. Paragenesis and internal textures of tourmaline

Tourmalinization represents the most important hydrothermal alteration in the Puy-les-Vignes deposit. It occurred from the early hydrothermal alteration stage that followed the formation of the collapse breccia pipe and continued until silicification and vein opening leading to the deposition of wolframite, as well as during later fracturing episodes. Four generations of hydrothermal tourmaline (Tur 1 to Tur 4) are identified based on crosscutting relationships and detailed textural observations.

4.1.1. Greisen tourmaline (Tur 1)

This tourmaline is only found in the internal part of greisenized host-rock clasts (mainly gneisses) and it represents the earliest generation identified in the Puy-les-Vignes deposit. Tur 1 forms sub-euhedral crystals of green-brownish colour in plane-polarized light, ranging from 50 to 100 μm in size, which are disseminated in clusters within the quartz and muscovite assemblage of the greisen (Fig. 2B). On BSE images, Tur 1 shows an internal zoning composed of three successive zones (Fig. 3A): (i) a medium grey core forming the main part of the grains and showing a relatively homogeneous texture; (ii) a light grey irregular rim, a few to tens of μm -wide, surrounding the core with textural evidence of corrosion. The core-rim interface is thus interpreted as a dissolution-precipitation front; (iii) a dark overgrowth of tens of μm wide that surrounds the tourmaline grains in apparent continuity with the rim.

4.1.2. Tourmalinites (Tur 2)

This second generation of tourmaline is related to the most important stage of tourmalinization at Puy-les-Vignes. It corresponds to the formation of black aureole of tourmalinite (tourmaline±quartz) on the rims of the host-rock clasts (gneisses and granites) composing the breccia body. The tourmalinite rims are of variable thickness, ranging from a few millimetres to tens of centimetres, up to complete tourmalinization of the clasts (Fig. 2A). The contact between the tourmalinite and the quartz forming the breccia matrix is sharp and crack-seal textures are common along the tourmaline-quartz borders. This indicates that silicification of the breccia was synchronous to the mass collapse and occurred after formation of the tourmalinite. At the microscopic scale, the tourmalinite rim is composed of aggregates of prismatic grains cemented by limpid macrocrystalline quartz. There are some textural differences between gneissic and granitic clasts. Tourmaline on gneissic clasts (Tur 2a) consists of sub-euhedral crystals with an orange-brownish to greenish colour in plane-polarized light and ranging from 50 to 500 μm in size (Fig. 2C). They typically display zoning composed of three successive zones on BSE images (Fig. 3B): (i) a dark grey core (<50 μm in size) showing a patchy texture; (ii) a discrete and irregular bright rim, of a few micrometres thickness, that locally replaces the core; and (iii) an overgrowth in continuity with the rim that forms the largest part of the tourmaline grains and is characterized by a micrometre-scale oscillatory zoning. X-ray element maps show that the core has higher Mg and Ca contents than the overgrowth, which is generally Fe-rich but with fluctuating Fe and Mg contents corresponding to the oscillatory zoning (Fig. 4). Intracrystalline variations in Ti contents reflect sector zoning. Tourmaline on granitic clasts (Tur 2b) forms larger crystals, ranging from 100 μm up to a few millimetres, which have a green-brownish colour in plane-polarized light (Fig. 2D). On BSE images, the crystals show more complex internal textures composed of the following zones (Fig. 3C): (i) a dark grey core showing some sector zoning

and patchy texture; (ii) a light grey rim in continuity with the core and showing oscillatory zoning at the micrometre-scale; (iii) a dark overgrowth with a relatively homogeneous texture surrounding the rim; (iv) a bright external corrosion, which crosscuts and partially replaces the previous zones. This late tourmaline shows a particularly fine-scale growth zoning (Fig. 3D).

4.1.3. Acicular tourmaline (Tur 3)

This third tourmaline generation was only found within the quartz of the breccia matrix and in wolframite-bearing quartz veins, where it is locally intergrown with wolframite suggesting it is syn-mineralization. Tur 3 forms large elongated euhedral crystals with a green-bluish colour or colourless in plane-polarized light. Most crystals range from 500 μm to a few millimetres in size, but the largest ones reach a few centimetres (Fig. 2E). Acicular tourmaline is found either as isolated or fan-like aggregates disseminated within the quartz, or as fibrous crystals directly overgrown on the wall-rock selvages. The tourmaline crystals are commonly fractured within the quartz, suggesting that the quartz-tourmaline breccia and veins underwent a late brittle deformation episode. The internal texture of acicular tourmaline is composed of (i) a large core forming the main part of the crystals, and (ii) a rim a few μm -thick that shows growth zoning. Tourmaline sections perpendicular to the c-axis typically show sector zoning (Fig. 3E).

4.1.4. Microbreccia tourmaline (Tur 4)

This last generation is restricted to a late tourmaline-adularia-chlorite microbreccia episode that postdates the W mineralization. The microbreccia is composed of a dense aggregate of prismatic tourmaline grains, which are cemented by adularia and chlorite, with minor muscovite. The tourmaline crystals have an orange-brownish to bluish colour in plane-

polarized light and range from 50 to 500 μm in size (Fig. 2F). Tur 4 is internally-zoned (Fig. 3F) with: (i) a medium grey core showing a patchy texture; (ii) a light grey rim, of several tens of μm thick, forming the largest part of the grains. The core-rim interface is irregular and shows evidences of corrosion-dissolution; (iii) a dark overgrowth with micrometre-scale zoning in continuity with the previous rim.

4.2. Chemical composition and crystal chemistry of tourmaline

4.2.1. Major and minor elements

Representative chemical compositions of tourmaline from Puy-les-Vignes are summarized in Table 1 and the complete dataset is provided in the Electronic Supplementary Material. The different generations of hydrothermal tourmaline have overall similar chemical compositions, with some variations in the major elements Fe (0.5-1.7 apfu), Mg (0.7-2.1 apfu), and Al (5.6-6.9 apfu), as well as for the minor elements Na (0.4-0.8 apfu), Ti (<0.3 apfu), and Ca (<0.2 apfu). Tourmaline belongs mostly to the alkali group and plots within the field of metasedimentary rocks in the Al-Fe-Mg diagram (Fig. 5). Only a minority of tourmaline belongs to the X-vacant group and plots along the field of granites and pegmatites (Fig. 5). Tourmaline compositions correspond dominantly to the dravite–schorl solid solution, with a few analyses corresponding to the foitite–Mg-foitite solid solution (Fig. 6). The compositional variations of tourmaline are related to variable ratios of $\text{Fe}/(\text{Fe}+\text{Mg})=0.23\text{-}0.69$ and $\text{X}_{\square}/(\text{X}_{\square}+\text{Na})=0.12\text{-}0.61$, which are mainly attributed to the exchange vectors $\text{Fe}^{2+}_{+1}\text{Mg}^{2+}_{-1}$ and $(\square\text{Al}^{3+})_{+1}(\text{Na}^{+}\text{Mg}^{2+})_{-1}$ (Fig. 6).

In detail, the different tourmaline generations show chemical variations of the optically-distinguished zones. Pre-ore Tur 1 has variable $\text{Fe}/(\text{Fe}+\text{Mg})=0.28\text{-}0.64$ and $\text{X}_{\square}/(\text{X}_{\square}+\text{Na})=0.12\text{-}0.49$, which reflects compositional zoning. The core and overgrowth are

characterized by similar dravitic compositions with low $\text{Fe}/(\text{Fe}+\text{Mg})$ values (0.28–0.54), whereas the rims have higher $\text{Fe}/(\text{Fe}+\text{Mg})$ values (0.56–0.64). Tur 2a hosted in gneissic clasts has relatively homogeneous major element compositions corresponding to dravite with minor variations in $\text{Fe}/(\text{Fe}+\text{Mg})=0.33\text{--}0.57$ and $\text{X}_{\square}/(\text{X}_{\square}+\text{Na})=0.28\text{--}0.57$. Tur 2b hosted in granitic clasts has more variable compositions with $\text{Fe}/(\text{Fe}+\text{Mg})=0.23\text{--}0.64$ and $\text{X}_{\square}/(\text{X}_{\square}+\text{Na})=0.21\text{--}0.60$. The range is mainly due to differences between the core zone and overgrowth ($\text{Fe}/(\text{Fe}+\text{Mg})=0.23\text{--}0.36$) and the rims ($\text{Fe}/(\text{Fe}+\text{Mg})=0.44\text{--}0.64$). Syn-ore Tur 3 has dravitic composition with homogeneous compositions having $\text{Fe}/(\text{Fe}+\text{Mg})=0.24\text{--}0.43$ and $\text{X}_{\square}/(\text{X}_{\square}+\text{Na})=0.31\text{--}0.51$. Post-ore Tur 4 has compositions intermediate between foitite and dravite with an extended range of $\text{Fe}/(\text{Fe}+\text{Mg})=0.26\text{--}0.58$ and $\text{X}_{\square}/(\text{X}_{\square}+\text{Na})=0.16\text{--}0.61$ ratios. The cores are distinguished by high $\text{X}_{\square}/(\text{X}_{\square}+\text{Na})=0.46\text{--}0.61$ with schorl compositions, whereas the rims and overgrowths have more dravitic compositions with lower $\text{X}_{\square}/(\text{X}_{\square}+\text{Na})=0.16\text{--}0.50$ and higher Ti contents (up to 0.26 apfu).

4.2.2. Trace elements

Average trace element compositions of tourmaline from Puy-les-Vignes are summarized in Table 2 and the complete dataset is given in the Electronic Supplementary Material. Tourmaline is overall characterized by low concentrations (<0.1 to 10 ppm) of Co, Ni, Cu, Rb, Y, REE, Zr, Nb, Mo, Cs, Ba, Ta, W, Pb, Bi, Th, and U, intermediate concentrations (10s to 100 ppm) of Li, Be, Sc, Sr, and Sn, and high concentrations (100s to >1000 ppm) of Ti, V, Cr, and Zn (Fig. 7). The different generations of hydrothermal tourmaline show slightly compositional zoning principally marked by variations in Sc (5–228 ppm), Ti (580–7780 ppm), V (64–804 ppm), Cr (9–13060 ppm), Ni (20–135 ppm), Zn (39–280 ppm), Sr (13–263 ppm), total REE (0.3–15 ppm), Sn (7–147 ppm), and Pb (0.7–19 ppm) (Fig. 7). In multi-

421 element diagrams normalized to the upper continental crust (UCC from Rudnick and Gao,
422 2003), the different tourmaline generations show similar trace element patterns with relative
423 enrichments in Sc, V, Cr, Be, Bi, and Zn between 2 and 100 times higher than the UCC
424 values, and relative depletions in Sr, Ba, Cs, Rb, Y, Nb, Ta, Zr, Ti, U, Th, Mo, Sn, Pb, and Cu
425 between 5 and 100 times lower than the UCC values (Fig. 8). Principal component analysis
426 (PCA) has been applied in order to understand the compositional variations of tourmaline and
427 to identify trace element correlations. PCA is a multivariate statistical technique that provides
428 dimensionality-reduction of correlated variables into a reduced set of orthogonal linear
429 combinations (so-called principal components), maximizing the variance and minimizing
430 information loss (Izenman, 2008). PCA is a classical method of multivariate statistics that is
431 particularly useful for treating large geochemical datasets such as LA-ICP-MS trace element
432 analyses of minerals (e.g., Winderbaum et al., 2012; Belissont et al., 2014). Results of the
433 PCA are represented by a two-dimensional projection of the two first principal components
434 (PC1 vs. PC2), which describe the statistical correlations between the investigated variables
435 on a correlation circle. Classical PCA has been applied to the log-transformed LA-ICP-MS
436 dataset of trace element contents in tourmaline (n=116 spot analyses). A total of 18 variables
437 has been selected for the PCA including the main trace elements (Li, Sc, Ti, V, Cr, Co, Zn, Sr,
438 Y, Zr, Nb, Sn, LREE, HREE, W, Pb, Th, U) determined by LA-ICP-MS. Other trace elements
439 at very low concentrations (<1 ppm) or below the limits of detection were not included. PCA
440 applied to each individual generation of tourmaline led to the same group correlations than
441 PCA applied to the complete tourmaline dataset. The projection of the PC1 vs. PC2 planes
442 accounts for 53% of the element content variability. Four groups of element correlation
443 clusters are discriminated by the PCA (Fig. 9). A first group is composed of HREE, Y, Zr, Th,
444 and U, which correspond to trivalent and tetravalent high field strength elements. A second
445 group includes Li, Ti, LREE, Sr, and Pb, which correspond mostly to monovalent and bivalent

large ion lithophile elements. A third group consists of Nb, Sn, and W, which are tetravalent to hexavalent high field strength elements. A fourth group includes Sc and V, which are anti-correlated with the second group. Finally, the elements Co, Cr, and Zn plot individually, without correlations between each other. Site occupancy in tourmaline is controlled by the charge-to-radius ratios of the elements, with incorporation of 1+ and some 2+ elements (Na, K, Ca, Li, Sr, Pb, etc) in the X-site, 3+, 4+ and some 2+ elements (Fe, Mg, Mn, Co, Ni, Cu, Zn, Sc, Cr, V, Ga, REE, Ti, Hf, Zr, U, etc) in the Y- and Z-sites (van Hinsberg, 2011). The statistical correlation clusters identified by PCA therefore reflect partly the crystallochemical control for the incorporation of trace elements in tourmaline. Variation diagrams of selected trace elements (Fig. 10) show overlapping concentrations between the different tourmaline generations precluding the discrimination of distinct clusters. Positive correlations between Li vs. Ti, Sr vs. Sn, Sn+W vs. Nb+Ta, Sc vs. V, Pb vs. Sr, or LREE vs. Sr, confirm the results from the PCA.

4.3. Boron isotopic compositions of tourmaline

The boron isotopic compositions of tourmaline from Puy-les-Vignes are reported in Table 3. The $\delta^{11}\text{B}$ values of tourmaline (n=46) range in total from -13.3‰ to -7.8‰ with a mean value of $-11.4 \pm 1.5\text{‰}$ (Fig. 11). The within-sample variations are typically 1-3‰ and are related to growth zoning. Greisen-hosted Tur 1 has $\delta^{11}\text{B}$ values between -11.1‰ and -7.8‰ (mean = $-9.2 \pm 1.0\text{‰}$, n=11) with the cores having lower $\delta^{11}\text{B}$ values compared to the rims and overgrowths. Pre-ore Tur 2a has $\delta^{11}\text{B}$ values ranging from -13.1‰ to -11.1‰ (mean = $-11.9 \pm 0.6\text{‰}$, n=8) with no significant boron isotopic zonation. Syn-ore Tur 3 also has homogeneous $\delta^{11}\text{B}$ values ranging from -13.2‰ to -12.1‰ (mean = $-12.7 \pm 0.3\text{‰}$, n=12) without distinction between core and rim. Finally, Tur 4 has $\delta^{11}\text{B}$ compositions between -13.3‰ and -10.3‰

(mean = $-11.8 \pm 0.9\%$, n=15) with no isotope zoning.

5. Discussion

5.1. Intracrystalline zoning and compositional variations in tourmaline

Tourmaline from the Puy-les-Vignes deposit shows internal zoning and variations in major, minor, and trace elements. The majority of tourmaline grains have cores surrounded by rims and overgrowths, which display both sector and concentric zoning. The core-rim interface is commonly marked by dissolution evidences, whereas the overgrowth typically shows oscillatory zoning at the micrometre-scale. The formation of oscillatory zoning is a typical feature of hydrothermal minerals and has generally been interpreted to result from external and/or internal controls (Shore and Fowler, 1996). In the first case (external control), oscillations may be caused by periodic changes in the external environment due to varying fluid conditions such as chemical composition, pressure, or temperature (e.g., Holten et al., 1997). In the second case (internal control), the oscillations are related to self-organized processes during the crystalline growth, which are controlled by absorption-diffusion mechanisms at the crystal-fluid interface (e.g., L'Heureux and Jamtveit, 2002) or by micromorphological instabilities of the growing face (e.g., Shtukenberg and Punin, 2011). Oscillatory zoning may also result from a combination of both external and internal controls, whereby crystal-scale variations are related to bulk changes in the hydrothermal fluid whereas fine-scale modulations are caused by growth-rate-controlled incorporation of trace elements (Barker and Cox, 2011). Quantitative microanalyses performed along an oscillatory zoning in a representative tourmaline crystal show chemical evolution trends at the growth-band scale (Fig. 12). The external overgrowth shows a succession of rhythmic growth bands (dark and

light) on BSE images, each of them being marked by a systematic Fe increase (0.93–1.18 apfu) and Mg decrease (1.27–1.09 apfu). The oscillatory zoning corresponds therefore to an increasing trend of the Fe/(Fe+Mg) ratio (0.42–0.52) along the growth direction. The compositional changes marking the transition between the growth bands could not be caused by a continuous fractionation trend of a single fluid in closed-system, which is expected to yield rather continuous variations with a decreasing Fe/(Fe+Mg) ratio over time. By contrast, the increasing Fe/(Fe+Mg) ratio along the compositional zoning is interpreted as reflecting rapid crystal growth or dynamic changes in the external fluid conditions. This interpretation is supported by (i) the formation of the breccia pipe by a collapse mechanism indicating rapidly changing fluid overpressure conditions, (ii) the density of euhedral tourmaline crystals composing the tourmalinite rims suggesting that the hydrothermal fluid was oversaturated relative to tourmaline allowing homogeneous and possibly rapid nucleation, and (iii) the dissolution evidences at the core-rim interface attesting that the fluid responsible was locally out-of-equilibrium and reacted with the pre-existing tourmaline by a dissolution-precipitation mechanism. Multi-stage formation of tourmaline at Puy-les-Vignes is thus demonstrated by growth zoning and crosscutting relationships, arguing for successive boron-rich fluid circulation episodes in a dynamic hydrothermal system.

5.2. Tourmaline composition as indicator of fluid chemistry

The major and trace element composition of tourmaline is a reliable geochemical monitor of its forming environment and has been used to trace the fluid evolution and sources in magmatic-hydrothermal systems (e.g., Jiang et al., 2004; Marks et al., 2013; Drivenes et al., 2015; Yang et al., 2015; Duchoslav et al., 2017; Hong et al., 2017; Dutrow and Henry, 2018). Precipitation of tourmaline from aqueous fluids requires high boron contents (>0.5-1.0 wt.%)

521 B₂O₃) and acidic-to-near neutral conditions (pH<6) that favor trigonal coordination of boron
 522 in the fluid (Morgan and London, 1989; Henry and Dutrow, 1996). Tourmaline compositions
 523 from Puy-les-Vignes plot along the dravite-schorl solid solution and have relatively low Na
 524 contents (average 0.6 apfu) and high X-site vacancies (average 0.4 apfu), suggesting
 525 precipitation from a low-salinity fluid (von Goerne et al., 2001, 2011; Dutrow and Henry,
 526 2018). Assuming a temperature of 500°C, a salinity of ca. 3 wt.% NaCl eq can be estimated
 527 for the fluid in equilibrium with the assemblage tourmaline + quartz + chlorite (von Goerne et
 528 al., 2001). The dominant substitution mechanisms observed in tourmaline are $\text{Fe}^{2+}_{+1}\text{Mg}^{2+}_{-1}$
 529 and $(\square\text{Al}^{3+})_{+1}(\text{Na}^{+}\text{Mg}^{2+})_{-1}$ (Fig. 6), with no contribution of the $\text{Fe}^{3+}_{+1}\text{Al}^{3+}_{-1}$ exchange vector in
 530 the Al vs. Fe diagram (not shown), thus suggesting low $\text{Fe}^{3+}/\text{Fe}^{2+}$ ratios and reduced fluid
 531 conditions. These conclusions are supported by fluid inclusion studies of quartz associated
 532 with the tourmalinite (Tur 2) that reported low-salinity (2-5 wt.% NaCl eq), high-temperature
 533 (>500°C), and elevated CO₂-CH₄-N₂ contents (Alikouss, 1993), pointing to fluid compositions
 534 controlled by the graphite-water equilibrium with C-rich metasediments under reduced
 535 hydrothermal conditions (Ramboz et al., 1985; Dubessy et al., 1989). The different tourmaline
 536 generations show considerable overlap in their major and trace element contents (Figs. 5 to 8)
 537 and lack distinct chemical signatures allowing discrimination of clusters. This may reflect the
 538 role of fluid-rock interaction processes as already proposed in several studies (Hazarika et al.,
 539 2015; Kalliomäki et al., 2017). Incorporation of major and trace elements in hydrothermal
 540 tourmaline is fundamentally controlled by the tourmaline-fluid partition coefficients, which
 541 depend on crystal chemistry constraints and external conditions (van Hinsberg, 2011). Several
 542 studies reported that the major and trace element contents of tourmaline mirror the host-rock
 543 composition and local fluid-rock interactions (Henry and Guidotti, 1985; Raith et al., 2004;
 544 Marks et al., 2013; Hazarika et al., 2015; Kalliomäki et al., 2017). High concentrations (>100
 545 ppm) of V, Cr, and Sr, and low concentrations (<50 ppm) of Li and Sn in tourmaline from

Puy-les-Vignes suggest an input of these elements from metasedimentary-volcanic rocks rather than magmatic sources (Jiang et al., 2004; Galbraith et al., 2009; van Hinsberg and Schumacher, 2011; Marks et al., 2013; Hazarika et al., 2015; Yang et al., 2015; Kalliomäki et al., 2017). In particular, Li and Sr have been proposed as suitable indicators for discriminating between a magmatic and metamorphic origin of hydrothermal tourmalines (Kalliomäki et al., 2017). Using the Li/Sr ratio as a proxy for the fluid source, we compared the composition of tourmaline from Puy-les-Vignes for selected trace elements with worldwide tourmaline hosted in granites, metasediments, and metavolcanics (Fig. 13). Despite some variations, tourmaline from Puy-les-Vignes has trace element contents overlapping with the compositional field of metamorphic tourmaline, which is also in agreement with its major element compositions falling into the field of metasediments in the Al-Fe-Mg diagram (Fig. 5). This would indicate that hydrothermal tourmalines from Puy-les-Vignes were dominantly formed from fluids that interacted with metavolcanic and metasedimentary host-rocks. In order to evaluate the potential sources of the trace elements, we compared the average composition of tourmaline from Puy-les-Vignes with the whole-rock compositions of the main host-rock lithologies in the northwestern FMC, composed of peraluminous granites, gneisses, and metabasic rocks (Fig. 14). Tourmaline shows intermediate trace element patterns with similar enrichments in granitophile elements (Be, U, Sn, W, Bi, U) and transition metals (Sc, V, Cr, Zn, Ni) compared to evolved peraluminous granites and gneisses, and metabasic rocks, respectively. This finding is relevant since peraluminous granites and gneissic-amphibolite rocks are known in a distance <5 km around the Puy-les-Vignes deposit (Fig. 1). The REE pattern of tourmaline is marked by enrichments in HREE over LREE, with a positive Eu anomaly, and it is clearly different from the REE spectra of peraluminous granites and gneisses but resembles those of metabasic rocks. The REE patterns of tourmaline have been shown to reflect the REE composition of their host-rock lithologies and the effects of fluid-rock interactions (e.g.,

Torres-Ruiz et al., 2003; Marks et al., 2013; Yang et al., 2015; Duchoslav et al., 2017; Kalliomäki et al., 2017; Hong et al., 2017). The depletion in LREE over HREE and the low total REE contents of Puy-les-Vignes tourmaline may reflect (i) variable fluid/rock ratios during the tourmalinization process (Torres-Ruiz et al., 2003; Pesquera et al., 2005), (ii) LREE incorporation in accessory phases (rutile, monazite, zircon) co-crystallizing with tourmaline in the fluid, or (iii) presence of micro-inclusions (zircon, rutile, titanite, etc.) in tourmaline (Jiang et al., 2004; Hazarika et al., 2015). The positive Eu anomaly ($\text{Eu}/\text{Eu}^*=2-4$) indicates the predominance of Eu^{2+} in the fluid and its preferential partitioning over Eu^{3+} into the X-site of tourmaline (van Hinsberg, 2011). This would also indicate a reducing nature of the fluids, in accordance with the inferred low $\text{Fe}^{3+}/\text{Fe}^{2+}$ ratios. In summary, the major and trace element compositions of tourmaline possibly records a mixed magmatic-metamorphic signature resulting from fluid-rock interaction processes yielding to two possible interpretations: (i) the fluid was of magmatic origin, exsolved from a crystallizing peraluminous melt, and strongly interacted with the metamorphic host-rocks during formation of the breccia pipe; or (ii) the fluid was of metamorphic origin, possibly produced by devolatilization reactions, and leached out metals from the granitic basement during high-temperature fluid-rock interactions. Considering the inferred low fluid salinity and reducing conditions, a metamorphic-hydrothermal origin seems more likely.

5.3. B isotope constraints on the fluid source(s): magmatic vs. metamorphic origin

The total range of $\delta^{11}\text{B}$ values in tourmaline from Puy-les-Vignes is large, varying from -13.3‰ to -7.8‰ (average $\delta^{11}\text{B} = -11.4‰$), with most of the tourmaline having $\delta^{11}\text{B}$ values <-10‰ (Fig. 11). These $\delta^{11}\text{B}$ values cannot unambiguously distinguish between a granitic and a metamorphic source of boron due to the large isotopic overlap of these two reservoirs

596 (Marschall and Jiang, 2011; Trumbull and Slack, 2018). Previous boron isotope studies on
 597 tourmaline from W-Sn deposits in the European Variscan belt reported $\delta^{11}\text{B}$ values ranging
 598 from -15‰ to +2‰ with a mean around -10‰, and concluded that boron was dominantly
 599 derived from magmatic fluids exsolved from peraluminous granitic melts (Smith and Yardley,
 600 1996; Pesquera et al., 2005; Jiang et al., 2008; Ribeiro da Costa et al., 2014; Drivenes et al.,
 601 2015; Codeço et al., 2017). Recent SIMS data from the Panasqueira W-Sn deposit (Portugal)
 602 show that tourmaline has $\delta^{11}\text{B}$ values comprised between -12.7‰ and -3.7‰ (average $\delta^{11}\text{B}$ =
 603 -9‰), which has been interpreted as a boron source derived from a S-type granite (Codeço et
 604 al., 2017). Generally, the boron isotopic composition of tourmaline is controlled by (i) the
 605 composition of the boron source, (ii) the temperature of formation, and (iii) the fluid/rock
 606 ratio (Palmer and Slack, 1989). Based on existing tourmaline-fluid boron isotope fractionation
 607 factors from Meyer et al. (2008), valid for $T=400\text{--}700^\circ\text{C}$ and $P=200\text{ MPa}$, it is possible to
 608 estimate the isotopic composition of the hydrothermal fluid in equilibrium with tourmaline
 609 depending on temperature. Fluid inclusion data from hydrothermal quartz associated with the
 610 tourmalinite (Tur 2) yielded trapping conditions at temperatures of $540 \pm 50^\circ\text{C}$ and pressures
 611 of $2.5 \pm 0.5\text{ kbar}$ (Alikouss, 1993). This is consistent with the Zr-in-rutile temperatures of 530
 612 $\pm 35^\circ\text{C}$ estimated for W-bearing rutile intergrown with the tourmalinite (Harlaux, 2016).
 613 Assuming a crystallization temperature of 500°C and an average $\delta^{11}\text{B} = -11.4‰$ for
 614 tourmaline, the fluid in isotopic equilibrium would have a $\delta^{11}\text{B} = -9.5‰$ using tourmaline-
 615 fluid boron isotope fractionation factors (Meyer et al., 2008). A magmatic fluid origin can be
 616 tested by calculating the isotopic composition of a boron-rich peraluminous granitic melt,
 617 which would have produced a magmatic fluid with a $\delta^{11}\text{B} = -9.5‰$. At 650°C , a boron isotope
 618 fractionation factor of 5‰ can be predicted between the granitic melt and the aqueous fluid
 619 (Hervig et al., 2002), considering a 50:50 proportion of trigonal-tetrahedral coordination of
 620 boron in the melt (see discussion by Trumbull et al., 2013). This would imply a $\delta^{11}\text{B} = -$

14.5‰ for the hypothetical granitic source, which falls in the typical range of S-type granites (Trumbull and Slack, 2018). A metamorphic fluid origin is also possible since metasediments generally contain high amounts of boron >80 ppm on average and up to 100s ppm (Ishikawa and Nakamura, 1993; Leeman and Sisson, 1996; Nakano and Nakamura, 2001; Wilke et al., 2002; Trumbull and Slack, 2018). Metamorphic dehydration reactions and fluid-rock interactions represent two possible processes that may efficiently extract boron from metasediments (e.g., Nakano and Nakamura, 2001; Kawakami and Ikeda, 2003; van Hinsberg et al., 2011). During prograde metamorphism, the muscovite-breakdown reaction of metapelitic rocks produces a low-salinity, reduced, and boron-rich metamorphic fluid (Moran et al., 1992; Dutrow et al., 1999; Dutrow and Henry, 1996, 2012). Such a hydrothermal fluid equilibrated with boron-rich metasediments would contain about 0.2 wt.% B₂O₃ at 500°C and 1 kbar (Weisbrod et al., 1986). Devolatilization of metasediments also induces a high boron isotope fractionation of about -10‰ between mica and fluid at 500°C with preferential partitioning of ¹¹B into the expelled metamorphic fluid (Wunder et al., 2005). Considering that the metamorphic fluid had a $\delta^{11}\text{B} = -9.5\text{‰}$, this would imply that the muscovite-bearing rock would have a very light boron isotope composition of $\delta^{11}\text{B} = -19\text{‰}$, which falls in the range of metasedimentary rocks (Ishikawa and Nakamura, 1993; Peacock and Hervig, 1999; Nakano and Nakamura, 2001; Romer and Meixner, 2014; Berryman et al., 2017). To sum up, a magmatic or a metamorphic fluid origin is possible for tourmaline from Puy-les-Vignes according to the boron isotope data.

5.4. Evolution of the hydrothermal system in the Puy-les-Vignes W deposit

Tourmaline formation at Puy-les-Vignes occurred during the pre-ore hydrothermal alteration stage preceding the main brecciation-collapse episode and continued up to vein opening

leading to deposition of wolframite. This boron metasomatism thus represents a protracted process throughout the history of the deposit formation. As previously discussed, the trace element and boron isotopic composition of tourmaline suggest the dominant role of fluid-rock interactions between the metamorphic basement and boron-rich hydrothermal fluids. The fluid evolution of the Puy-les-Vignes ore-forming hydrothermal system is discussed in the following based on geological constraints.

5.4.1. Early greisenization stage (ca. 324 Ma)

Greisen-hosted Tur 1 is interpreted to have formed during the earliest hydrothermal episode known at Puy-les-Vignes, which corresponds to the greisenization of the St-Léonard-de-Noblat paragneisses. Greisen formation is typically related to high-temperature alteration by acidic magmatic fluids released from the apical part of a crystallizing intrusion (Černý et al., 2005). Exsolution of a magmatic volatile phase from a water-saturated and boron-rich (>1 wt.% B₂O₃) peraluminous granitic melt would preferentially partition boron and other lithophile incompatible elements (Li, Rb, Cs, Sn, W, etc.) into the fluid (Audétat et al., 2000; Hervig et al., 2002; Thomas et al., 2003; Schatz et al., 2004). In this regard, Tur 1 has the highest concentrations in Rb (10-80 ppm), Cs (1-5 ppm), and W (4-20 ppm) among all tourmaline. No granitic intrusion spatially and genetically connected to the breccia pipe is known at Puy-les-Vignes. The closest and the only contemporaneous intrusion is the Auriat granite, which is located at about 5 km in the northeast of the deposit (Fig. 1A) and is dated at 324 ± 1 Ma (U-Pb on zircon; Gebauer et al., 1981). A continuous core drilling of 1000 m through the Auriat granite revealed a vertical zoning marked by an upward enrichment in incompatible trace elements (Li, Rb, Cs, Ta, Th, U) reflecting a magmatic differentiation trend, which was later affected by successive hydrothermal alteration events during the Late Carboniferous to Permian (Arniaud et al., 1984; Parneix and Petit, 1991). In particular, late-

magmatic tourmaline has been described as an interstitial phase or filling intracrystalline cracks in plagioclase and K-feldspar from the upper part of the Auriat granite (Parneix and Petit, 1991). These observations would suggest that the granitic melt contained >2 wt.% B₂O₃ allowing crystallization of late-magmatic tourmaline at temperature <750°C (Wolf and London, 1997). Regional geophysical data indicate a NE-SW zone of lower gravity anomaly towards Puy-les-Vignes, suggesting a possible extension of the Auriat granite under the deposit (Melleton et al., 2017). In addition, NE-trending dykes of microgranite crosscutting the enclosing gneisses are located at the intersection with the breccia pipe (Weppe, 1951, 1958). One of these dykes has been dated at 324.7 ± 2.4 Ma (⁴⁰Ar-³⁹Ar on muscovite; Harlaux, 2016), which is compatible with the age of the Auriat granite. These arguments suggest therefore that a peraluminous granitic cupola, possibly related to the nearby Auriat granite, exists beneath the Puy-les-Vignes deposit. This unexposed granite was likely responsible for the release at ca. 324 Ma of early magmatic-hydrothermal fluids, which would have strongly interacted with the overlying gneisses leading to distal greisenization and forming disseminated Tur 1.

5.4.2. Main tourmalinization stage (ca. 324-318 Ma)

The main tourmalinization stage at Puy-les-Vignes produced a tourmaline-rich crackle breccia affecting the enclosing paragneisses and forming the tourmalinite rims (Tur 2), which is interpreted to have resulted from intense fluid-rock interactions between boron-rich hydrothermal fluids and the host-rocks in a fluid-dominated system (i.e. high fluid/rock ratios). This episode is temporally constrained between 324 Ma (⁴⁰Ar-³⁹Ar on muscovite; Cuney et al., 2002) and 318 Ma (U-Pb on wolframite; Harlaux et al., 2018b), but it likely occurred soon after the crystallization of the Auriat granite. The St-Léonard-de-Noblat paragneisses belong to the LGU, which experienced successively two episodes of medium-

696 pressure and medium-temperature metamorphism during the Middle Devonian at ca. 385-375
 697 Ma (650-750°C, 0.7 GPa) and during the Early Carboniferous at ca. 360-350 Ma (550-600°C,
 698 0.8-1 GPa) (Faure et al., 2009a and references therein). Previous works reported that the LGU
 699 gneisses in the northern FMC reached the muscovite-breakdown reaction during the prograde
 700 metamorphic path, resulting in a biotite-sillimanite-stable assemblage, whereas boron
 701 partitioned into the expelled fluid (van Hinsberg and Schumacher, 2011). This is in good
 702 agreement with the mineralogical composition of the migmatitic biotite-sillimanite gneisses
 703 of the St-Léonard-de-Noblat unit, implying that those were boron-depleted during the Middle
 704 Devonian - Early Carboniferous prograde metamorphism prior to the formation of the Puy-
 705 les-Vignes deposit. Consequently, the St-Léonard-de-Noblat paragneisses cannot be
 706 considered as a viable source of boron for the massive tourmalinization stage that occurred
 707 after 324 Ma. An alternative source could be the Dronne micaschists that belong to the PAU
 708 located below the LGU, at the bottom of the three-nappe pile system of the FMC. In the
 709 northern FMC, the PAU crops out locally in tectonic windows surrounded by higher-grade
 710 rocks from the LGU and UGU, and has only been subjected to low-grade metamorphism
 711 (Faure et al., 2009a). During the Late Carboniferous (ca. 320-315 Ma), syn-orogenic crustal
 712 melting and high-grade metamorphism were coeval in the Limousin area as indicated by the
 713 emplacement of two-mica leucogranites into the UGU and LGU and the formation of
 714 cordierite-sillimanite migmatites (Lafon and Respaut, 1988; Cartannaz et al., 2007; Gébelin et
 715 al., 2009; Faure et al., 2009b; Gardien et al., 2011). Although an unexposed peraluminous
 716 leucogranite is a possible source for the boron-rich hydrothermal fluids at Puy-les-Vignes, a
 717 metamorphic fluid origin cannot be ruled out. We propose that devolatilization of the deep-
 718 seated Dronne micaschists in the underlying PAU during the Late Carboniferous may also
 719 represent a potential mechanism for generating boron-rich metamorphic fluids at depth.
 720 Whatever the origin of the fluids (magmatic or metamorphic), the formation of the Puy-les-

Vignes quartz-tourmaline crackle breccia would have been the result of a strong focusing of boron-rich hydrothermal fluids rising upwards at the intersection of crustal faults, yielding to hydraulic fracturing and brecciation of the overlying gneiss carapace, filling the cavities between the clasts, and forming the tourmalinite rims (Tur 2) during fluid-rock interactions.

5.4.3. Hydrothermal W mineralization stage (ca. 318 Ma)

Hydraulic brecciation and mass collapse of the tourmalinite crackle breccia produced a matrix-supported quartz-tourmaline breccia pipe, followed by fluid-assisted reopening and formation of the network of quartz-wolframite±tourmaline (Tur 3) veins. The age of the W mineralization episode is constrained at 317.7 ± 0.7 Ma (U-Pb wolframite age; Harlaux et al., 2018b), i.e more than 6 Ma after the emplacement of the Auriat granite. The mechanism responsible for the brecciation-collapse of the overlying gneisses is unknown. Explosive release of overpressured magmatic fluids from a crystallizing intrusion beneath the deposit is a possible explanation (Sillitoe, 1985; Pollard et al., 1987). This mechanism has generally been proposed for the formation of magmatic-hydrothermal breccia pipes associated with W-Sn mineralization (e.g., Ren et al., 1995; Somarin and Ashley, 2004; Yang and Bodnar, 2004; Solomovich et al., 2012). The trace element composition of wolframite from Puy-les-Vignes has shown increasing concentrations in granitophile elements (Nb, Ta, Sn, Li) from surface down to 300 m at depth, which has been interpreted as the chemical footprint of the spatial proximity with an underlying leucogranite (Harlaux et al., 2018a). Such trend may indicate wolframite precipitation from magmatic or metamorphic fluids having interacting with the basement. This interpretation is likely since several studies reported the importance of fluid-rock interaction as a major process for deposition of wolframite (e.g., Dewaele et al., 2016; Chicharro et al., 2016; Lecumberri-Sanchez et al., 2017). In absence of any evidences arguing for a direct genetic connection of the Puy-les-Vignes breccia pipe to an unexposed

leucogranite emplaced at 318 Ma, the origin (magmatic vs. metamorphic) of the ore-forming hydrothermal fluids must be kept open.

5.4.4. Post-ore hydrothermal stage (ca. 300 Ma)

Tur 4 associated with the adularia and chlorite microbreccia formed during a late hydraulic fracturing episode that post-dated the W mineralization. This event is constrained at 301.3 ± 1.5 Ma (^{40}Ar - ^{39}Ar on adularia; Harlaux, 2016), i.e. more than 20 Ma after the emplacement of the Auriat granite. This age is coeval with the late-Variscan generalized extensional tectonics in the FMC that resulted from the late-orogenic uplift and thinning of the continental crust (Faure et al., 2009a). The 300-305 Ma period is synchronous to the formation of orogenic Au deposits in the Limousin area, which were produced by mixing of metamorphic and meteoric fluids (Boiron et al., 2003; Bouchot et al., 2005). Since no episode of granitic magmatism is known in the Limousin during this period, it is likely that Tur 4 was formed by boron-rich fluids equilibrated with the metamorphic pile. This would imply that the boron isotope composition of metamorphic tourmaline is indistinguishable from the one of tourmaline formed from magmatic-hydrothermal fluids and that caution should be applied when interpreting the fluid sources in granite-related deposits based only on boron isotope compositions of tourmaline.

6. Conclusions

Tourmaline is an important alteration mineral in the Puy-les-Vignes W deposit occurring during pre-, syn-, and post-mineralization stages. The different generations of hydrothermal tourmaline (Tur 1 to Tur 4) belong to the dravite-schorl series and have similar major and trace element compositions plotting in the field of metamorphic rocks. The variable

enrichments in granitophile elements and transition metals in tourmaline suggest a mixed magmatic-metamorphic origin likely related to high-temperature fluid-rock interactions between the metamorphic basement and boron-rich, low salinity, and reduced hydrothermal fluids. Boron isotope variations ($\delta^{11}\text{B} = -13.3\text{‰}$ to -7.8‰) in tourmaline cannot unambiguously distinguish between a magmatic and a metamorphic origin of the hydrothermal fluids. According to existing geochronological data and geological constraints, the Puy-les-Vignes breccia pipe is interpreted to result from a multi-stage evolution involving both magmatic and metamorphic fluids. The release of magmatic-hydrothermal fluids from an unexposed peraluminous leucogranitic cupola at ca. 324 Ma, possibly related to the nearby Auriat granite, is proposed as the main mechanism responsible for formation of greisen tourmaline (Tur 1). Massive tourmalinization and hydraulic fracturing of the host-rocks resulted from extensive interactions between boron-rich hydrothermal fluids and the metasedimentary rocks leading to formation of the tourmalinite rims (Tur 2). Fluid-assisted reopening and collapse of the former tourmalinite at ca. 318 Ma yielded to a superimposed matrix-supported quartz-tourmaline breccia pipe and formation of wolframite-bearing quartz veins and syn-ore tourmaline (Tur 3). Finally, post-ore hydraulic fracturing by boron-rich metamorphic fluids resulted in formation of tourmaline microbreccias (Tur 4) at ca. 300 Ma. We conclude that the trace element and boron isotopic composition of tourmaline from the Puy-les-Vignes deposit was dominantly controlled by fluid-rock interaction between magmatic and/or metamorphic fluids and the country rocks.

Acknowledgements

This work was supported by the French National Research Agency through the national

program "Investissements d'avenir" of the Labex Ressources 21 with the reference ANR-10-LABX-21-RESSOURCES21, and has also taken part of the project ERAMIN "New Ores". The authors would like to thank Dr. Hossein Ahmadzadeh and the Musée Minéralogique de l'Ecole des Mines d'Alès (France) for supplying samples of collection from the Puy-les-Vignes mine. We also thank Sandrine Mathieu, Dr. Andreï Lecomte, Dr. Olivier Rouer, and Dr. Chantal Peiffert (GeoRessources, Vandœuvre-lès-Nancy, France) for technical support in providing analytical data with SEM, EMPA, and LA-ICP-MS. We are also grateful to Dr. Andrey Gurenko and Dr. Etienne Deloule (CRPG-CNRS, Vandœuvre-lès-Nancy, France) for their help during the SIMS analyses. Constructive reviews and suggestions by Dr. Robert Trumbull and another anonymous reviewer greatly improved the quality of the manuscript. We also thank the Editor-in-Chief Prof. Franco Pirajno for the editorial handling.

References

- Alexandre, P., 2007. U–Pb zircon SIMS ages from the French Massif Central and implication for the pre-Variscan tectonic evolution in Western Europe. *C. R. Geosci.* 339, 613-621.
- Alexandrov, P., Floc'h, J.P., Cuney, M., Cheilletz, A., 2001. Datation U–Pb à la microsonde ionique des zircons de l'unité supérieure de gneiss dans le Sud Limousin, Massif central. *CR. Acad. Sci. IIA* 332, 625-632.
- Alikouss, S., 1993. Contribution à l'étude des fluides crustaux : approche analytique et expérimentale. Ph.D. thesis, Institut National Polytechnique de Lorraine, France, 255p.
- Arniaud, D., Dupuy, C., Dostal, J., 1984. Geochemistry of Auriat granite (Massif Central, France). *Chem. Geol.* 45, 263-277.
- Audétat, A., Günther, D., Heinrich, C.A., 2000. Magmatic-hydrothermal evolution in a fractionating granite: A microchemical study of the Sn-W-F-mineralized Mole Granite (Australia). *Geochim. Cosmochim. Ac.* 64, 3373-3393.
- Baker, T., Pollard, P.J., Mustard, R., Mark, G., Graham, J.L., 2005. A comparison of granite-related tin, tungsten, and gold-bismuth deposits: implications for exploration. *SEG Newsletter* 61, 5-17.
- Barker, S.L., Cox, S.F., 2011. Oscillatory zoning and trace element incorporation in hydrothermal minerals: insights from calcite growth experiments. *Geofluids* 11, 48-56.
- Belissant, R., Boiron, M.C., Luais, B., Cathelineau, M., 2014. LA-ICP-MS analyses of minor and trace elements and bulk Ge isotopes in zoned Ge-rich sphalerites from the Noailhac–Saint-Salvy deposit (France): Insights into incorporation mechanisms and ore deposition processes. *Geochim. Cosmochim. Ac.* 126, 518-540.
- Berger, J., Féménias, O., Ohnenstetter, D., Bruguier, O., Plissart, G., Mercier, J.C.C., Demaiffe, D., 2010a. New occurrence of UHP eclogites in Limousin (French Massif

833 Central): age, tectonic setting and fluid–rock interactions. *Lithos* 118, 365-382.

834 Berger, J., Femenias, O., Ohnenstetter, D., Plissart, G., Mercier, J.C., 2010b. Origin and
835 tectonic significance of corundum–kyanite–sapphirine amphibolites from the Variscan
836 French Massif Central. *J. Metamorph. Geol.* 28, 341-360.

837 Berryman, E.J., Kutzschbach, M., Trumbull, R.B., Meixner, A., van Hinsberg, V., Kasemann,
838 S.A., Franz, G., 2017. Tourmaline as a petrogenetic indicator in the Pfitsch Formation,
839 Western Tauern Window, Eastern Alps. *Lithos* 284, 138-155.

840 Blamart, D., Boutaleb, M., Sheppard, S., Marignac, C., Weisbrod, A., 1992. A comparative
841 thermobarometric (chemical and isotopic) study of a tourmalinized pelite and its Sn-Be
842 vein, Walmès, Morocco. *Eur. J. Mineral.* 4, 355-368.

843 Boiron, M.C., Cathelineau, M., Banks, D.A., Fourcade, S., Vallance, J., 2003. Mixing of
844 metamorphic and surficial fluids during the uplift of the Hercynian upper crust:
845 consequences for gold deposition. *Chem. Geol.* 194, 119-141.

846 Bouchot, V., Ledru, P., Lerouge, C., Lescuyer, J.L., Milesi, J.P., 2005. Late Variscan
847 mineralizing systems related to orogenic processes: the French Massif Central. *Ore*
848 *Geol. Rev.* 27, 169-197.

849 Cartannaz, C., 2005. Magmatismes et déformations polyphasés: exemple des massifs de
850 Guéret et de Millevaches (Massif Central Français). Origine des magmas et contexte de
851 mise en place. Ph.D. thesis, Université de Franche-Comté, France, 317p.

852 Cartannaz, C., Rolin, P., Cocherie, A., Marquer, D., Legendre, O., Fanning, C.M., Rossi, P.,
853 2007. Characterization of wrench tectonics from dating of syn-to post-magmatism in the
854 north-western French Massif Central. *Int. J. Earth Sci.* 96, 271-287.

855 Catanzaro, E.J., Champion, C.E., Garner, E.L., Marinenko, G., Sappenfield, K.M., Shields,
856 W.R., 1970. Standard reference materials: boric acid isotopic and assay standard
857 reference materials. US National Bureau of Standards, Special Publication 260-17, 70p.

858 Černý, P., Blevin, P.L., Cuney, M., London, D., 2005. Granite-related Ore Deposits. In
 859 Hedenquist, J.W., Thompson, J.F.H., Goldfarb, R.J., and Richards, J.P., eds., Econ.
 860 Geol. 100th Anniversary Volume 1905-2005, 337–370.

861 Chell-Michou, C., Laurent, O., Moyen, J.F., Block, S., Paquette, J.L., Couzinié, S., Gardien,
 862 V., Vanderhaeghe, O., Villaros, A., Zeh, A., 2017. Pre-Cadomian to late-Variscan
 863 odyssey of the eastern Massif Central, France: Formation of the West European crust in
 864 a nutshell. *Gondwana Res.* 46, 170-190.

865 Chenevoy, M., Constans, J.E., Recoing, M., 1984. Carte géologique à 1/50 000 Saint-
 866 Léonard-de-Noblat et notice explicative. Editions BRGM, 44p.

867 Chicharro, E., Boiron, M.C., López-García, J.Á., Barfod, D.N., Villaseca, C., 2016. Origin,
 868 ore forming fluid evolution and timing of the Logrosán Sn–(W) ore deposits (Central
 869 Iberian Zone, Spain). *Ore Geol. Rev.* 72, 896-913.

870 Codeço, M.S., Weis, P., Trumbull, R.B., Pinto, F., Lecumberri-Sanchez, P., Wilke, F.D., 2017.
 871 Chemical and boron isotopic composition of hydrothermal tourmaline from the
 872 Panasqueira W-Sn-Cu deposit, Portugal. *Chem. Geol.* 468, 1-16.

873 Cuney, M., Alexandrov, P., Le Carlier de Veslud, C., Cheilletz, A., Raimbault, L., Ruffet, G.,
 874 Scaillet, S., 2002. The timing of W-Sn rare-metals mineral deposit formation in the
 875 Western Variscan chain in their orogenic setting: the case of the Limousin area (Massif
 876 Central, France). In: *The Timing and Location of Major Ore Deposits in an Evolving*
 877 *Orogen* (eds. D.J. Blundell, F. Neubauer and A. Von Quadt). *Geol. Soc. London Spec.*
 878 *Publ.* 204, 213-228.

879 Decrée, S., Marignac, C., De Putter, T., Yans, J., Clauer, N., Dermech, M., Aloui, K., Baele, J.
 880 M., 2013. The Oued Belif hematite-rich breccia: A Miocene iron oxide Cu-Au-(U-REE)
 881 deposit in the Nefza mining district, Tunisia. *Econ. Geol.* 108, 1425-1457.

882 Demirel, S., Göncüoğlu, M.C., Topuz, G., Isik, V., 2009. Geology and chemical variations in

883 tourmaline from the quartz–tourmaline breccias within the Kerkenez granite–monzonite
884 massif, Central Anatolian Crystalline Complex, Turkey. *Can. Mineral.* 47, 787-799.

885 Dewaele, S., De Clercq, F., Hulsbosch, N., Piessens, K., Boyce, A., Burgess, R., Muchez, P.,
886 2016. Genesis of the vein-type tungsten mineralization at Nyakabingo (Rwanda) in the
887 Karagwe-Ankole belt, Central Africa. *Miner. Deposita* 51, 283-307.

888 Downes, H., Duthou, J.L., 1988. Isotopic and trace-element arguments for the lower-crustal
889 origin of Hercynian granitoids and pre-Hercynian orthogneisses, Massif Central
890 (France). *Chem. Geol.* 68, 291-308.

891 Drivenes, K., Larsen, R.B., Müller, A., Sørensen, B.E., Wiedenbeck, M., Raanes, M.P., 2015.
892 Late-magmatic immiscibility during batholith formation: assessment of B isotopes and
893 trace elements in tourmaline from the Land's End granite, SW England. *Contrib.*
894 *Mineral. Petr.* 169, 1-27.

895 Dubessy, J., Poty, B., Ramboz, C., 1989. Advances in C-O-H-N-S fluid geochemistry based
896 on micro-Raman spectrometric analysis of fluid inclusions. *Eur. J. Mineral.* 1, 517-534.

897 Duchoslav, M., Marks, M.A.W., Drost, K., McCammon, C., Marschall, H.R., Wenzel, T.,
898 Markl, G., 2017. Changes in tourmaline composition during magmatic and
899 hydrothermal processes leading to tin-ore deposition: The Cornubian Batholith, SW
900 England. *Ore Geol. Rev.* 83, 215-234.

901 Duthou, J.L., 1978. Les granitoïdes du Haut Limousin (Massif central français), chronologie
902 Rb/Sr de leur mise en place; le thermo-métamorphisme carbonifère. *B. Soc. Geol. Fr.*
903 20, 229-235.

904 Dutrow, B.L., Henry, D.J., 2011. Tourmaline: a geological DVD. *Elements* 7, 301-306.

905 Dutrow, B.L., Henry, D.J., 2018. Tourmaline compositions and textures: reflections of the
906 fluid phase. *J. Geosci.* 63, 99-110.

907 Dutrow, B.L., Foster, C.T., Henry, D.J., 1999. Tourmaline-rich pseudomorphs in sillimanite

908 zone metapelites: Demarcation of an infiltration front. *Am. Mineral.* 84, 794-805.

909 Dyar, M.D., Wiedenbeck, M., Robertson, D., Cross, L.R., Delaney, J.S., Ferguson, K.,
910 Francis, C.A., Grew, E.S., Guidotti, C.V., Hervig, R.L., Hughes, J.M., Husler, J.,
911 Leeman, W., McGuire, A.V., Rhede, D., Rothe, H., Paul, R.L., Richards, I., Yates, M.,
912 2001. Reference minerals for the microanalysis of light elements. *Geostandards*
913 *Newslett.* 25, 441-463.

914 Faure, M., Lardeaux, J.M., Ledru, P., 2009a. A review of the pre-Permian geology of the
915 Variscan French Massif Central. *C. R. Geosci.* 341, 202–213.

916 Faure, M., Mezeme, E.B., Cocherie, A., Melleton, J., Rossi, P., 2009b. The South Millevaches
917 Middle Carboniferous crustal melting and its place in the French Variscan belt. *B. Soc.*
918 *Geol. Fr.* 180, 473-481.

919 Galbraith, C.G., Clarke, D.B., Trumbull, R.B., Wiedenbeck, M., 2009. Assessment of
920 tourmaline compositions as an indicator of emerald mineralization at the Tsa da Glisza
921 Prospect, Yukon Territory, Canada. *Econ. Geol.* 104, 713-731.

922 Gardien, V., Vanderhaeghe, O., Arnaud, N., Cocherie, A., Grange, M., Lécuyer, C., 2011.
923 Thermal maturation and exhumation of a middle orogenic crust in the Livradois area
924 (French Massif Central). *B. Soc. Geol. Fr.* 182, 5-24.

925 Gebauer, H., Bernard-Griffiths, J., Gnünfelder, M., 1981. U/Pb zircon and monazite dating
926 of mafic-ultramafic complex and its country rocks. Example: Sauviat-sur-Vige, French
927 Massif Central. *Contrib. Mineral. Petr.* 76, 292-300.

928 Gébelin, A., Roger, F., Brunel, M., 2009. Syntectonic crustal melting and high-grade
929 metamorphism in a transpressional regime, Variscan Massif Central, France.
930 *Tectonophysics* 477, 229-243.

931 Giraud, A., Marchand, J., Dupuy, C., Dostal, J., 1984. Geochemistry of leptyno-amphibolite
932 complex from Haut Allier (French Massif Central). *Lithos* 17, 203-214.

933 Harlaux, M., 2016. Tungsten and Rare-metal (Nb, Ta, Sn) Hydrothermal Metallogenic
 934 Systems in the Late-Variscan Orogenic Context: Example of the French Massif Central.
 935 Ph.D. thesis, Université de Lorraine, France, 576p.

936 Harlaux, M., Marignac, C., Cuney, M., Mercadier, J., 2015a. The Puy-les-Vignes breccia pipe
 937 (Massif Central, France): a unique occurrence of polymetallic W-Nb±Ta-HREE-Bi-Cu-
 938 As±Au-Ag mineralization in the Variscan belt. In Proceedings of the 13th Biennial SGA
 939 Meeting, 24–27 August 2015, Nancy, France (eds. A.S. André-Mayer, M. Cathelineau,
 940 P. Muchez, E. Pirard and S. Sindern), Vol. 2, 749–752.

941 Harlaux, M., Marignac, C., Cuney, M., Mercadier, J., Magott, R., Mouthier, B., 2015b. Nb-Ti-
 942 Y-HREE-W-U oxide minerals with uncommon compositions associated with the
 943 tungsten mineralization in the Puy-les-Vignes deposit (Massif Central, France):
 944 evidence for rare-metal mobilization by late hydrothermal fluids with a peralkaline
 945 signature. *Can. Mineral.* 53, 653-672.

946 Harlaux, M., Mercadier, J., Bonzi, W.M.E., Kremer, V., Marignac, C., Cuney, M., 2017.
 947 Geochemical signature of magmatic-hydrothermal fluids exsolved from the Beauvoir
 948 rare-metal granite (Massif Central, France): insights from LA-ICPMS analysis of
 949 primary fluid inclusions. *Geofluids* 2017, 1–25.

950 Harlaux, M., Mercadier, J., Marignac, C., Peiffert, C., Cloquet, C., Cuney, M., 2018a. Tracing
 951 metal sources in peribatholithic hydrothermal W deposits based on the chemical
 952 composition of wolframite: The example of the Variscan French Massif Central. *Chem.*
 953 *Geol.* 479, 58-85.

954 Harlaux, M., Romer, R.L., Mercadier, J., Morlot, C., Marignac, C., Cuney, M., 2018b. 40 Ma
 955 of hydrothermal W mineralization during the Variscan orogenic evolution of the French
 956 Massif Central revealed by U-Pb dating of wolframite. *Miner. Deposita* 53, 21-51.

957 Hazarika, P., Mishra, B., Pruseth, K.L., 2015. Diverse tourmaline compositions from orogenic

958 gold deposits in the Hutti-Maski greenstone belt, India: implications for sources of ore-
 959 forming fluids. *Econ. Geol.* 110, 337-353.

960 Henry, D.J., Dutrow, B.L., 1996. Metamorphic tourmaline and its petrologic applications. In
 961 Boron: mineralogy, petrology and geochemistry (Grew, E.S. and Anovitz, L.M. eds.).
 962 *Rev. Mineral.* 33, 503–557.

963 Henry, D.J., Dutrow, B.L., 2012. Tourmaline at diagenetic to low-grade metamorphic
 964 conditions: Its petrologic applicability. *Lithos* 154, 16-32.

965 Henry, D.J., Guidotti, C.V., 1985. Tourmaline as a petrogenetic indicator mineral: an example
 966 from the staurolite-grade metapelites of NW Maine. *Am. Mineral.* 70, 1-15.

967 Henry, D.J., Novák, M., Hawthorne, F.C., Ertl, A., Dutrow, B.L., Uher, P., Pezzotta, F., 2011.
 968 Nomenclature of the tourmaline-supergroup minerals. *Am. Mineral.* 96, 895-913.

969 Hervig, R.L., Moore, G.M., Williams, L.B., Peacock, S.M., Holloway, J.R., Roggensack, K.,
 970 2002. Isotopic and elemental partitioning of boron between hydrous fluid and silicate
 971 melt. *Am. Mineral.* 87, 769-774.

972 Holten, T., Jamtveit, B., Meakin, P., Cortini, M., Blundy, J., Austrheim, H., 1997. Statistical
 973 characteristics and origin of oscillatory zoning in crystals. *Am. Mineral.* 82, 596-606.

974 Hong, W., Cooke, D.R., Zhang, L., Fox, N., Thompson, J., 2017. Tourmaline-rich features in
 975 the Heemskirk and Pieman Heads granites from western Tasmania, Australia:
 976 Characteristics, origins, and implications for tin mineralization. *Am. Mineral.* 102, 876-
 977 899.

978 Hulsbosch, N., Boiron, M.C., Dewaele, S., Muchez, P., 2016. Fluid fractionation of tungsten
 979 during granite–pegmatite differentiation and the metal source of peribatholithic W quartz
 980 veins: Evidence from the Karagwe-Ankole Belt (Rwanda). *Geochim. Cosmochim.*
 981 *Ac.* 175, 299-318.

982 Izenman, A.J., 2008. Modern multivariate statistical techniques. Regression, classification,

983 and Manifold learning. Springer-Verlag, New York, 733 p.

984 Ishikawa, T., Nakamura, E., 1993. Boron isotope systematics of marine sediments. *Earth*
985 *Planet. Sc. Lett.* 117, 567-580.

986 Jiang, S.Y., Yu, J.M., Lu, J.J., 2004. Trace and rare-earth element geochemistry in tourmaline
987 and cassiterite from the Yunlong tin deposit, Yunnan, China: implication for migmatitic–
988 hydrothermal fluid evolution and ore genesis. *Chem. Geol.* 209, 193-213.

989 Jiang, S.Y., Radvanec, M., Nakamura, E., Palmer, M., Kobayashi, K., Zhao, H-X., Zhao, K-
990 D., 2008. Chemical and boron isotopic variations of tourmaline in the Hnilec granite-
991 related hydrothermal system, Slovakia: Constraints on magmatic and metamorphic fluid
992 evolution. *Lithos* 106, 1-11.

993 Jochum, K.P., Weis, U., Stoll, B., Kuzmin, D., Yang, Q., Raczek, I., Jacob, D.E., Stracke, A.,
994 Birbaum, K., Frick, D.A., Günther, D., Enzweiler, J., 2011. Determination of reference
995 values for NIST SRM 610-617 glasses following ISO guidelines. *Geostand. Geoanal.*
996 *Res.* 35, 397–429.

997 Kalliomäki, H., Wagner, T., Fusswinkel, T., Sakellaris, G., 2017. Major and trace element
998 geochemistry of tourmalines from Archean orogenic gold deposits: Proxies for the
999 origin of gold mineralizing fluids?. *Ore Geol. Rev.* 91, 906-927.

1000 Kawakami, T., Ikeda, T., 2003. Boron in metapelites controlled by the breakdown of
1001 tourmaline and retrograde formation of borosilicates in the Yanai area, Ryoke
1002 metamorphic belt, SW Japan. *Contrib. Mineral. Petr.* 145, 131-150.

1003 Lafon, J.M., Respaut, J.P., 1988. Géochronologie U-Pb et leucogranites varisques: cas des
1004 massifs de Grandrieu (Lozère) et de la Porcherie (Limousin), Massif Central Français.
1005 *B. Mineral.* 111, 225-237.

1006 Launay, G., Sizaret, S., Guillou-Frottier, L., Gloaguen, E., Pinto, F., 2018. Deciphering fluid
1007 flow at the magmatic-hydrothermal transition: A case study from the world-class

1008 Panasqueira W–Sn–(Cu) ore deposit (Portugal). *Earth Planet. Sc. Lett.* 499, 1-12.

1009 Lecumberri-Sanchez, P., Vieira, R., Heinrich, C.A., Pinto, F., Wälle, M., 2017. Fluid-rock
1010 interaction is decisive for the formation of tungsten deposits. *Geology* 45, 579-582.

1011 Leeman, W.P., Sisson, V.B., 1996. Geochemistry of boron and its implications for crustal and
1012 mantle processes. In *Boron: mineralogy, petrology and geochemistry* (Grew, E.S. and
1013 Anovitz, L.M. eds). *Rev. Mineral.* 33, 645–707.

1014 Leeman, W.P., Tonarini, S., 2001. Boron isotopic analysis of proposed borosilicate mineral
1015 reference samples. *Geostandards Newslett.* 25, 399-403.

1016 Leger, J.M., Wang, X., Lameyre, J., 1990. Les leucogranites de Saint-Goussaud en Limousin :
1017 pétrographie, éléments majeurs et traces dans le sondage de Villechabrolle (projet
1018 Energeroc). *B. Soc. Geol. Fr.* 6, 515-524.

1019 Lerouge, C., Bouchot, V., 2009. Conditions of formation and origin of fluids of quartz-
1020 tourmaline veins in the La Châtaigneraie tungstiferous district (Massif Central, France):
1021 fluid inclusions and stable isotopes. *B. Soc. Geol. Fr.* 180, 263-270.

1022 L’Heureux, I., Jamtveit, B., 2002. A model of oscillatory zoning in solid solutions grown from
1023 aqueous solutions: Applications to the (Ba, Sr) SO₄ system. *Geochim. Cosmochim. Ac.*
1024 66, 417-429.

1025 London, D., Manning, D.A.C., 1995. Chemical variation and significance of tourmaline from
1026 southwest England. *Econ. Geol.* 90, 495-519.

1027 Longerich, H.P., Jackson, S.E., Günther, D., 1996. Laser ablation inductively coupled plasma
1028 mass spectrometric transient signal data acquisition and analyte concentration
1029 calculation. *J. Anal. Atom. Spectrom.* 11, 899-904.

1030 Mahjoubi, E.M., Chauvet, A., Badra, L., Sizaret, S., Barbanson, L., El Maz, A., Chen, Y.,
1031 Amann, M., 2016. Structural, mineralogical, and paleoflow velocity constraints on
1032 Hercynian tin mineralization: the Achmmach prospect of the Moroccan Central Massif.

1033 Miner. Deposita 51, 431-451.

1034 Marignac, C., Cuney, M., 1999. Ore deposits of the French Massif Central: insight into the
1035 metallogensis of the Variscan collision belt. Miner. Deposita 34, 472-504.

1036 Marignac, C., Zouhair, M., 1992. Fluid evolution in an unmineralized greisen-tourmaline
1037 system in the Ment granite (central Morocco): a fluid-inclusion study. Eur. J. Mineral. 4,
1038 949-964.

1039 Marks, M.A., Marschall, H.R., Schühle, P., Guth, A., Wenzel, T., Jacob, D.E., Barth, M.,
1040 Markl, G., 2013. Trace element systematics of tourmaline in pegmatitic and
1041 hydrothermal systems from the Variscan Schwarzwald (Germany): the importance of
1042 major element composition, sector zoning, and fluid or melt composition. Chem. Geol.
1043 344, 73-90.

1044 Marschall, H.R., Jiang, S.Y., 2011. Tourmaline isotopes: no element left behind. Elements 7,
1045 313-319.

1046 Melleton, J., Cocherie, A., Faure, M., Rossi, P., 2010. Precambrian protoliths and Early
1047 Paleozoic magmatism in the French Massif Central: U-Pb data and the North Gondwana
1048 connection in the west European Variscan belt. Gondwana Res. 17, 13-25.

1049 Melleton, J., Gloaguen, E., Tourlière, B., Martelet, G., 2017. Promotion des districts miniers
1050 métropolitains. Le district à tungstène de Puy-les-Vignes (87). Rapport BRGM/RP-
1051 66905-FR, 46 p.

1052 Meyer, C., Wunder, B., Meixner, A., Romer, R.L., Heinrich, W., 2008. Boron-isotope
1053 fractionation between tourmaline and fluid: an experimental re-investigation. Contrib.
1054 Mineral. Petr. 156, 259-267.

1055 Mlynarczyk, M.S., Williams-Jones, A.E., 2006. Zoned tourmaline associated with cassiterite:
1056 implications for fluid evolution and tin mineralization in the San Rafael Sn–Cu deposit,
1057 southeastern Peru. Can. Mineral. 44, 347-365.

1058 Moran, A.E., Sisson, V.B., Leeman, W.P., 1992. Boron depletion during progressive
1059 metamorphism: implications for subduction processes. *Earth Planet. Sc. Lett.* 111, 331-
1060 349.

1061 Morgan, G.B., London, D., 1989. Experimental reactions of amphibolite with boron-bearing
1062 aqueous fluids at 200 MPa: implications for tourmaline stability and partial melting in
1063 mafic rocks. *Contrib. Mineral. Petr.* 102, 281-297.

1064 Mouthier, B., 2005. La mine de tungstène de Puy-les-Vignes (Haute-Vienne). *Connaissance et*
1065 *Sauvegarde de Saint-Léonard*, 2^e édition, 256p.

1066 Nakano, T., Nakamura, E., 2001. Boron isotope geochemistry of metasedimentary rocks and
1067 tourmalines in a subduction zone metamorphic suite. *Phys. Earth Planet. In.* 127, 233-
1068 252.

1069 Palmer, M.R., Slack, J.F., 1989. Boron isotopic composition of tourmaline from massive
1070 sulfide deposits and tourmalinites. *Contrib. Mineral. Petr.* 103, 434-451.

1071 Parneix, J.C., Petit, J.C., 1991. Hydrothermal alteration of an old geothermal system in the
1072 Auriat granite (Massif Central, France): petrological study and modelling. *Chem. Geol.*
1073 89, 329-351.

1074 Peacock, S.M., Hervig, R.L., 1999. Boron isotopic composition of subduction-zone
1075 metamorphic rocks. *Chem. Geol.* 160, 281-290.

1076 Pesquera, A., Torres-Ruiz, J., Gil-Crespo, P.P., Jiang, S.Y., 2005. Petrographic, chemical and
1077 B-isotopic insights into the origin of tourmaline-rich rocks and boron recycling in the
1078 Martinamor Antiform (Central Iberian Zone, Salamanca, Spain). *J. Petr.* 46, 1013-1044.

1079 Pollard, P.J., Pichavant, M., Charoy, B., 1987. Contrasting evolution of fluorine- and boron-
1080 rich tin systems. *Miner. Deposita* 22, 315-321.

1081 Raith, J. G., Riemer, N., Meisel, T., 2004. Boron metasomatism and behaviour of rare earth
1082 elements during formation of tourmaline rocks in the eastern Arunta Inlier, central

- 1083 Australia. *Contrib. Mineral. Petr.* 147, 91-109.
- 1084 Ramboz, C., Schnapper, D., Dubessy, J., 1985. The P-V-T-X-fO₂ evolution of H₂O-CO₂-CH₄-
 1085 bearing fluid in a wolframite vein: Reconstruction from fluid inclusion studies.
 1086 *Geochim. Cosmochim. Ac.* 49, 205-219.
- 1087 Ren, S.K., Walshe, J.L., Paterson, R.G., Both, R.A., Andrew, A., 1995. Magmatic and
 1088 hydrothermal history of the porphyry-style deposits of the Ardlethan tin field, New
 1089 South Wales, Australia. *Econ. Geol.* 90, 1620-1645.
- 1090 Ribeiro da Costa, I., Mourão, C., Récio, C., Guimarães, F., Antunes, I.M., Farinha Ramos, J.,
 1091 Barriga, F.J.A.S., Palmer, M.R., Milton, J.A., 2014. Tourmaline occurrences within the
 1092 Penamacor-Monsanto granitic pluton and host-rocks (Central Portugal): genetic
 1093 implications of crystal-chemical and isotopic features. *Contrib. Mineral. Petr.* 167, 1-23.
- 1094 Romer, R.L., Meixner, A., 2014. Lithium and boron isotopic fractionation in sedimentary
 1095 rocks during metamorphism—the role of rock composition and protolith mineralogy.
 1096 *Geochim. Cosmochim. Ac.* 128, 158-177.
- 1097 Rudnick, R.L., Gao, S., 2003. Composition of the Continental Crust. In *Treatise on*
 1098 *Geochemistry* Vol. 3 (Eds. Rudnick, R.L.). Elsevier, Amsterdam, pp 1–64.
- 1099 Schatz, O.J., Dolejš, D., Stix, J., Williams-Jones, A.E., Layne, G.D., 2004. Partitioning of
 1100 boron among melt, brine and vapour in the system haplogranite-H₂O-NaCl at 800°C
 1101 and 100 MPa. *Chem. Geol.* 210, 135-147.
- 1102 Shore, M., Fowler, A.D., 1996. Oscillatory zoning in minerals; a common phenomenon. *Can.*
 1103 *Mineral.* 34, 1111-1126.
- 1104 Shtukenberg, A.G., Punin, Y.O., 2011. Micromorphological instability of a growing face as a
 1105 source of oscillatory zoning in crystals. *Mineral. Mag.* 75, 169-183.
- 1106 Sillitoe, R., 1985. Ore-related breccias in volcanoplutonic arcs. *Econ. Geol.* 80, 1467-1514.
- 1107 Slack, J.F., Trumbull, R., 2011. Tourmaline as a recorder of ore-forming processes. *Elements*

1108 7, 321-326.

1109 Smith, M.P., Yardley, B.W.D., 1996. The boron isotopic composition of tourmaline as a guide
 1110 to fluid processes in the southwestern England orefield: an ion microprobe study.
 1111 *Geochim. Cosmochim. Ac.* 60, 1415-1427.

1112 Solgadi, F., Moyen, J.F., Vanderhaeghe, O., Sawyer, E.W., Reisberg, L., 2007. The role of
 1113 crustal anatexis and mantle-derived magmas in the genesis of synorogenic Hercynian
 1114 granites of the Livradois area, French Massif Central. *Can. Mineral.* 45, 581-606.

1115 Solomovich, L.I., Trifonov, B.A., Sabelnikov, S.E., 2012. Geology and mineralization of the
 1116 Uchkoshkon tin deposit associated with a breccia pipe, Eastern Kyrgyzstan. *Ore Geol.*
 1117 *Rev.* 44, 59-69.

1118 Somarin, A.K., Ashley, P., 2004. Hydrothermal alteration and mineralisation of the Glen Eden
 1119 Mo-W-Sn deposit: a leucogranite-related hydrothermal system, Southern New England
 1120 Orogen, NSW, Australia. *Miner. Deposita* 39, 282-300.

1121 Thomas, R., Förster, H-J., Heinrich, W., 2003. The behaviour of boron in a peraluminous
 1122 granite-pegmatite system and associated hydrothermal solutions: a melt and fluid-
 1123 inclusion study. *Contrib. Mineral. Petr.* 144, 457-472.

1124 Tindle, A.G., Breaks, F.W., Selway, J.B., 2002. Tourmaline in petalite-subtype granitic
 1125 pegmatites: evidence of fractionation and contamination from the Pakeagama Lake and
 1126 Separation Lake areas of northwestern Ontario, Canada. *Can. Mineral.* 40, 753-788.

1127 Torres-Ruiz, J., Pesquera, A., Gil-Crespo, P.P., Velilla, N., 2003. Origin and petrogenetic
 1128 implications of tourmaline-rich rocks in the Sierra Nevada (Betic Cordillera,
 1129 southeastern Spain). *Chem. Geol.* 197, 55-86.

1130 Trumbull, R.B., Slack, J.F., 2018. Boron isotopes in the continental crust: granites,
 1131 pegmatites, felsic volcanic rocks, and related ore deposits. In: Marschall, H.R., Foster,
 1132 G.L. (Eds.), *Boron Isotopes - The Fifth Element. Advances in Isotope Geochemistry*,

1133 Springer-Verlag, pp. 249-272.

1134 Trumbull, R.B., Beurlen, H., Wiedenbeck, M., Soares, D.R., 2013. The diversity of B-isotope
 1135 variations in tourmaline from rare-element pegmatites in the Borborema Province of
 1136 Brazil. *Chem. Geol.* 352, 47-62.

1137 Trumbull, R.B., Garda, G.M., Xavier, R.P., Cavalcanti, J.A.D., Codeço, M.S., 2019.
 1138 Tourmaline in the Passagem de Mariana gold deposit (Brazil) revisited: major-element,
 1139 trace-element and B-isotope constraints on metallogenesis. *Miner. Deposita* 54, 395-
 1140 414.

1141 Vallance, J., Cathelineau, M., Marignac, C., Boiron, M.C., Fourcade, S., Martineau, F., Fabre,
 1142 C., 2001. Microfracturing and fluid mixing in granites: W–(Sn) ore deposition at Vaulry
 1143 (NW French Massif Central). *Tectonophysics* 336, 43-61.

1144 Van Daele, J., Hulsbosch, N., Dewaele, S., Boiron, M.C., Piessens, K., Boyce, A., Muchez, P.,
 1145 2018. Mixing of magmatic-hydrothermal and metamorphic fluids and the origin of
 1146 peribatholithic Sn vein-type deposits in Rwanda. *Ore Geol. Rev.* 101, 481-501.

1147 van Hinsberg, V.J., 2011. Preliminary experimental data on trace-element partitioning
 1148 between tourmaline and silicate melt. *Can. Mineral.* 49, 153-163.

1149 van Hinsberg, V.J., Schumacher, J.C., 2011. Tourmaline as a petrogenetic indicator mineral in
 1150 the Haut-Allier metamorphic suite, Massif Central, France. *Can. Mineral.* 49, 177-194.

1151 van Hinsberg, V.J., Henry, D.J., Marschall, H.R., 2011. Tourmaline: an ideal indicator of its
 1152 host environment. *Can. Mineral.* 49, 1-16.

1153 Villaros A., Pichavant M., 2019. Mica-liquid trace elements partitioning and the granite-
 1154 pegmatite connection: The St-Sylvestre complex (Western French Massif Central).
 1155 *Chem. Geol.* 528. <https://doi.org/10.1016/j.chemgeo.2019.07.040>

1156 von Goerne, G., Franz, G., Heinrich, W., 2001. Synthesis of tourmaline solid solutions in the
 1157 system Na₂O–MgO–Al₂O₃–SiO₂–B₂O₃–H₂O–HCl and the distribution of Na between

1158 tourmaline and fluid at 300 to 700°C and 200 MPa. *Contrib. Mineral. Petr.* 141, 160-
1159 173.

1160 von Goerne, G., Franz, G., van Hinsberg, V.J., 2011. Experimental determination of Na–Ca
1161 distribution between tourmaline and fluid in the system CaO–Na₂O–MgO–Al₂O₃–SiO₂–
1162 B₂O₃–H₂O. *Can. Mineral.* 49, 137-152.

1163 Weisbrod, A., Polak, C., Roy, D., 1986. Experimental study of tourmaline solubility in the
1164 system Na–Mg–Al–Si–B–O–H. Applications to the boron content of natural
1165 hydrothermal fluids and tourmalinization processes. In *International Symposium on*
1166 *Experimental Mineralogy and Geochemistry (Nancy)*, Abstracts vol., 140–141.

1167 Weppe, M., 1951. Contribution à l'étude des gîtes de tungstène français : Puy-les-Vignes
1168 (Haute Vienne), La Châtaigneraie (Cantal). *Revue de Géologie appliquée et de*
1169 *Prospection minière*. Société d'Impressions Typographiques, Nancy, 210p.

1170 Weppe, M., 1958. Contribution à la géologie minière et à la minéralogie minière. Les
1171 gisements de wolfram de Leucamp, Puy-les-Vignes, Montbelleux. Société
1172 d'Impressions Typographiques, Nancy, 196p.

1173 Wilke, M., Nabelek, P.I., Glascock, M.D., 2002. B and Li Proterozoic metapelites from the
1174 Black Hills, U.S.A.: Implications for the origin of leucogranitic magmas. *Am. Mineral.*
1175 87, 491-500.

1176 Williamson, B.J., Spratt, J., Adams, J.T., Tindle, A.G., Stanley, C.J., 2000. Geochemical
1177 constraints from zoned hydrothermal tourmalines on fluid evolution and Sn
1178 mineralization: an example from fault breccias at Roche, SW England. *J. Petr.* 41, 1439-
1179 1453.

1180 Williamson, B.J., Müller, A., Shail, R.K., 2010. Source and partitioning of B and Sn in the
1181 Cornubian batholith of southwest England. *Ore Geol. Rev.* 38, 1-8.

1182 Winderbaum, L., Ciobanu, C.L., Cook, N.J., Paul, M., Metcalfe, A., Gilbert, S., 2012.

1183 Multivariate analysis of an LA-ICP-MS trace element dataset for pyrite. *Math. Geosci.*
 1184 44, 823-842.

1185 Wolf, M.B., London, D., 1997. Boron in granitic magmas: stability of tourmaline in
 1186 equilibrium with biotite and cordierite. *Contrib. Mineral. Petr.* 130, 12–30.

1187 Wunder, B., Meixner, A., Romer, R.L., Wirth, R., Heinrich, W., 2005. The geochemical cycle
 1188 of boron: constraints from boron isotope partitioning experiments between mica and
 1189 fluid. *Lithos* 84, 206-216.

1190 Yang, K., Bodnar, R.J., 2004. Orthomagmatic origin for the Ilkwang Cu–W breccia-pipe
 1191 deposit, southeastern Kyongsang Basin, South Korea. *J. Asian Earth Sci.* 24, 259-270.

1192 Yang, S.Y., Jiang, S.Y., Zhao, K.D., Dai, B.Z., Yang, T., 2015. Tourmaline as a recorder of
 1193 magmatic–hydrothermal evolution: an in situ major and trace element analysis of
 1194 tourmaline from the Qitianling batholith, South China. *Contrib. Mineral. Petr.* 170, 42.
 1195

Figure captions

Fig. 1. (A) Geological setting and location of the Puy-les-Vignes (PLV) deposit in the Limousin area, northwest French Massif Central (FMC) (modified from Chenevoy et al., 1984). (B) Close-up sketch of the breccia pipe structure at surface (modified from Weppe, 1951).

Fig. 2. Mineralogical and textural features of tourmaline from the Puy-les-Vignes deposit. (A) Typical clast of greisenized gneiss (Gr) rimmed by a cm-thick aureole of black tourmalinite and cemented by quartz (sample PLV-7571). (B) Greisen tourmaline (Tur 1) disseminated in cluster within secondary quartz and muscovite assemblage (sample PLV-02-08a; plane-polarized transmitted light). (C) Tourmalinite on a gneissic clast (Tur 2a) composed by the aggregation of tourmaline crystals cemented by macrocrystalline quartz (sample PLV-02-01a; plane-polarized transmitted light). (D) Tourmalinite on a granitic clast (Tur 2b) showing a sharp contact with the quartz of the breccia (sample PLV-02-04a; plane-polarized transmitted light). (E) Acicular tourmaline (Tur 3) disseminated in a wolframite-bearing quartz vein (sample PLV-02-01c; plane-polarized transmitted light). (F) Microbreccia tourmaline (Tur 4) cemented by adularia and chlorite (sample PLV-02-13b; plane-polarized transmitted light). Mineral abbreviations according to the IMA: Ad=Adularia, Chl=Chlorite, Fe-ox=Fe-oxide, Ms=Muscovite, Qtz=Quartz, Tur=Tourmaline.

Fig. 3. Backscattered electron images of tourmaline from the Puy-les-Vignes deposit. (A) Greisen tourmaline (Tur 1) associated with secondary quartz and muscovite (sample PLV-02-08a). (B) Tourmaline on a gneissic clast (Tur 2a), composed by a core and rim surrounded by an overgrowth showing oscillatory zoning (sample PLV-02-01a). (C) Tourmaline on a granitic

1221 clast (Tur 2b) showing a core-rim zoning and corrosion (sample PLV-02-04a). (D) Detail
 1222 view of late corrosion cutting the crystalline borders of tourmaline (sample PLV-02-04a). (E)
 1223 Section of acicular tourmaline (Tur 3) perpendicular to the c-axis showing sector zoning
 1224 (sample PLV-02-15). (F) Microbreccia tourmaline (Tur 4) cemented by adularia and chlorite
 1225 and showing internal zoning (sample PLV-02-13b). Mineral abbreviations according to the
 1226 IMA: Ad=Adularia, Chl=Chlorite, Fe-ox=Fe-oxide, Ms=Muscovite, Qtz=Quartz,
 1227 Tur=Tourmaline. The numbers refer to the tourmaline zoning: (i) core, (ii) rim, (iii)
 1228 overgrowth, and (iv) corrosion.

1229

1230 **Fig. 4.** Backscattered electron image (BSE) of a zoned tourmaline from a tourmalinized
 1231 gneissic clast (Tur 2a) and corresponding X-ray element maps for Mg, Fe, Ti, Ca, and F
 1232 (sample PLV-02-01a).

1233

1234 **Fig. 5.** Chemical compositions of tourmaline from Puy-les-Vignes plotted in the Ca-X□-
 1235 Na+K ternary diagrams (A-D; after Henry et al., 2011) and in the Al-Fe-Mg ternary diagrams
 1236 (E-H; after Henry and Guidotti, 1985). Tur 1: Greisen tourmaline (samples PLV-02-08a and
 1237 PV-5b). Tur 2a: Tourmalinite on gneissic clasts (sample PLV-02-01a); Tur 2b: Tourmalinite
 1238 on granitic clasts (sample PLV-02-04a). Tur 3: Acicular tourmaline in wolframite-bearing
 1239 quartz veins (samples PLV-02-01c and PLV-02-15). Tur 4: Microbreccia tourmaline
 1240 associated with adularia and chlorite (samples PLV-02-13a/b). The numbered fields in the Al-
 1241 Al₅₀Fe₅₀-Al₅₀Mg₅₀ diagrams correspond to the compositional range of tourmaline from
 1242 different rock types as defined by Henry and Guidotti (1985): (1) Li-rich granitoids,
 1243 pegmatites and aplites; (2) Li-poor granitoids, pegmatites and aplites; (3) Fe³⁺-rich quartz-
 1244 tourmaline rocks (hydrothermally altered granites); (4) Al-rich metapelites and
 1245 metapsammites; (5) Al-poor metapelites and metapsammites; (6) Fe³⁺-rich quartz-tourmaline

rocks, calc-silicate rocks and metapelites; (7) Low-Ca meta-ultramafics and Cr-V-rich metasediments; (8) Meta-carbonates and meta-pyroxenites.

Fig. 6. Compositional variation diagrams of tourmaline from Puy-les-Vignes showing the $X_{\square}/(X_{\square}+Na)$ vs. $Fe/(Fe+Mg)$ atomic ratios (A-D) and Mg vs. Fe in atoms per formula unit (apfu) (E-H). Exchange vectors are indicated by arrows.

Fig. 7. Concentrations of selected trace elements in tourmaline from Puy-les-Vignes ordered by generations (Tur 1 to Tur 4).

Fig. 8. Multi-element diagrams of tourmaline from Puy-les-Vignes normalized to the upper continental crust (UCC from Rudnick and Gao, 2003). The coloured fields correspond to the minimum and maximum values range. Trace elements are grouped by geochemical affinity (after Decrée et al., 2013).

Fig. 9. Principal component analysis (PCA) of the LA-ICP-MS log-transformed dataset of trace element contents in tourmaline from Puy-les-Vignes (n=116 spot analyses, 18 variables). See text for discussion.

Fig. 10. Variation diagrams of selected trace elements in tourmaline from Puy-les-Vignes.

Fig. 11. Boron isotope compositions of tourmaline from Puy-les-Vignes. (A) Histogram showing the $\delta^{11}B$ distribution of the different tourmaline generations (Tur 1 to Tur 4) with distinction of the intracrystalline zones (core, rim, overgrowth). (B) $\delta^{11}B$ variations in tourmaline ordered by generations (Tur 1 to Tur 4). The $\delta^{11}B$ value of $-11.4 \pm 1.5\%$ represents

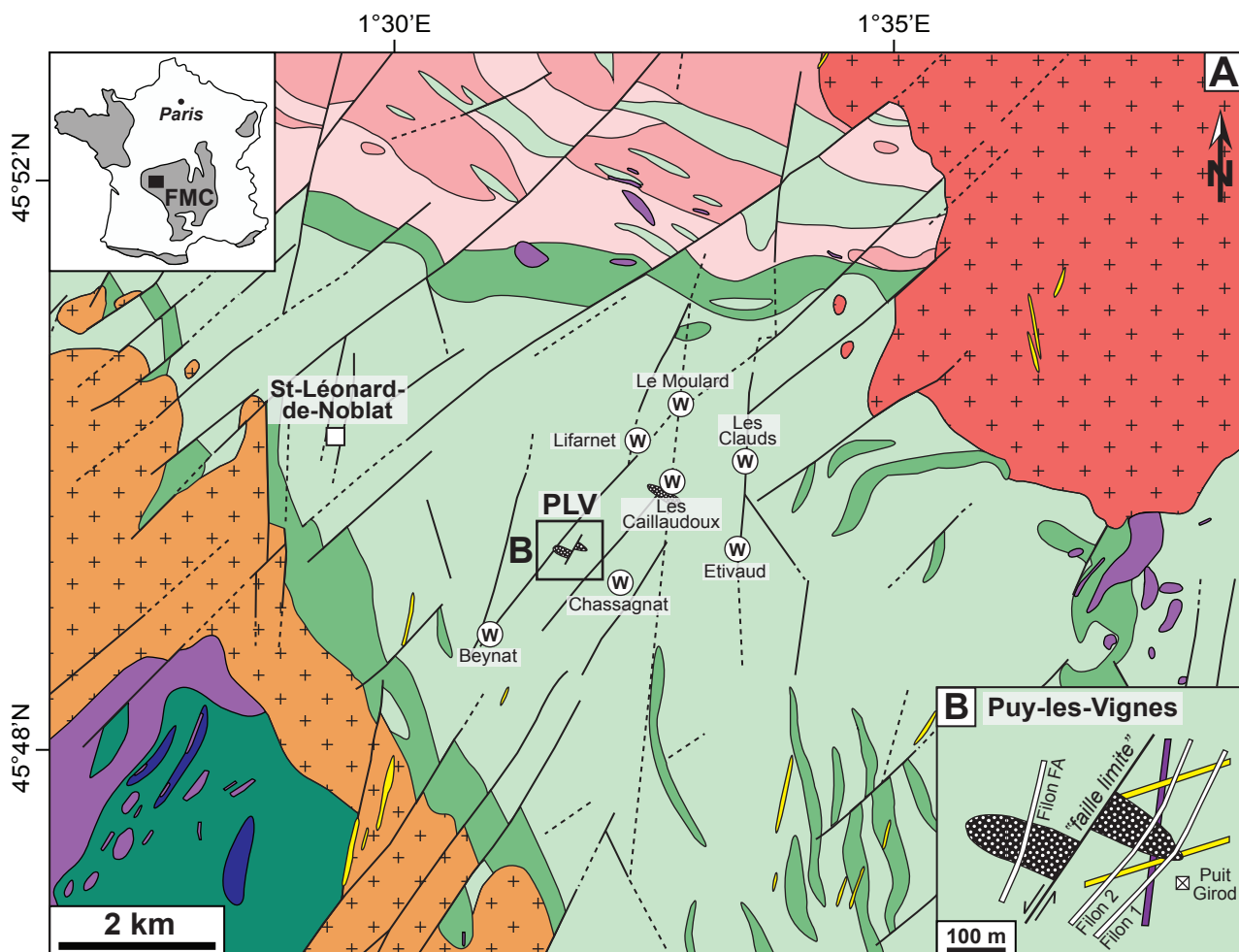
the average of all tourmaline $\delta^{11}\text{B}$ values. (C) $\delta^{11}\text{B}$ composition ranges of tourmaline hosted in variable lithologies worldwide (after Marschall and Jiang, 2011; Trumbull and Slack, 2018).

Fig. 12. Compositional zoning in a single grain of tourmaline from a massive tourmalinite (Tur 2a; sample PLV-02-01a). (A) Backscattered electron image of a tourmaline grain sectioned perpendicular to the c-axis. Internal zoning is underlined with black dashed lines. (B) Detail view of the oscillatory zoning at the micrometre-scale along the external overgrowth with location of the microanalyses. (C) Corresponding compositional variations in tourmaline along the zoning expressed in atom per formula unit (apfu).

Fig. 13. Selected trace elements in tourmaline from Puy-les-Vignes as function of the Li/Sr ratio compared to compositions of worldwide tourmaline hosted in granites (Drivenes et al., 2015; Yang et al., 2015; Duchoslav et al., 2017; Hong et al., 2017; Kalliomäki et al., 2017), metasediments (van Hinsberg and Schumacher, 2011; Hazarika et al., 2015; Kalliomäki et al., 2017; Trumbull et al., 2019), and metavolcanics (Galbraith et al., 2009; Hazarika et al., 2015; Kalliomäki et al., 2017).

Fig. 14. Average trace element and REE compositions of tourmaline from Puy-les-Vignes compared to the whole-rock compositions of the main lithologies in the northwestern French Massif Central, normalized to the upper continental crust values (UCC from Rudnick and Gao, 2003). The lines correspond to the average of the data and the coloured fields correspond to the minimum and maximum value ranges. Source of the data: St-Sylvestre granite: Villaros and Pichavant (2019), Leger et al. (1990) – Guéret granite: Cartannaz (2005) – Lower Gneiss Unit (LGU) para- and orthogneisses: Cartannaz (2005), van Hinsberg and

1296 Schumacher (2011), Downes and Duthou (1988) – Upper Gneiss Unit (UGU) para- and
1297 orthogneisses: Solgadi et al. (2007) – UGU ophiolites and eclogites: Berger et al. (2010a,
1298 2010b) – UGU Leptyno-amphibolite complex: Giraud et al. (1984).
1299
1300



LEGEND

Carboniferous intrusions

- Auriat granite (ca. 324 Ma)
- Aureil granite (ca. 346 Ma)

Upper Gneiss Unit (UGU)

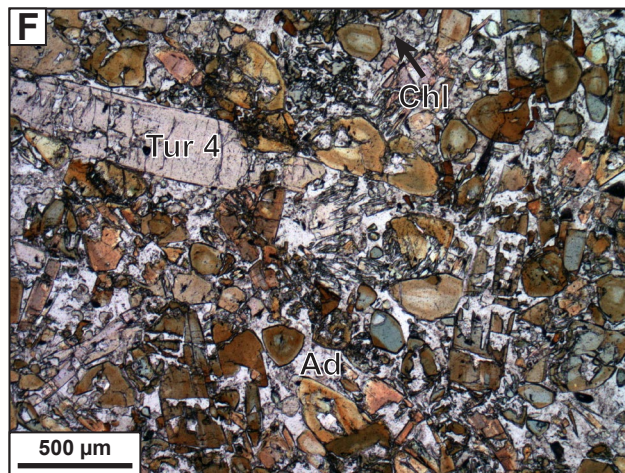
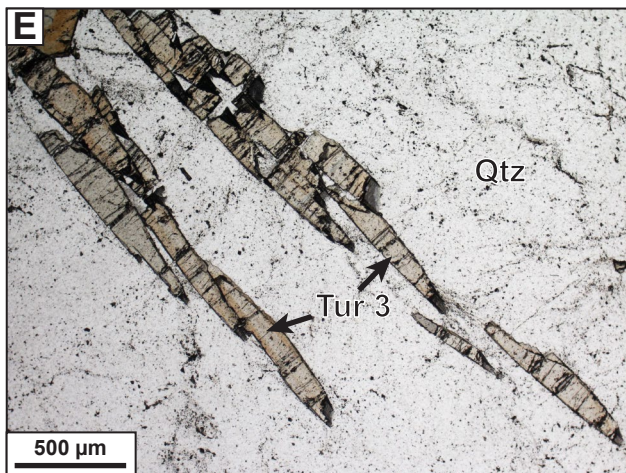
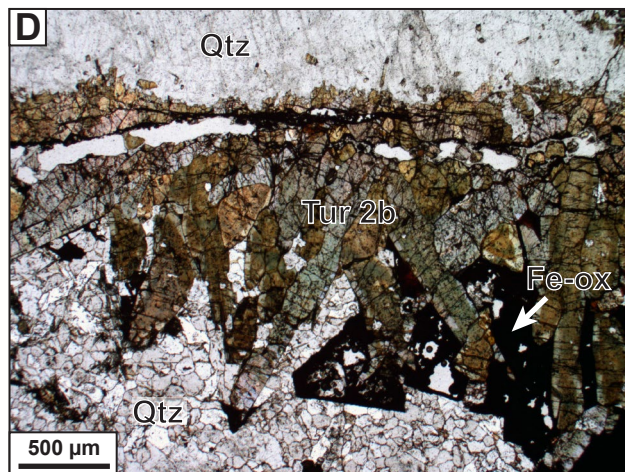
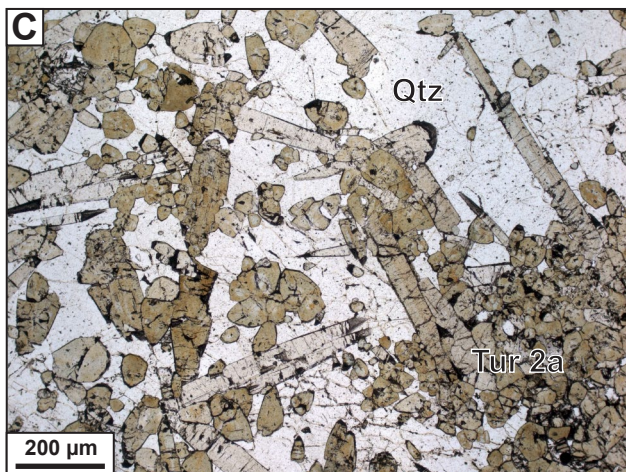
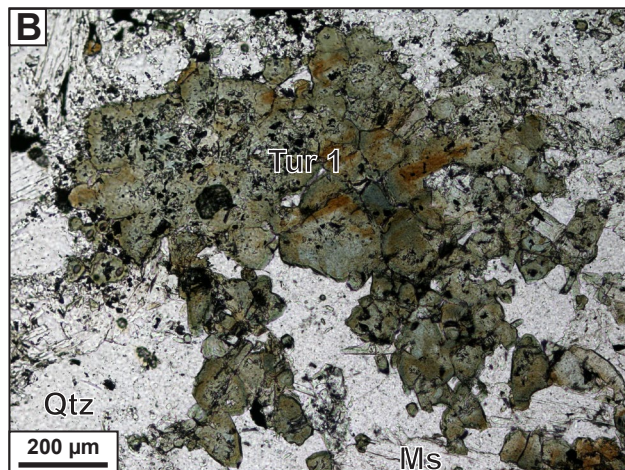
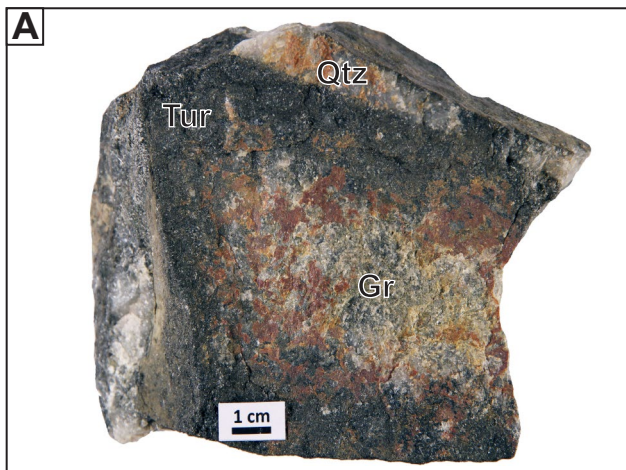
- Paragneiss
- Leptynite-amphibolite complex

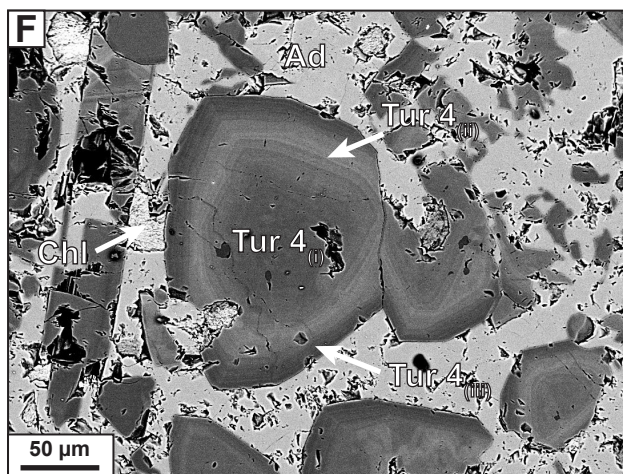
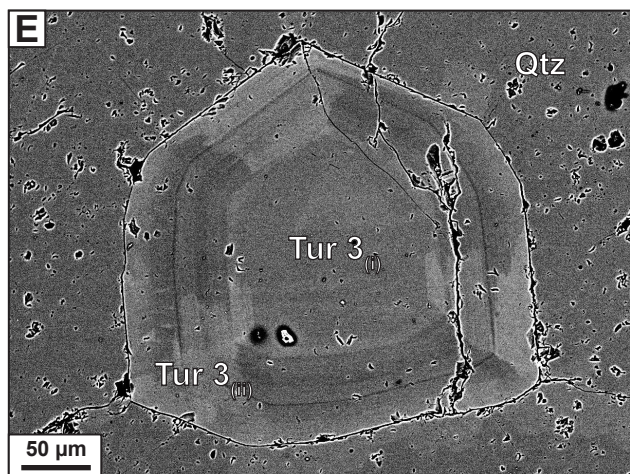
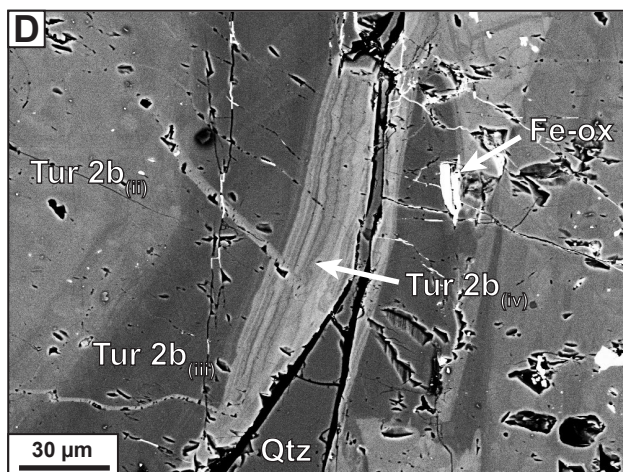
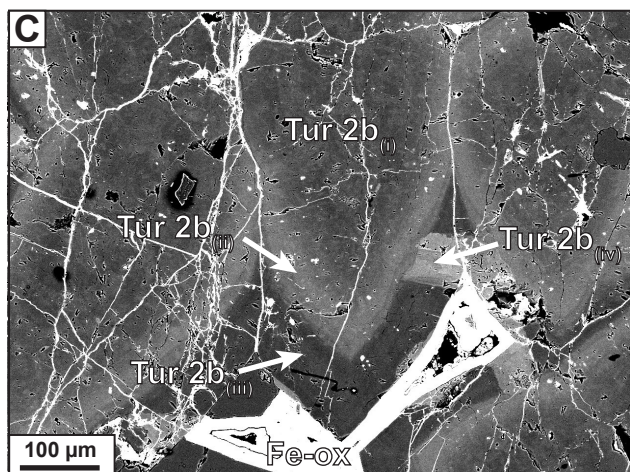
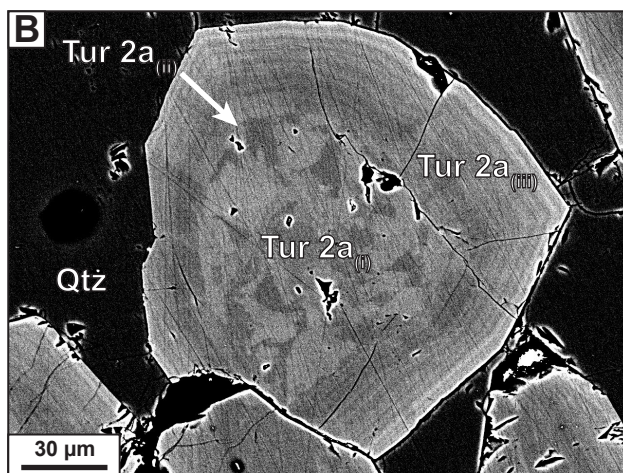
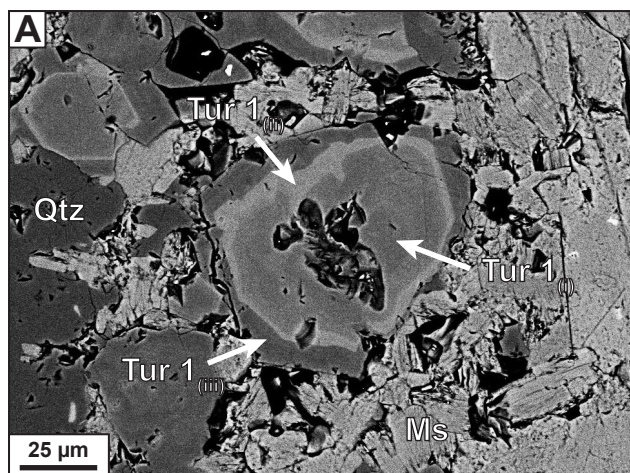
Lower Gneiss Unit (LGU)

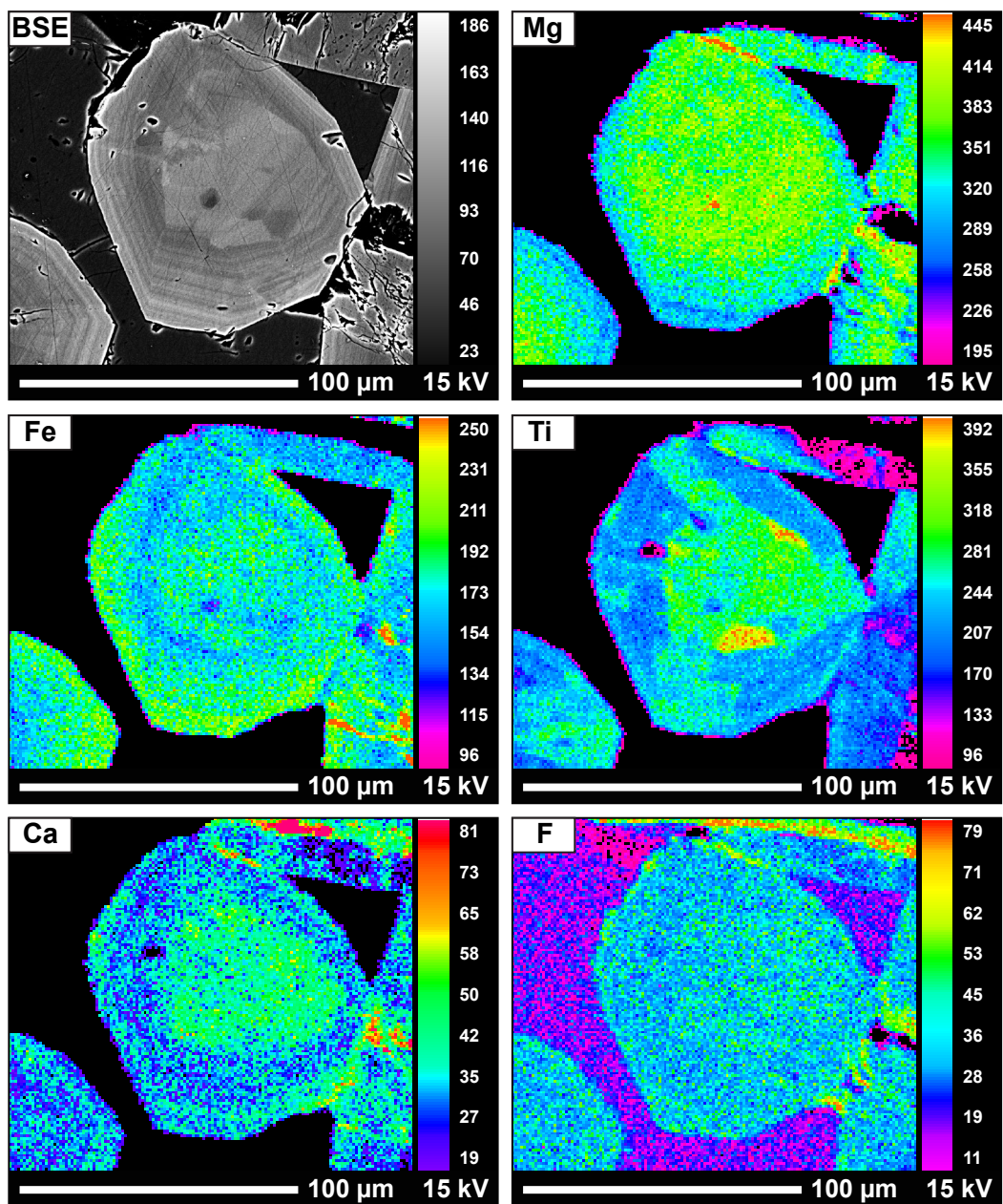
- Leptynite
- Orthogneiss
- Migmatitic paragneiss
- Massive paragneiss
- Massive amphibolite

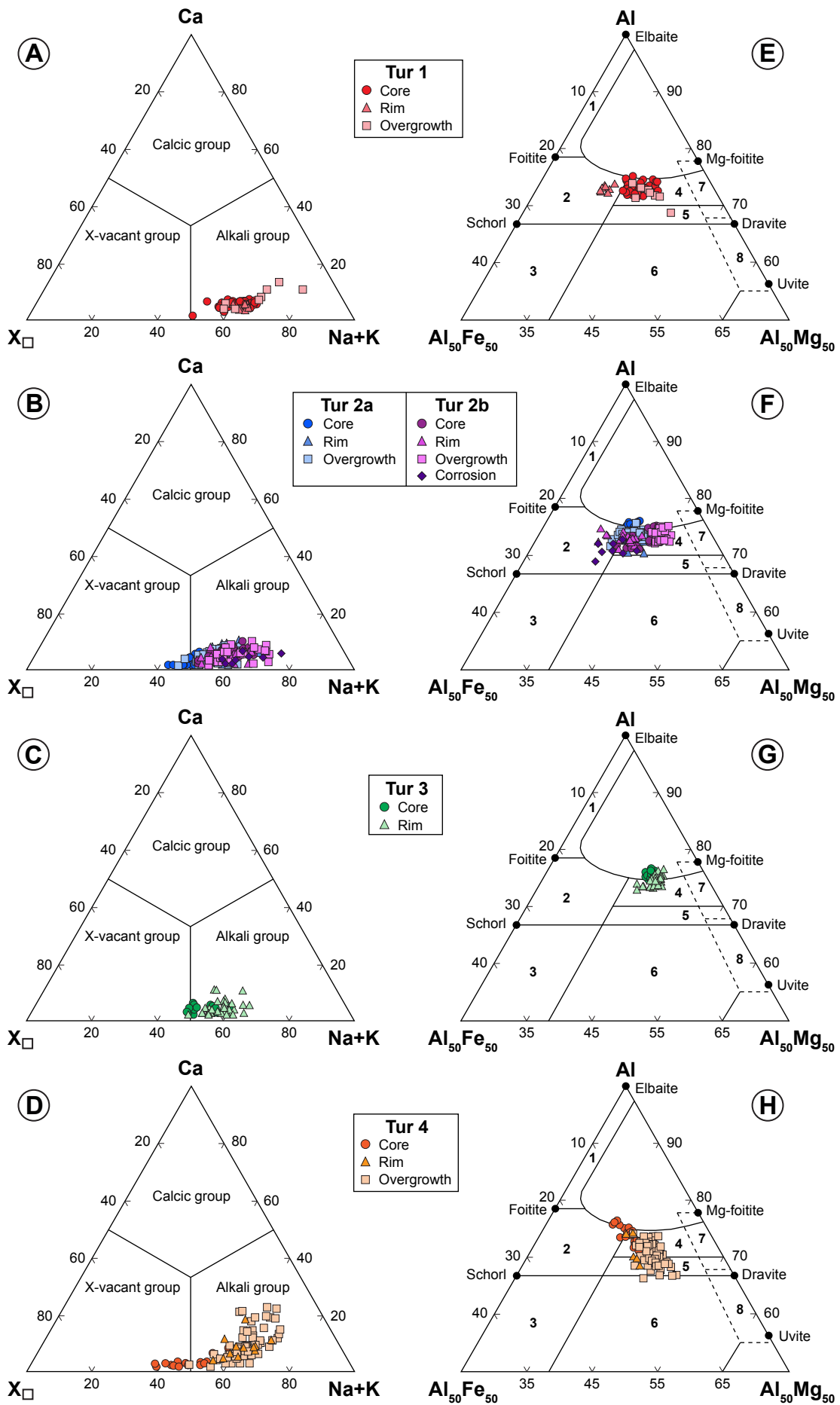
Structures and Mineralization

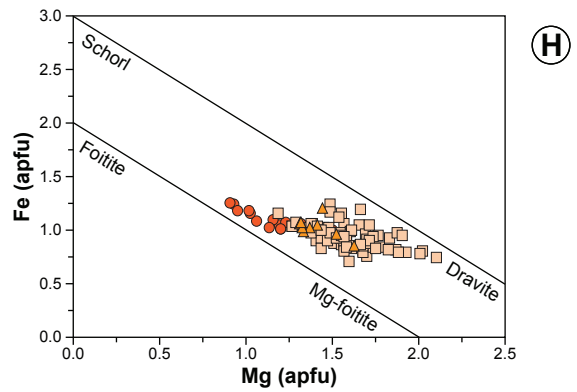
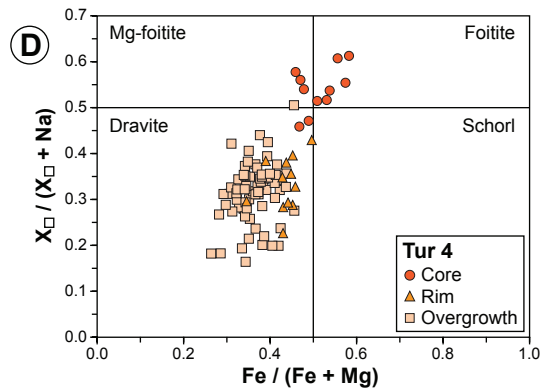
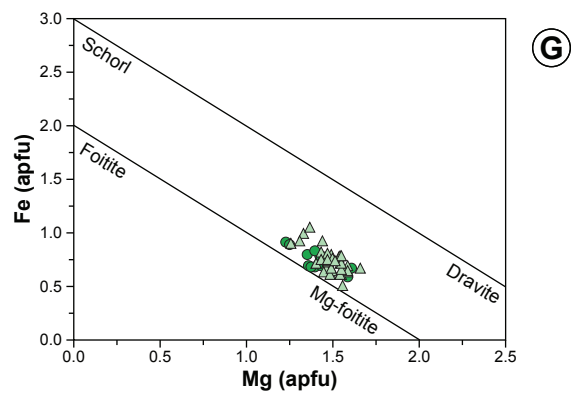
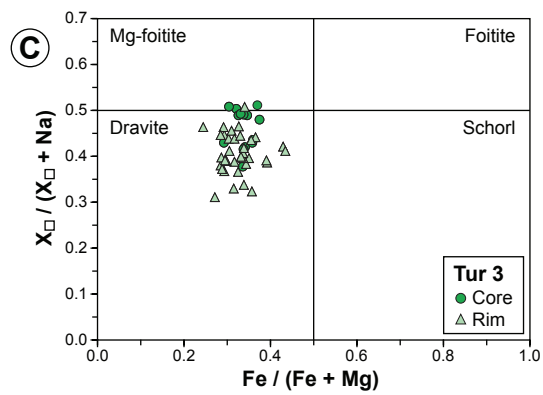
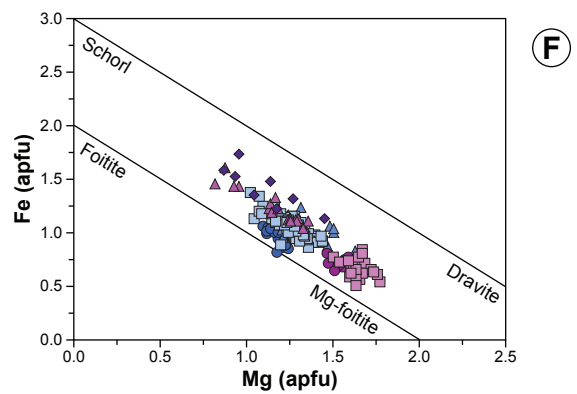
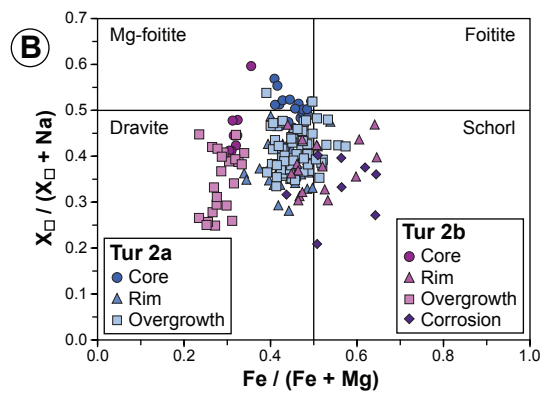
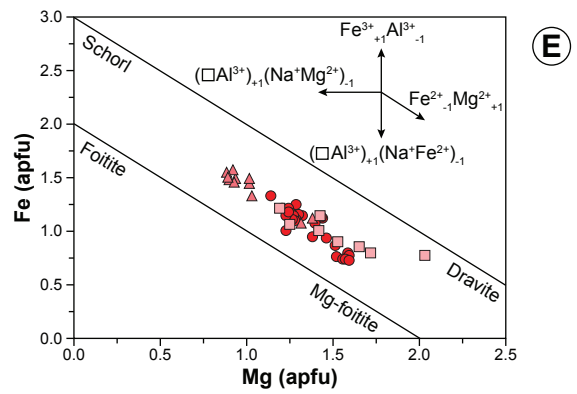
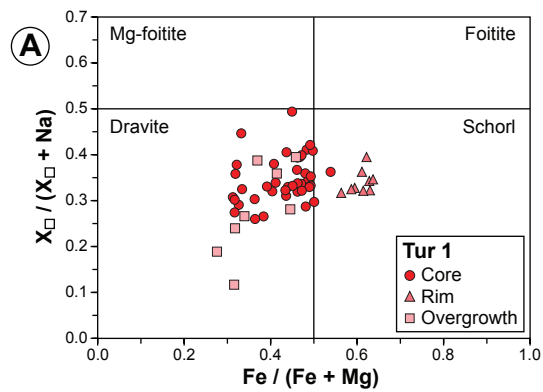
- Breccia pipe
- Lamprophyre dyke
- Microgranite dyke
- Quartz-wolframite veins
- Strike-slip fault
- Wolframite occurrence

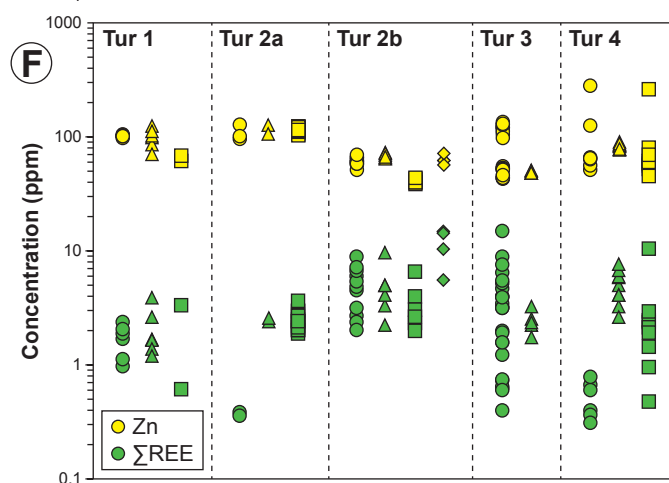
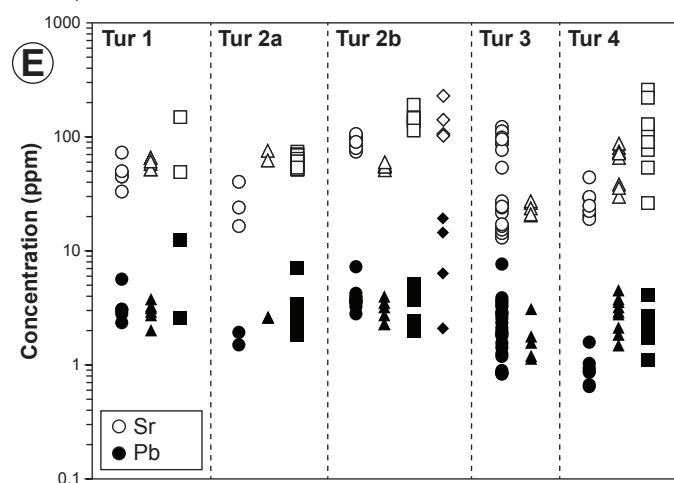
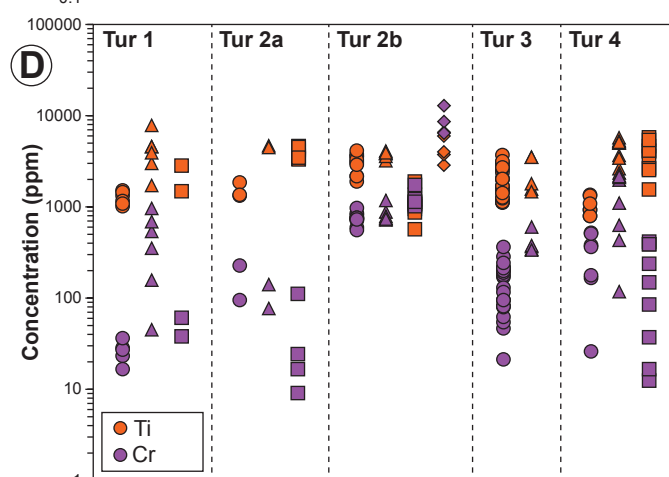
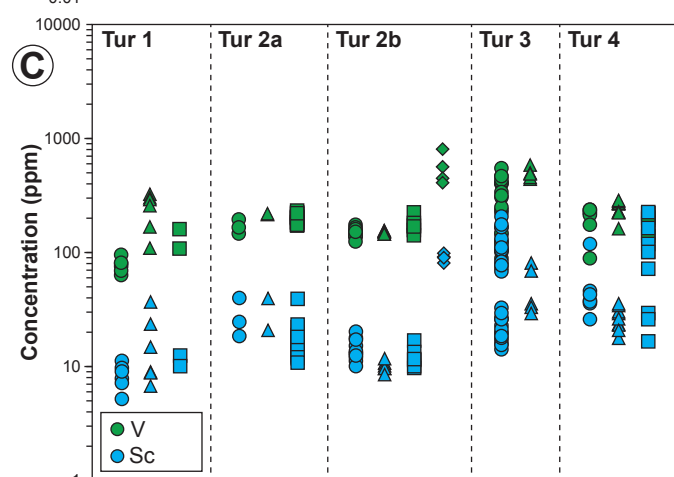
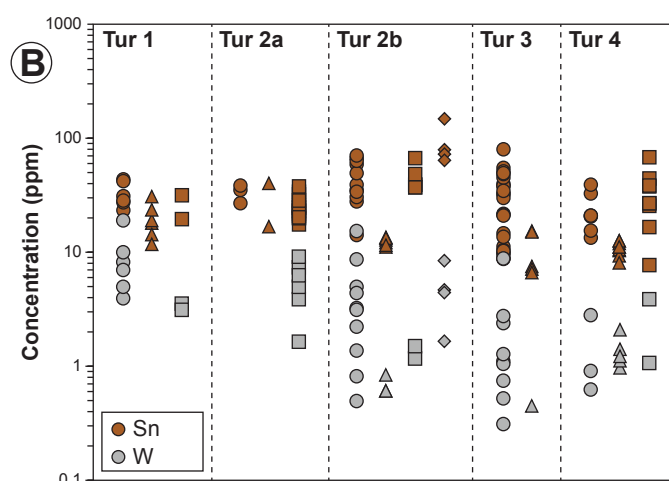
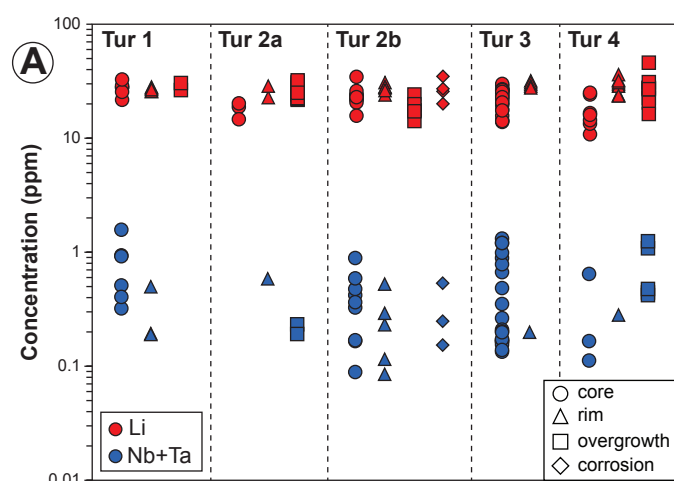


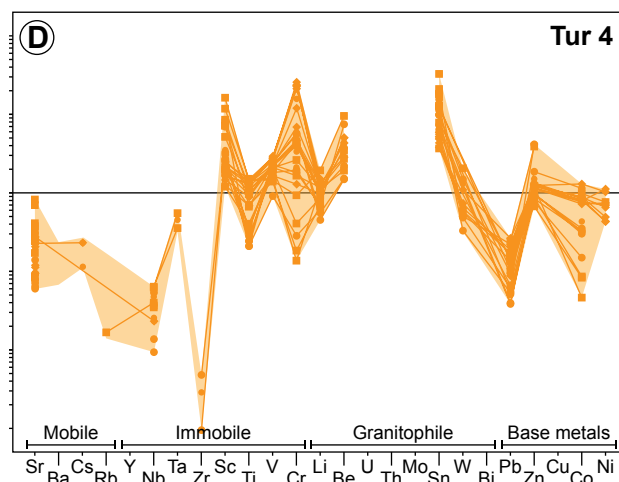
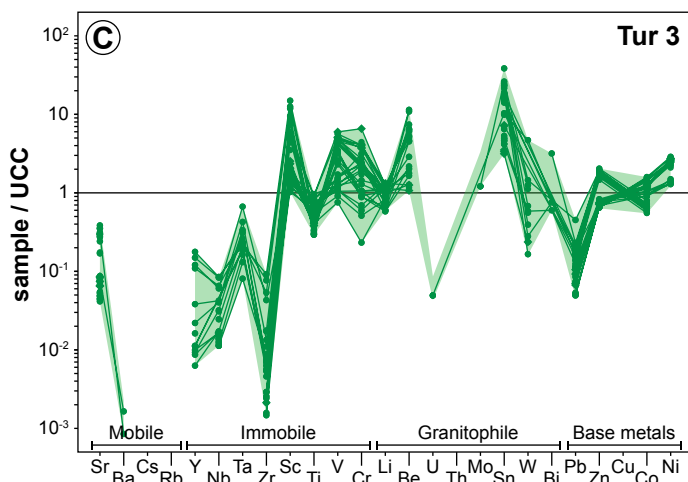
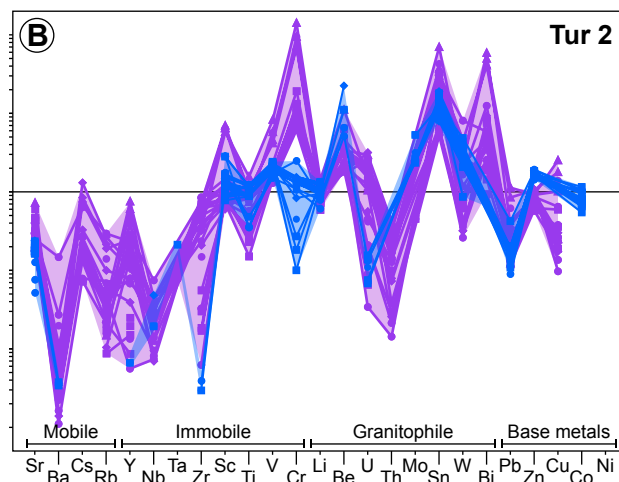
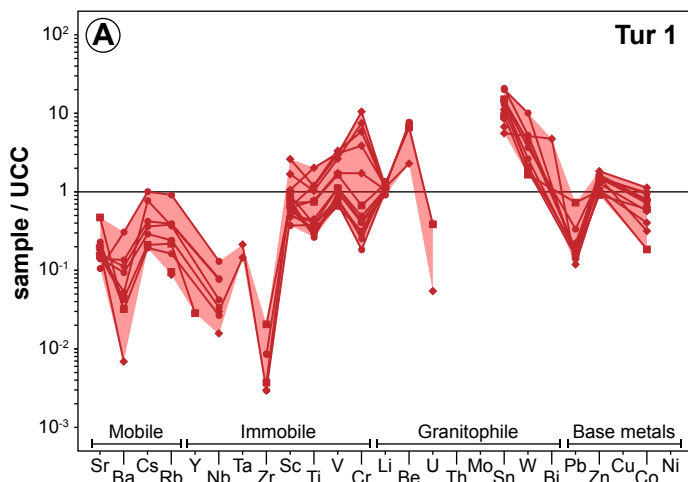


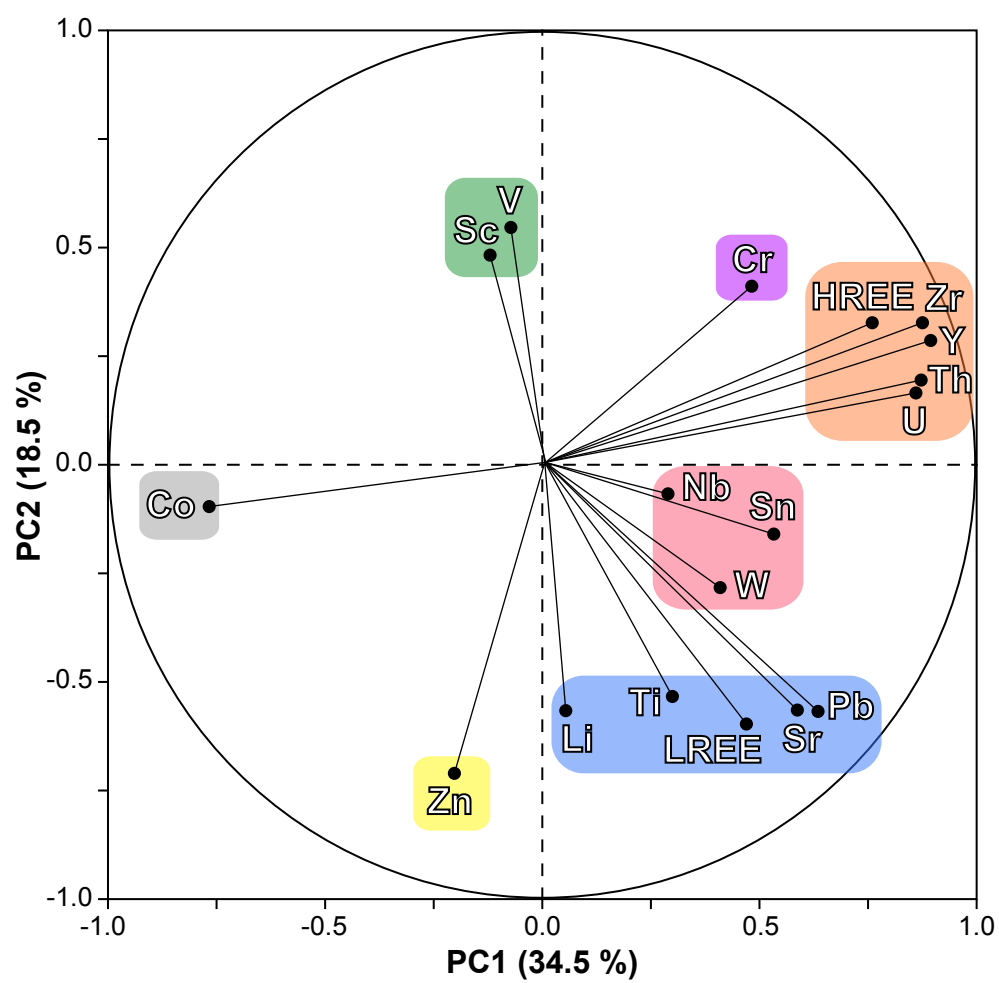


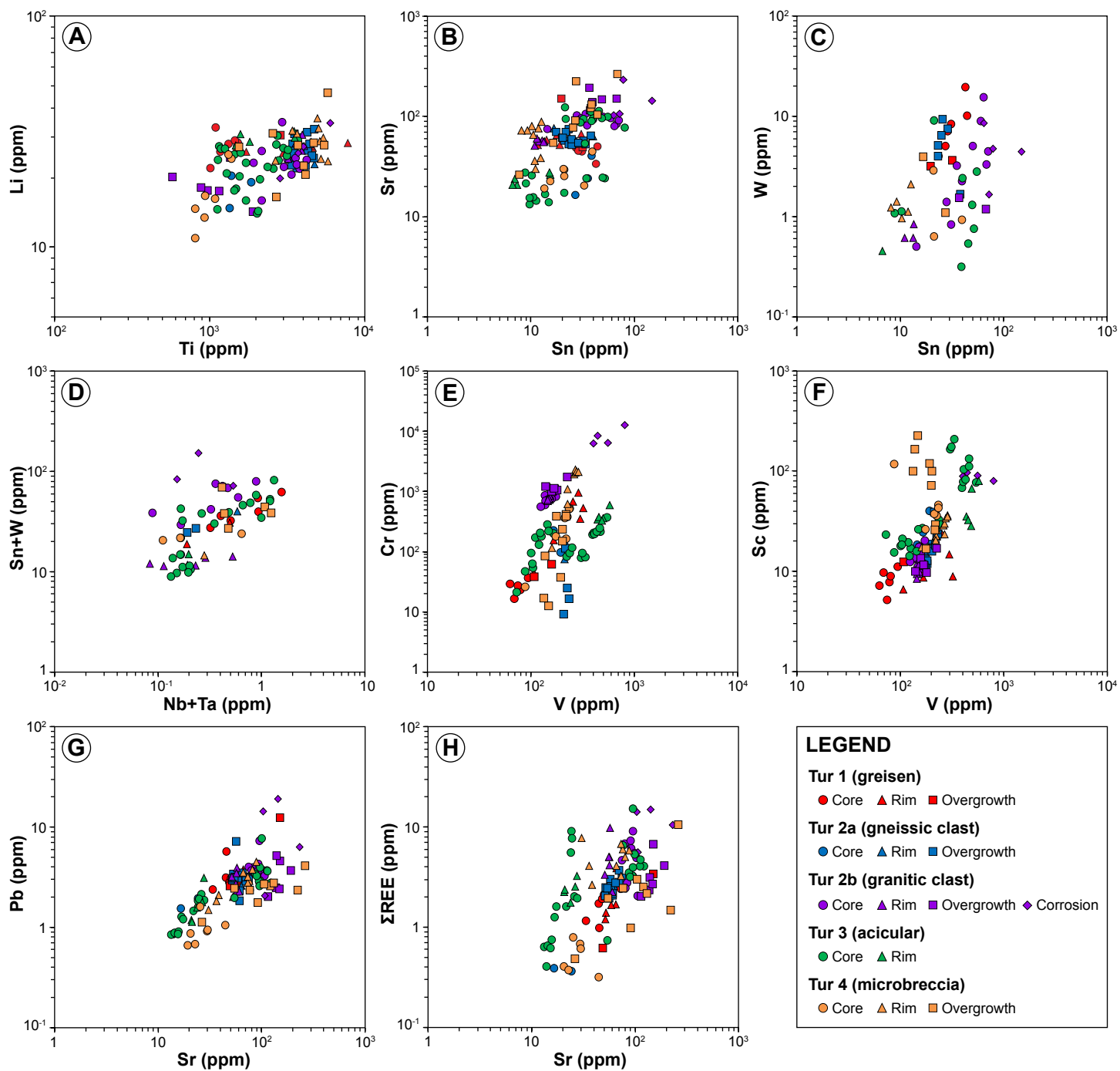


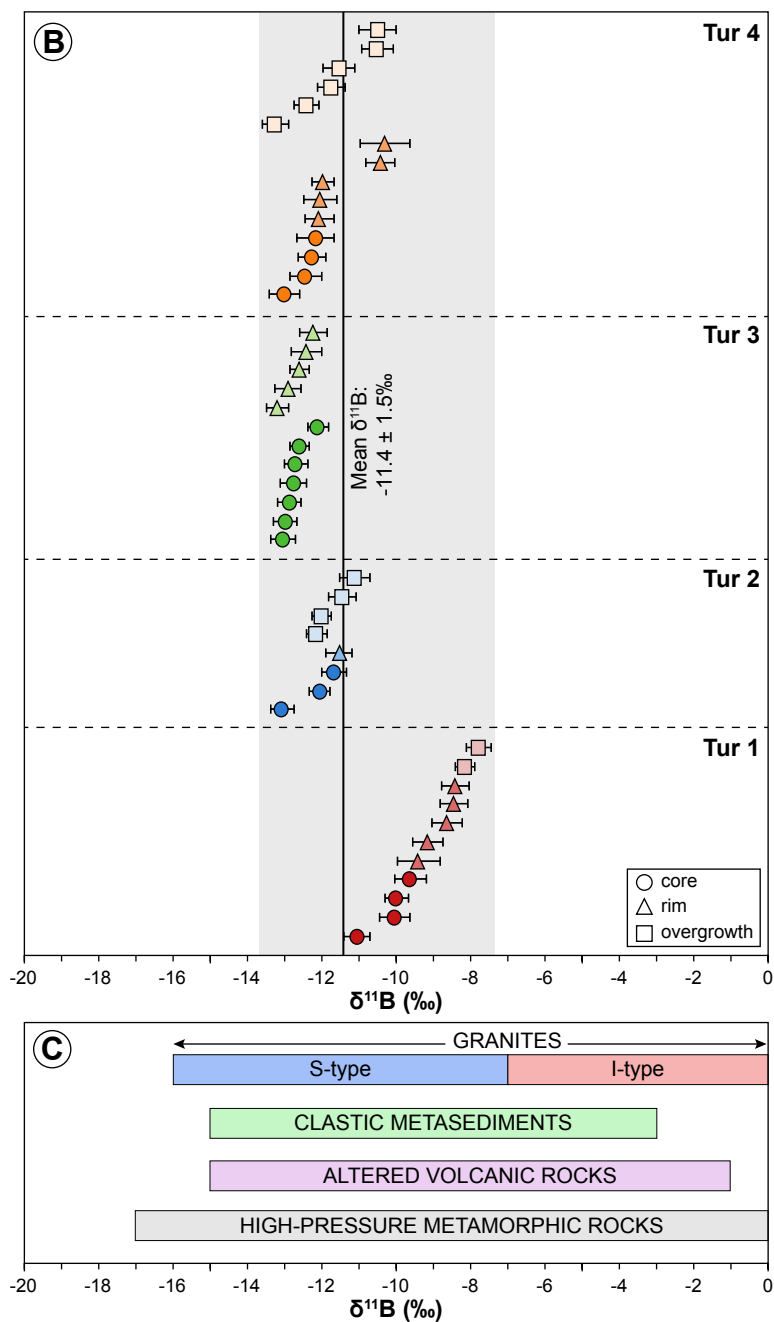
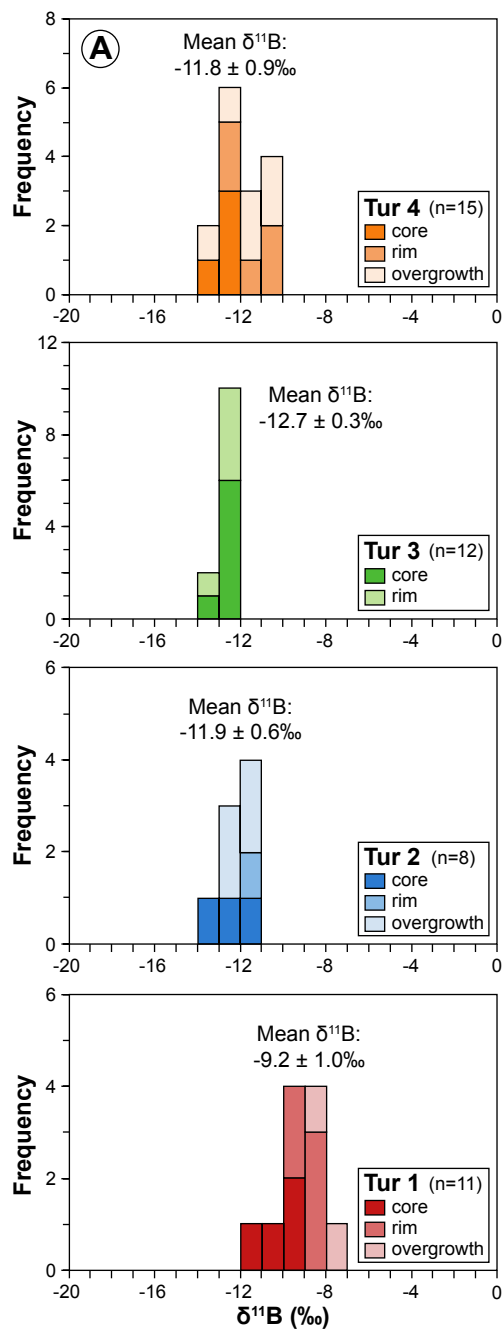


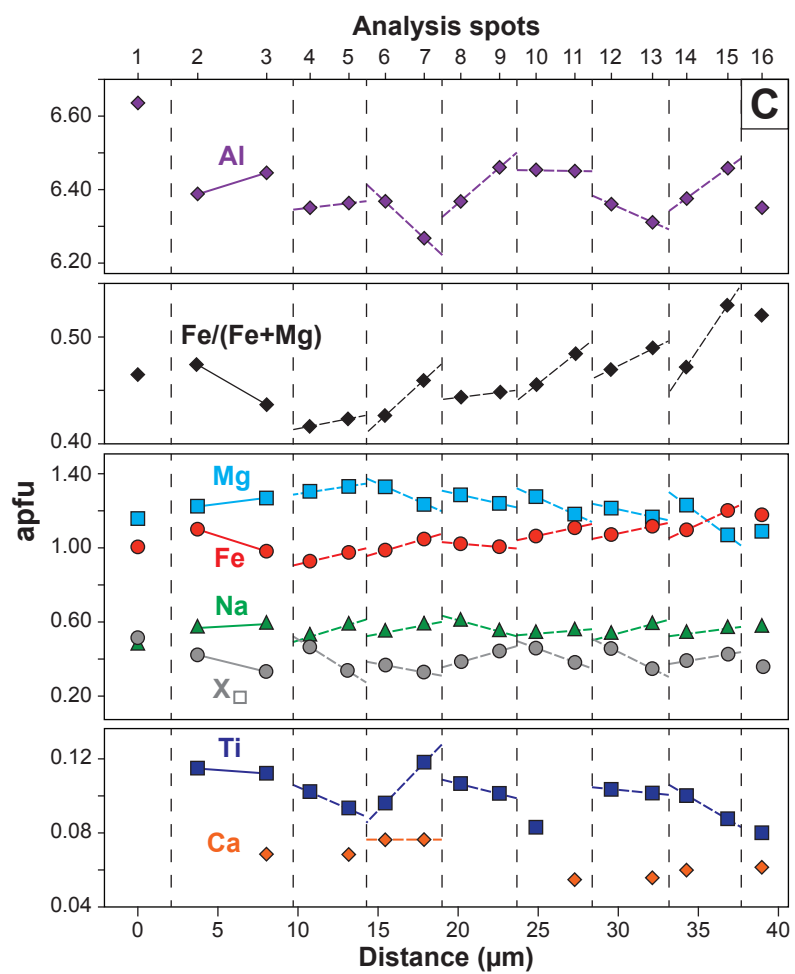
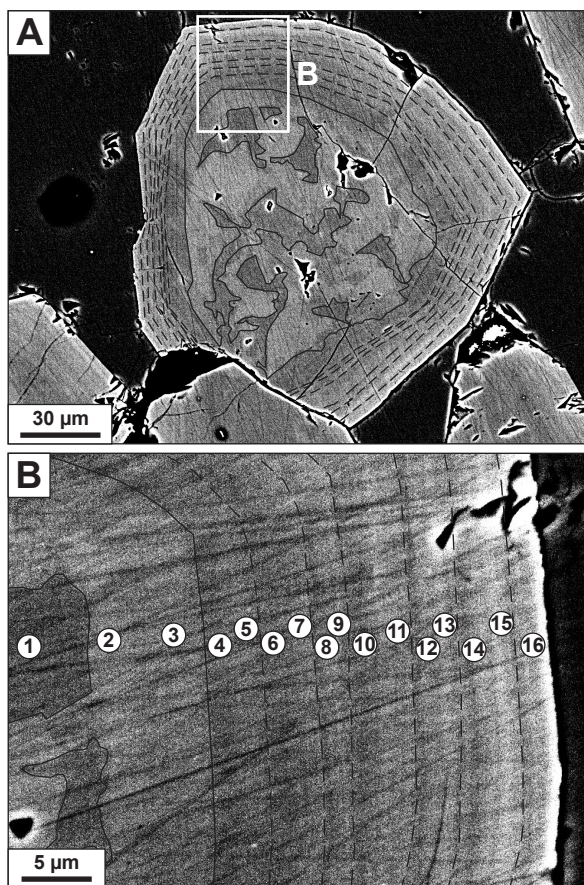


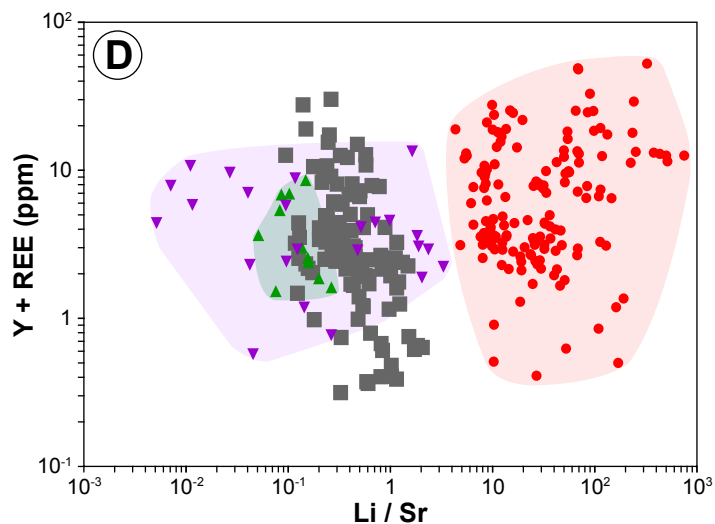
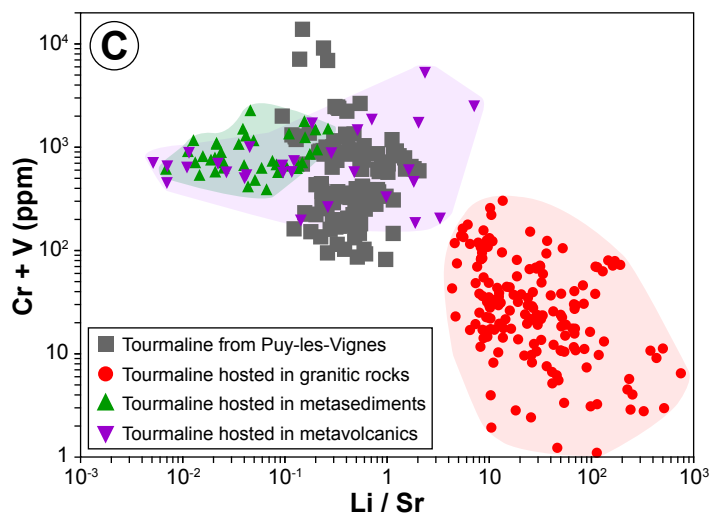
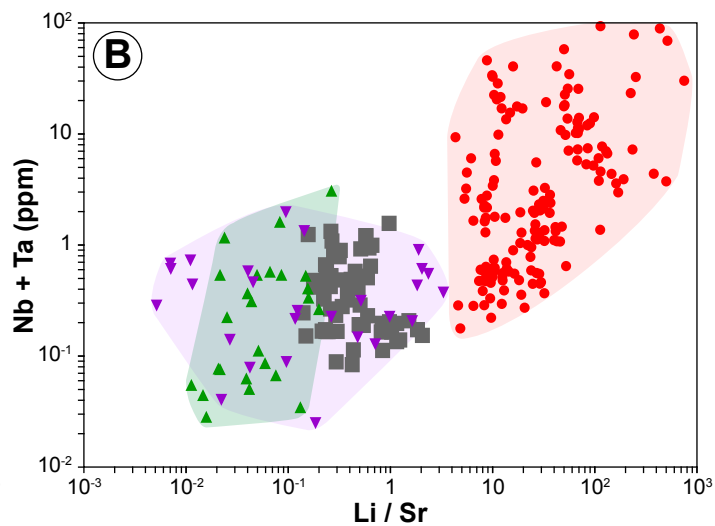
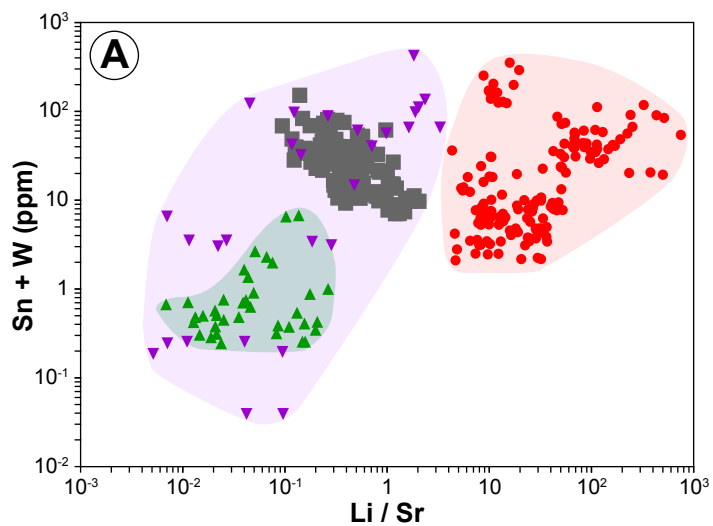












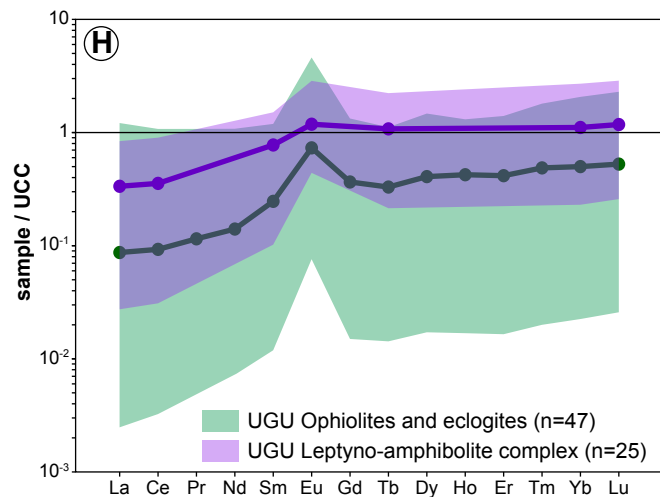
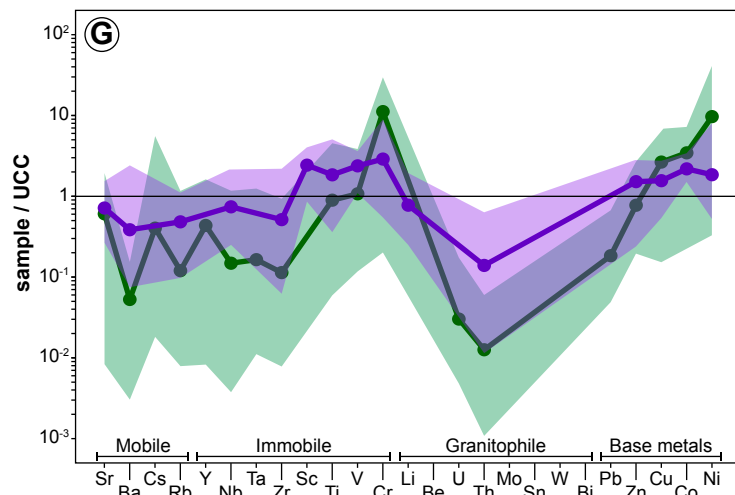
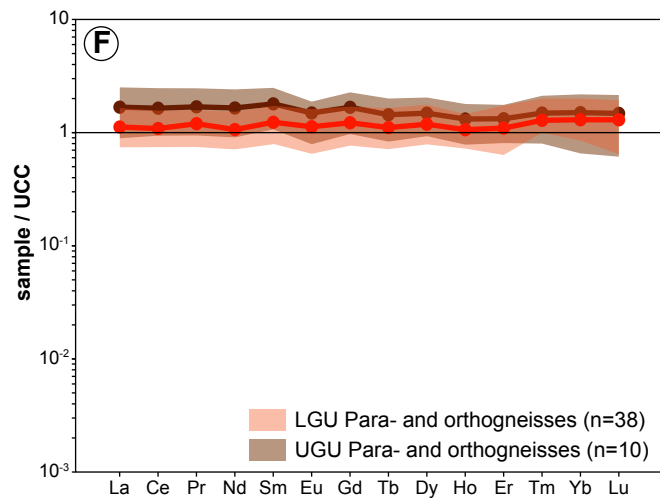
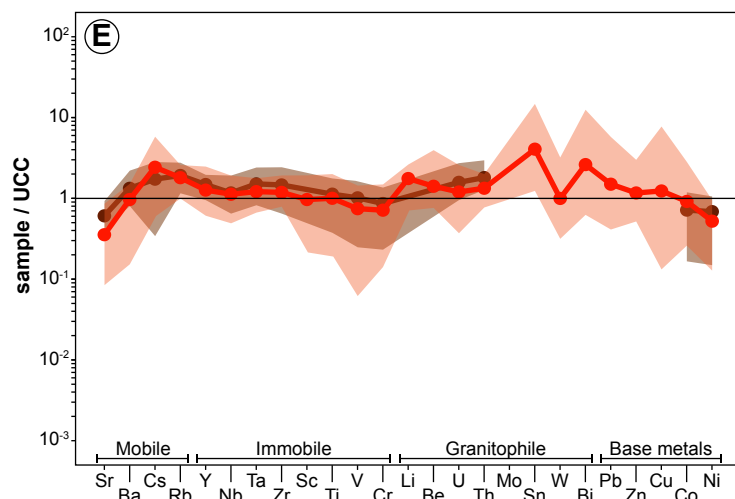
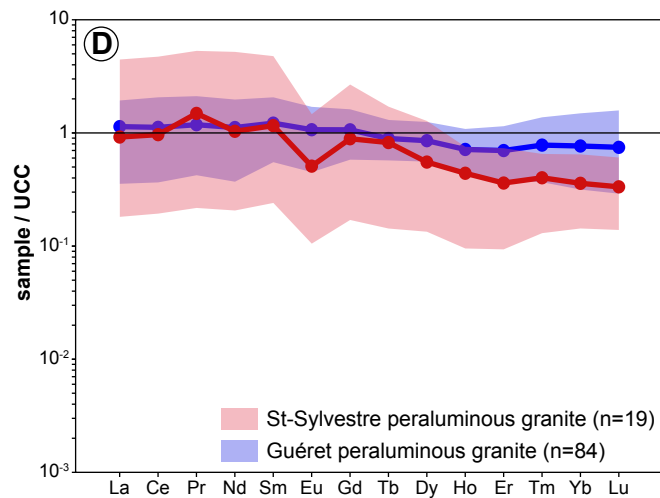
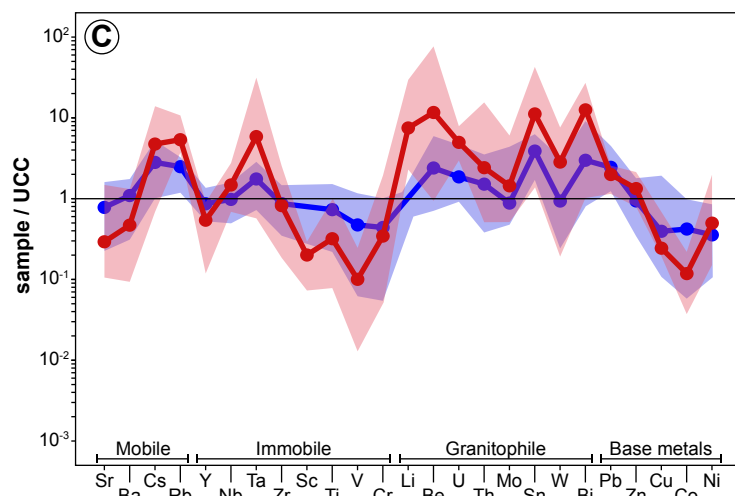
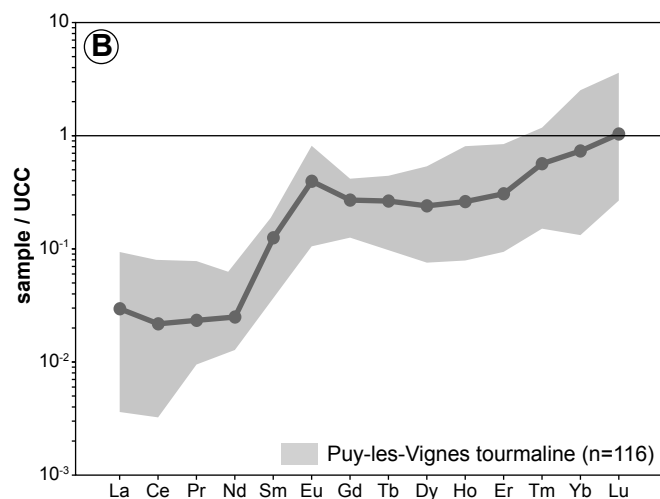
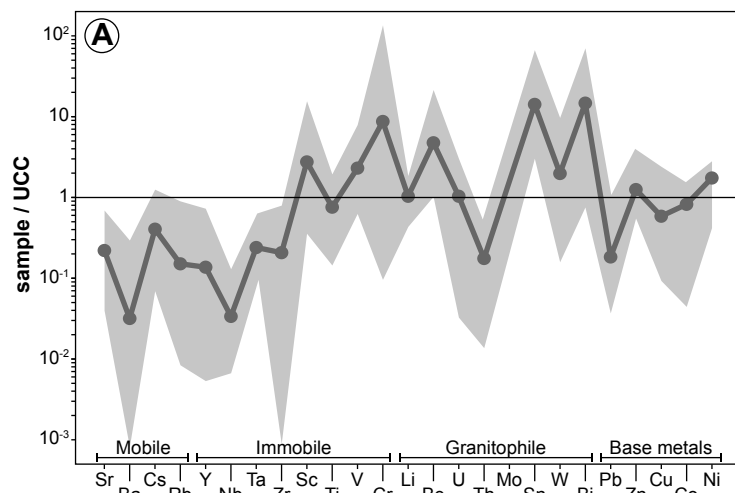


Table 1. Average major element compositions (in wt.% and apfu) of tourmaline from Puy-les-Vignes analyzed by EMPA.

	Greisen tourmaline (Tur 1)						Tourmalinite on gneissic clast (Tur 2a)						Tourmalinite on granitic clast (Tur 2b)			
	Sample PLV-02-08a						Sample PLV-02-01a						Sample PLV-02-04a			
	Core (n=24)		Rim (n=9)		Overgrowth (n=7)		Core (n=22)		Rim (n=53)		Overgrowth (n=68)		Core (n=11)		Rim (n=17)	
	Mean	SD	Mean	SD	Mean	SD	Mean	SD	Mean	SD	Mean	SD	Mean	SD	Mean	SD
SiO ₂ (wt.%)	36.30	0.28	35.96	0.28	36.58	0.55	36.87	0.33	36.32	0.34	36.37	0.42	36.97	0.65	36.21	0.72
TiO ₂	0.79	0.37	0.52	0.25	0.45	0.21	0.10	0.17	0.95	0.32	0.67	0.28	0.29	0.28	0.79	0.32
Al ₂ O ₃	33.79	0.78	33.64	0.52	33.70	0.85	34.26	0.58	32.97	0.74	33.33	0.58	34.85	0.71	33.06	0.79
Cr ₂ O ₃	0.00	0.00	0.00	0.00	0.00	0.00	0.00	0.00	0.00	0.00	0.00	0.00	0.00	0.00	0.00	0.00
FeO	8.07	0.95	10.77	0.49	7.31	1.12	7.18	0.57	7.49	0.65	7.72	0.74	5.35	0.31	9.00	1.12
MgO	5.46	0.49	3.87	0.24	6.21	1.19	4.83	0.20	5.37	0.44	5.16	0.40	6.45	0.19	4.74	0.69
CaO	0.30	0.06	0.27	0.05	0.41	0.18	0.02	0.05	0.29	0.20	0.21	0.18	0.22	0.16	0.24	0.17
MnO	0.00	0.00	0.01	0.04	0.00	0.00	0.00	0.00	0.00	0.00	0.00	0.00	0.00	0.00	0.00	0.00
Na ₂ O	1.93	0.14	1.97	0.07	1.99	0.18	1.57	0.09	1.83	0.11	1.78	0.12	1.72	0.18	1.86	0.17
K ₂ O	0.00	0.00	0.01	0.03	0.01	0.03	0.00	0.00	0.00	0.00	0.00	0.02	0.00	0.00	0.00	0.00
H ₂ O calc	3.68	0.04	3.63	0.06	3.63	0.12	3.67	0.03	3.66	0.03	3.66	0.03	3.73	0.03	3.65	0.02
B ₂ O ₃ calc	10.71	0.07	10.61	0.07	10.75	0.12	10.64	0.10	10.60	0.08	10.60	0.10	10.82	0.09	10.59	0.07
Li ₂ O calc	0.21	0.05	0.19	0.05	0.19	0.06	0.38	0.12	0.33	0.09	0.30	0.10	0.27	0.12	0.27	0.10
Total	101.3	0.5	101.5	0.6	101.4	0.7	99.5	1.1	99.8	0.8	99.8	1.1	100.7	0.7	100.4	0.5
Structural formula (apfu)																
T-site																
Si	5.89	0.03	5.89	0.02	5.91	0.04	6.02	0.06	5.96	0.06	5.97	0.07	5.94	0.09	5.94	0.09
Al	0.11	0.03	0.11	0.02	0.09	0.04	0.01	0.03	0.05	0.06	0.05	0.06	0.07	0.08	0.07	0.08
B-site																
B	3.00	0.00	3.00	0.00	3.00	0.00	3.00	0.00	3.00	0.00	3.00	0.00	3.00	0.00	3.00	0.00
Z-site																
Al	6.00	0.00	6.00	0.00	6.00	0.00	6.00	0.00	6.00	0.00	6.00	0.00	6.00	0.00	6.00	0.00
Mg	0.00	0.00	0.00	0.00	0.00	0.00	0.00	0.00	0.00	0.00	0.00	0.00	0.00	0.00	0.00	0.00
Cr	0.00	0.00	0.00	0.00	0.00	0.00	0.00	0.00	0.00	0.00	0.00	0.00	0.00	0.00	0.00	0.00
Fe ³⁺	0.00	0.00	0.00	0.00	0.00	0.00	0.00	0.00	0.00	0.00	0.00	0.00	0.00	0.00	0.00	0.00
Y-site																
Al	0.35	0.12	0.39	0.05	0.33	0.14	0.58	0.05	0.32	0.09	0.40	0.06	0.53	0.08	0.33	0.11
Ti	0.10	0.05	0.06	0.03	0.06	0.03	0.01	0.02	0.12	0.04	0.08	0.03	0.04	0.03	0.10	0.04
Cr	0.00	0.00	0.00	0.00	0.00	0.00	0.00	0.00	0.00	0.00	0.00	0.00	0.00	0.00	0.00	0.00
Fe ³⁺	0.00	0.00	0.00	0.00	0.00	0.00	0.00	0.00	0.00	0.00	0.00	0.00	0.00	0.00	0.00	0.00
Mg	1.32	0.11	0.95	0.06	1.50	0.28	1.18	0.05	1.31	0.10	1.26	0.10	1.55	0.05	1.16	0.17
Mn	0.00	0.00	0.00	0.01	0.00	0.00	0.00	0.00	0.00	0.00	0.00	0.00	0.00	0.00	0.00	0.00
Fe ²⁺	1.10	0.13	1.48	0.07	0.99	0.16	0.98	0.08	1.03	0.09	1.06	0.10	0.72	0.05	1.24	0.16
Li	0.14	0.03	0.13	0.03	0.13	0.04	0.25	0.08	0.22	0.06	0.20	0.07	0.17	0.08	0.18	0.07
X-site																
Ca	0.05	0.01	0.05	0.01	0.07	0.03	0.00	0.01	0.05	0.04	0.04	0.03	0.04	0.03	0.04	0.03
Na	0.61	0.05	0.63	0.02	0.62	0.06	0.50	0.03	0.58	0.03	0.57	0.04	0.54	0.06	0.59	0.05
K	0.00	0.00	0.00	0.01	0.00	0.01	0.00	0.00	0.00	0.00	0.00	0.00	0.00	0.00	0.00	0.00
□	0.34	0.05	0.32	0.02	0.30	0.08	0.50	0.03	0.37	0.05	0.40	0.05	0.43	0.06	0.37	0.06
OH	3.99	0.03	3.97	0.05	3.92	0.11	4.00	0.00	4.00	0.00	4.00	0.00	4.00	0.00	4.00	0.00
Xvac/(Xvac+Na)	0.36	0.05	0.34	0.03	0.33	0.08	0.50	0.03	0.39	0.04	0.41	0.05	0.44	0.06	0.38	0.06
Fe/(Fe+Mg)	0.45	0.05	0.61	0.02	0.40	0.08	0.45	0.03	0.44	0.04	0.46	0.04	0.32	0.02	0.52	0.07

Structural formula based on 31 anions (O, OH, F). B₂O₃, H₂O and Li₂O calculated by stoichiometry assuming B=3 apfu, OH+F=4 apfu and Li=15-total(T+Z+Y) and normalizing to 31 anions.

Table 1. (continued)

	Tourmalinite on granitic clast (Tur 2b)				Acicular tourmaline (Tur 3)				Sample PLV-02-15				Brecia tourmaline (Tur 4)					
	Sample PLV-02-04a				Sample PLV-02-01c				Sample PLV-02-15				Sample PLV-02-13a/b					
	Overgrowth (n=23)		Corrosion (n=8)		Core (n=6)		Rim (n=6)		Core (n=8)		Rim (n=31)		Core (n=11)		Rim (n=12)		Overgrowth (n=69)	
	Mean	SD	Mean	SD	Mean	SD	Mean	SD	Mean	SD	Mean	SD	Mean	SD	Mean	SD	Mean	SD
SiO ₂ (wt.%)	37.21	0.71	35.90	0.68	36.95	0.26	36.41	0.34	37.18	0.38	36.97	0.28	36.50	0.58	36.33	0.60	36.68	0.61
TiO ₂	0.22	0.31	0.99	0.83	0.24	0.05	0.60	0.32	0.06	0.18	0.30	0.37	0.13	0.15	0.96	0.26	0.80	0.47
Al ₂ O ₃	34.00	0.65	32.38	1.93	35.61	0.25	34.81	0.78	34.92	0.43	34.23	0.61	34.28	0.75	32.10	1.44	32.22	1.34
Cr ₂ O ₃	0.02	0.10	0.46	0.85	0.00	0.00	0.00	0.00	0.00	0.00	0.00	0.00	0.00	0.00	0.00	0.00	0.00	0.00
FeO	5.02	0.66	8.96	2.68	6.14	0.43	6.89	0.56	5.09	0.32	5.07	0.51	8.22	0.62	7.73	0.67	6.79	0.74
MgO	6.93	0.28	4.93	1.32	5.64	0.41	5.62	0.28	5.97	0.30	6.26	0.23	4.37	0.47	5.67	0.50	6.65	0.69
CaO	0.28	0.21	0.19	0.13	0.24	0.04	0.40	0.17	0.00	0.00	0.06	0.13	0.07	0.07	0.43	0.29	0.53	0.31
MnO	0.00	0.00	0.00	0.00	0.00	0.00	0.00	0.00	0.00	0.00	0.00	0.00	0.00	0.00	0.00	0.00	0.00	0.04
Na ₂ O	2.00	0.19	1.93	0.11	1.58	0.18	1.62	0.14	1.69	0.14	1.86	0.12	1.42	0.16	1.91	0.13	1.96	0.12
K ₂ O	0.00	0.00	0.00	0.00	0.02	0.04	0.00	0.00	0.00	0.00	0.00	0.00	0.00	0.02	0.01	0.02	0.01	0.02
H ₂ O calc	3.73	0.03	3.60	0.03	3.75	0.03	3.72	0.02	3.71	0.02	3.70	0.02	3.65	0.02	3.64	0.06	3.68	0.04
B ₂ O ₃ calc	10.82	0.09	10.43	0.08	10.86	0.07	10.78	0.05	10.76	0.07	10.72	0.06	10.59	0.06	10.55	0.17	10.66	0.12
Li ₂ O calc	0.37	0.16	0.21	0.06	0.27	0.02	0.24	0.04	0.35	0.11	0.36	0.07	0.29	0.13	0.34	0.13	0.31	0.13
Total	100.6	0.6	100.0	0.7	101.3	0.6	101.1	0.3	99.7	0.5	99.5	0.6	99.5	0.7	99.7	1.3	100.3	1.0
Structural formula (apfu)																		
T-site																		
Si	5.99	0.08	5.94	0.06	5.91	0.03	5.87	0.03	6.00	0.03	6.00	0.03	5.99	0.09	5.98	0.06	5.98	0.07
Al	0.04	0.06	0.06	0.06	0.09	0.03	0.13	0.03	0.01	0.02	0.01	0.02	0.04	0.05	0.03	0.05	0.04	0.06
B-site																		
B	3.00	0.00	3.00	0.00	3.00	0.00	3.00	0.00	3.00	0.00	3.00	0.00	3.00	0.00	3.00	0.00	3.00	0.00
Z-site																		
Al	6.00	0.00	5.97	0.07	6.00	0.00	6.00	0.00	6.00	0.00	6.00	0.00	6.00	0.00	5.99	0.04	5.96	0.08
Mg	0.00	0.00	0.03	0.07	0.00	0.00	0.00	0.00	0.00	0.00	0.00	0.00	0.00	0.00	0.01	0.04	0.04	0.08
Cr	0.00	0.00	0.00	0.00	0.00	0.00	0.00	0.00	0.00	0.00	0.00	0.00	0.00	0.00	0.00	0.00	0.00	0.00
Fe ³⁺	0.00	0.00	0.00	0.00	0.00	0.00	0.00	0.00	0.00	0.00	0.00	0.00	0.00	0.00	0.00	0.00	0.00	0.00
Y-site																		
Al	0.42	0.09	0.16	0.13	0.63	0.04	0.49	0.14	0.64	0.07	0.53	0.10	0.59	0.09	0.21	0.15	0.19	0.16
Ti	0.02	0.03	0.14	0.09	0.03	0.01	0.07	0.04	0.01	0.02	0.04	0.05	0.02	0.02	0.12	0.03	0.10	0.06
Cr	0.00	0.01	0.06	0.11	0.00	0.00	0.00	0.00	0.00	0.00	0.00	0.00	0.00	0.00	0.00	0.00	0.00	0.00
Fe ³⁺	0.00	0.00	0.00	0.00	0.00	0.00	0.00	0.00	0.00	0.00	0.00	0.00	0.00	0.00	0.00	0.00	0.00	0.00
Mg	1.65	0.06	1.08	0.23	1.35	0.09	1.35	0.07	1.44	0.07	1.51	0.06	1.07	0.12	1.38	0.12	1.58	0.14
Mn	0.00	0.00	0.00	0.00	0.00	0.00	0.00	0.00	0.00	0.00	0.00	0.00	0.00	0.00	0.00	0.00	0.00	0.00
Fe ²⁺	0.67	0.09	1.42	0.20	0.82	0.06	0.93	0.08	0.69	0.04	0.69	0.07	1.13	0.08	1.07	0.10	0.93	0.10
Li	0.24	0.10	0.14	0.04	0.18	0.01	0.15	0.02	0.23	0.07	0.23	0.05	0.19	0.09	0.23	0.08	0.20	0.08
X-site																		
Ca	0.05	0.03	0.04	0.02	0.04	0.01	0.07	0.03	0.00	0.00	0.01	0.02	0.01	0.01	0.08	0.05	0.09	0.06
Na	0.62	0.06	0.64	0.05	0.49	0.05	0.51	0.05	0.53	0.05	0.58	0.04	0.45	0.05	0.61	0.04	0.62	0.04
K	0.00	0.00	0.00	0.00	0.00	0.01	0.00	0.00	0.00	0.00	0.00	0.00	0.00	0.00	0.00	0.00	0.00	0.00
□	0.33	0.07	0.32	0.07	0.46	0.05	0.42	0.07	0.47	0.05	0.41	0.05	0.53	0.05	0.31	0.07	0.29	0.07
OH	4.00	0.00	4.00	0.00	4.00	0.00	4.00	0.00	4.00	0.00	4.00	0.00	4.00	0.00	4.00	0.00	4.00	0.00
Xvac/(Xvac+Na)																		
	0.35	0.07	0.33	0.07	0.49	0.05	0.45	0.06	0.47	0.05	0.41	0.04	0.54	0.05	0.33	0.06	0.31	0.07
Fe/(Fe+Mg)	0.29	0.03	0.56	0.07	0.38	0.03	0.41	0.03	0.32	0.02	0.31	0.03	0.51	0.04	0.43	0.04	0.37	0.04

Table 2. Average trace element concentrations (in ppm) in tourmaline from Puy-les-Vignes determined by LA-ICP-MS.

	LD	Greisen tourmaline (Tur 1)												Tourmalinite on greissic clast (Tur 2a)												Tourmalinite on granitic clast (Tur 2b)											
		Sample PLV-02-08a												Sample PLV-02-01a												Sample PLV-02-04a											
		Core (n=6)						Rim (n=6)			Overgrowth (n=2)			Core (n=3)						Rim (n=2)			Overgrowth (n=15)						Core (n=11)						Rim (n=6)		
		Mean	SD	Min	Max	Mean	SD	Min	Max	Mean	SD	Min	Max	Mean	SD	Min	Max	Mean	SD	Min	Max	Mean	SD	Min	Max	Mean	SD	Min	Max	Mean	SD	Min	Max				
Li	4.2	28	3.6	22	33	27	1.0	25	28	18	2.8	27	30	18	2.9	15	20	26	4.1	23	29	26	3.4	22	32	24	4.5	16	35	27	2.2	24	31				
Be	4.8	16	-	16	16	4.8	-	4.8	4.8	14	-	14	14	12	2.1	11	14	47	-	47	47	23	-	23	23	7.0	2.6	3.8	12	<LD	<LD	<LD	<LD				
Sc	1.9	8.4	2.1	5.2	11	17	12	6.7	37	21.3	1.7	10	12	28	11	19	40	30	13	21	40	18	7.0	11	39	14	3.2	10	20	10	1.1	8.5	12				
Ti	6.8	1270	205	1051	1530	4260	1040	1720	7780	2190	965	1500	2870	1530	280	1350	1860	4620	160	4500	4730	3950	515	3380	4720	3100	740	1930	4220	3770	320	3200	4070				
V	1.2	78	11	64	96	240	84	110	325	135	37	110	160	170	24	150	200	215	3.2	215	220	200	20	170	235	150	14	125	175	150	4.0	145	155				
Cr	9.7	27	7.5	17	37	460	345	45	970	50	16	39	62	165	93	98	230	110	46	77	140	41	49	92	114	760	115	560	990	845	180	715	1190				
Co	0.46	14	1.8	12	17	12	5.2	5.5	20	6.8	5.1	3.2	10	18	0.87	17	18	17	0.77	17	18	14	2.4	9.5	20	<LD	<LD	<LD	<LD	<LD	<LD	<LD	<LD				
Ni	16.4	<LD	<LD	<LD	<LD	<LD	<LD	<LD	<LD	<LD	<LD	<LD	<LD	<LD	<LD	<LD	<LD	<LD	<LD	<LD	<LD	<LD	<LD	<LD	<LD	<LD	<LD	<LD	<LD	<LD	<LD	<LD	<LD				
Cu	3.4	<LD	<LD	<LD	<LD	<LD	<LD	<LD	<LD	<LD	<LD	<LD	<LD	<LD	<LD	<LD	<LD	<LD	<LD	<LD	<LD	<LD	<LD	<LD	<LD	<LD	<LD	<LD	<LD	<LD	<LD	<LD	<LD				
Zn	4.2	103	2.5	99	106	98	18	70	123	65	5.5	61	69	109	18	96	129	116	14	106	126	114	6.1	104	124	61	5.0	52	70	68	3.4	64	72				
Rb	1.1	35	22	14	77	7.4	-	7.4	7.4	13	7.3	8.0	18	<LD	<LD	<LD	<LD	<LD	<LD	<LD	<LD	<LD	<LD	<LD	<LD	<LD	5.8	7.7	1.8	25	12	8.3	0.88	22			
Sr	0.19	50	13	34	74	60	6.3	52	67	100	72	49	151	27	12	17	41	70	9.3	63	76	60	7.2	52	75	92	10	75	107	56	2.9	51	60				
Y	0.20	<LD	<LD	<LD	<LD	<LD	<LD	<LD	<LD	0.60	-	0.60	0.6	<LD	<LD	<LD	<LD	<LD	<LD	<LD	<LD	<LD	0.14	-	0.14	0.14	3.4	2.5	0.12	8.3	2.6	1.5	0.82	5.1			
Zr	0.40	1.7	-	1.7	1.7	0.57	-	0.6	0.6	2.3	2.3	0.72	4.0	0.75	-	0.75	0.75	<LD	<LD	<LD	<LD	<LD	0.57	-	0.57	0.57	101	58	1.2	165	84	36	40	130			
Nb	0.19	0.78	0.47	0.32	1.6	0.27	0.1	0.2	0.4	<LD	<LD	<LD	<LD	<LD	<LD	<LD	<LD	0.58	-	0.58	0.58	0.23	-	0.23	0.23	0.35	0.25	0.09	0.89	0.25	0.18	0.08	0.52				
Mf	1.2	<LD	<LD	<LD	<LD	<LD	<LD	<LD	<LD	<LD	<LD	<LD	<LD	<LD	<LD	<LD	<LD	<LD	<LD	<LD	<LD	3.5	1.6	2.6	5.8	<LD	<LD	<LD	<LD	<LD	<LD	<LD	<LD	<LD			
Cs	0.83	33	8.4	23	44	19	6.8	12	31	26	8.5	20	32	33	6.0	27	38	28	17	17	40	26	5.7	17	38	45	19	14	71	12	1.0	11	13				
Sn	0.60	2.5	1.5	0.9	4.9	<LD	<LD	<LD	<LD	1.0	-	1.0	1.0	<LD	<LD	<LD	<LD	<LD	<LD	<LD	<LD	<LD	<LD	<LD	<LD	<LD	1.3	1.1	0.4	3.3	3.4	2.1	1.3	6.4			
Ba	1.3	77	62	20	193	4.3	-	4.3	4.3	24	5.0	20	27	<LD	<LD	<LD	<LD	<LD	<LD	<LD	<LD	<LD	<LD	<LD	<LD	<LD	2.3	0.16	2.1	2.4	12	29	0.70	92			
La	0.14	0.68	0.26	0.34	1.04	0.71	0.28	0.37	1.2	1.4	-	1.4	1.4	<LD	<LD	<LD	<LD	0.75	0.20	0.61	0.89	0.82	0.12	0.58	1.1	0.65	0.14	0.51	1.0	1.0	0.58	0.71	2.2				
Pr	0.15	1.0	0.30	0.63	1.4	1.2	0.49	0.56	1.8	1.3	1.0	0.62	2.0	0.38	0.02	0.36	0.39	1.6	0.20	1.4	1.7	1.4	0.24	1.2	2.1	1.3	0.35	0.95	2.1	1.7	1.0	1.1	3.7				
Cr	0.13	<LD	<LD	<LD	<LD	<LD	0.18	-	0.18	0.18	<LD	<LD	<LD	<LD	<LD	<LD	<LD	0.11	-	0.11	0.11	0.18	0.04	0.12	0.23	0.12	0.05	0.08	0.23	0.22	0.17	0.11	0.55				
Nd	0.74	<LD	<LD	<LD	<LD	<LD	0.50	-	0.50	0.50	<LD	<LD	<LD	<LD	<LD	<LD	<LD	<LD	<LD	<LD	<LD	0.72	-	0.72	0.72	0.57	0.11	0.41	0.70	0.74	0.32	0.48	1.2				
Sm	0.90	<LD	<LD	<LD	<LD	<LD	<LD	<LD	<LD	<LD	<LD	<LD	<LD	<LD	<LD	<LD	<LD	<LD	<LD	<LD	<LD	<LD	<LD	<LD	<LD	0.34	-	0.34	0.34	0.40	<LD	<LD	<LD	<LD			
Eu	0.25	0.43	<LD	0.43	0.43	0.32	0.07	0.27	0.37	<LD	<LD	<LD	<LD	<LD	<LD	<LD	<LD	0.30	-	0.30	0.30	0.38	0.11	0.24	0.55	0.43	0.06	0.28	0.49	0.28	0.06	0.21	0.35				
Gd	0.90	<LD	<LD	<LD	<LD	<LD	<LD	<LD	<LD	<LD	<LD	<LD	<LD	<LD	<LD	<LD	<LD	<LD	<LD	<LD	<LD	<LD	<LD	<LD	<LD	0.77	-	0.77	0.77	<LD	<LD	<LD	<LD	<LD			
Tb	0.13	<LD	<LD	<LD	<LD	<LD	<LD	<LD	<LD	<LD	<LD	<LD	<LD	<LD	<LD	<LD	<LD	<LD	<LD	<LD	<LD	0.15	-	0.15	0.15	0.14	-	0.14	0.14	0.09	-	0.09	0.09	<LD			
Dy	0.57	<LD	<LD	<LD	<LD	<LD	<LD	<LD	<LD	<LD	<LD	<LD	<LD	<LD	<LD	<LD	<LD	<LD	<LD	<LD	<LD	<LD	<LD	<LD	<LD	0.74	0.39	0.45	1.6	<LD	<LD	<LD	<LD	<LD			
Ho	0.14	<LD	<LD	<LD	<LD	<LD	<LD	<LD	<LD	<LD	<LD	<LD	<LD	<LD	<LD	<LD	<LD	<LD	<LD	<LD	<LD	<LD	<LD	<LD	<LD	0.19	0.08	0.12	0.33	0.15	0.08	0.10	0.24	<LD			
Er	0.42	<LD	<LD	<LD	<LD	<LD	<LD	<LD	<LD	<LD	<LD	<LD	<LD	<LD	<LD	<LD	<LD	<LD	<LD	<LD	<LD	<LD	<LD	<LD	<LD	0.64	0.31	0.25	1.1	0.40	0.13	0.26	0.54	<LD			
Tm	0.14	<LD	<LD	<LD	<LD	<LD	<LD	<LD	<LD	<LD	<LD	<LD	<LD	<LD	<LD	<LD	<LD	<LD	<LD	<LD	<LD	<LD	<LD	<LD	<LD	0.14	0.03	0.10	0.17	0.14	0.01	0.13	0.15	<LD			
Yb	0.66	<LD	<LD	<LD	<LD	<LD	<LD	<LD	<LD	<LD	<LD	<LD	<LD	<LD	<LD	<LD	<LD	<LD	<LD	<LD	<LD	<LD	<LD	<LD	<LD	1.1	0.43	0.41	1.7	1.0	0.44	0.47	1.5	<LD			
Lu	0.15	<LD	<LD	<LD	<LD	<LD	<LD	<LD	<LD	<LD	<LD	<LD	<LD	<LD	<LD	<LD	<LD	<LD	<LD	<LD	<LD	<LD	<LD	<LD	<LD	0.20	0.05	0.11	0.25	0.14	0.06	0.10	0.19	<LD			
ΣREE	-	1.7	0.55	1.0	2.4	2.1	1.0	1.2	3.9	2.0	2.0	0.62	3.4	0.25	0.22	0.10	0.39	2.5	0.11	2.4	2.6	2.5	0.48	1.9	3.7	5.0	2.2	2.1	9.1	5.0	2.6	2.3	9.8				
Ta	0.14	<LD	<LD	<LD	<LD	0.16	0.04	0.13	0.19	<LD	<LD	<LD	<LD	<LD	<LD	<LD	<LD	<LD	<LD	<LD	<LD	0.19	-	0.19	0.19	0.09	0.02	0.07	0.11	<LD	<LD	<LD	<LD	<LD	<LD		
W	0.76	8.9	5.5	4.0	19	<LD	<LD	<LD	<LD	3.4	0.32	3.2	3.6	<LD	<LD	<LD	<LD	<LD	<LD	<LD	<LD	5.6	2.7	1.6	9.2	4.5	4.5	0.50	1.5	0.68	0.13	0.61	0.84	<LD			
Pb	0.41	3.4	1.2	2.4	5.7	3.0	0.58	2.0	3.8	7.5	7.0	2.6	12	1.7	0.30	1.5	1.9	2.6	0.04	2.6	2.7	3.3	1.2	1.8	7.2	4.0	1.2	2.8	7.3	3.0	0.67	2.3	3.9				
Bi	0.23	<LD	<LD	<LD	<LD	0.95	-	0.9	0.9	<LD	<LD	<LD	<LD	<LD	<LD	<LD	<LD	<LD	<LD	<LD	<LD	12	-	12	12	1.0	0.75	0.37	2.5	1.0	0.64	0.50	1.9	<LD			
Th	0.22	<LD	<LD	<LD	<LD	<LD	<LD	<LD	<LD	<LD	<LD	<LD	<LD	<LD	<LD	<LD	<LD	<LD	<LD	<LD	<LD	<LD	<LD	<LD	<LD	1.8	1.0	0.15	3.6	1.1	0.89	0.27	2.7	<LD			
U	0.20	<LD	<LD	<LD	<LD	0.15	-	0.15	0.15	1.0	-	1.0	1.0	0.36	-	0.36	0.36	<LD	<LD	<LD	<LD	<LD	0.29	0.12	0.18	0.42	3.8	2.4	0.09	6.5	4.5	2.7	1.5	8.6			

LD: limit of detection

Table 2. (continued)

Table 3. Boron isotopic compositions of tourmaline from Puy-les-Vignes measured by SIMS.

Sample	Zone	$^{11}\text{B}/^{10}\text{B}$	$\delta^{11}\text{B}$ (‰)	$\pm 2\sigma$ (‰)
Greisen tourmaline (Tur 1)				
PLV-02-08a_02	Core	3.892	-11.06	0.36
PLV-02-08a_09	Core	3.896	-10.07	0.40
PLV-02-08a_06	Core	3.896	-10.00	0.33
PLV-02-08a_08	Core	3.897	-9.63	0.44
PLV-02-08a_10	Rim	3.903	-9.41	0.56
PLV-02-08a_11	Rim	3.904	-9.16	0.40
PLV-02-08a_01	Rim	3.906	-8.65	0.40
PLV-02-08a_03	Rim	3.907	-8.45	0.37
PLV-02-08a_04	Rim	3.907	-8.42	0.36
PLV-02-08a_05	Overgrowth	3.903	-8.17	0.25
PLV-02-08a_07	Overgrowth	3.904	-7.78	0.33
		Average (n=11)	-9.16	0.98
Tourmalinite on gneissic clast (Tur 2a)				
PLV-02-01a_03	Core	3.884	-13.08	0.32
PLV-02-01a_01	Core	3.888	-12.07	0.28
PLV-02-01a_07	Core	3.889	-11.69	0.34
PLV-02-01a_08	Rim	3.890	-11.55	0.34
PLV-02-01a_02	Overgrowth	3.887	-12.15	0.28
PLV-02-01a_04	Overgrowth	3.888	-12.03	0.26
PLV-02-01a_05	Overgrowth	3.890	-11.46	0.38
PLV-02-01a_06	Overgrowth	3.891	-11.14	0.41
		Average (n=8)	-11.90	0.59
Acicular tourmaline (Tur 3)				
PLV-02-01c_07	Core	3.884	-13.05	0.32
PLV-02-01c_05	Core	3.884	-12.99	0.31
PLV-02-01c_12	Core	3.885	-12.89	0.30
PLV-02-01c_01	Core	3.885	-12.76	0.35
PLV-02-01c_10	Core	3.885	-12.71	0.32
PLV-02-01c_06	Core	3.886	-12.62	0.26
PLV-02-01c_03	Core	3.888	-12.11	0.29
PLV-02-01c_11	Rim	3.883	-13.21	0.30
PLV-02-01c_08	Rim	3.885	-12.91	0.35
PLV-02-01c_02	Rim	3.886	-12.62	0.26
PLV-02-01c_09	Rim	3.886	-12.42	0.40
PLV-02-01c_04	Rim	3.887	-12.25	0.38
		Average (n=12)	-12.71	0.33
Breccia tourmaline (Tur 4)				
PLV-02-13b_14	Core	3.889	-13.02	0.40
PLV-02-13b_13	Core	3.891	-12.45	0.43
PLV-02-13b_01	Core	3.892	-12.29	0.36
PLV-02-13b_07	Core	3.892	-12.18	0.49
PLV-02-13b_03	Rim	3.888	-12.08	0.39
PLV-02-13b_12	Rim	3.888	-12.04	0.44
PLV-02-13b_02	Rim	3.888	-11.97	0.31
PLV-02-13b_05	Rim	3.894	-10.44	0.38
PLV-02-13b_11	Rim	3.895	-10.30	0.67
PLV-02-13b_06	Overgrowth	3.883	-13.26	0.37
PLV-02-13b_04	Overgrowth	3.886	-12.43	0.33
PLV-02-13b_15	Overgrowth	3.889	-11.75	0.38
PLV-02-13b_10	Overgrowth	3.890	-11.55	0.44
PLV-02-13b_09	Overgrowth	3.894	-10.52	0.42
PLV-02-13b_08	Overgrowth	3.894	-10.51	0.49
		Average (n=15)	-11.79	0.94

